IntechOpen

RF Systems, Circuits and Components

Edited by Mamun Bin Ibne Reaz
and Mohammad Arif Sobhan Bhuiyan

RF SYSTEMS, CIRCUITS AND COMPONENTS

Edited by **Mamun Bin Ibne Reaz**
and **Mohammad Arif Sobhan Bhuiyan**

RF Systems, Circuits and Components
http://dx.doi.org/10.5772/intechopen.72548
Edited by Mamun Bin Ibne Reaz and Mohammad Arif Sobhan Bhuiyan

Contributors

Chulsoon Hwang, Lahbib Zenkouar, Loubna Berrich, Charlotte Tripon-Canseliet, Jean Chazelas, Mikhail Belkin, Vladislav Golovin, Yuri Tyschuk, Mikhail Vasil’Ev, Alexander Sigov, Shahab Niazi, Sumathi Manickam

© The Editor(s) and the Author(s) 2019
The rights of the editor(s) and the author(s) have been asserted in accordance with the Copyright, Designs and Patents Act 1988. All rights to the book as a whole are reserved by INTECHOPEN LIMITED. The book as a whole (compilation) cannot be reproduced, distributed or used for commercial or non-commercial purposes without INTECHOPEN LIMITED’s written permission. Enquiries concerning the use of the book should be directed to INTECHOPEN LIMITED rights and permissions department (permissions@intechopen.com).
Violations are liable to prosecution under the governing Copyright Law.

Individual chapters of this publication are distributed under the terms of the Creative Commons Attribution 3.0 Unported License which permits commercial use, distribution and reproduction of the individual chapters, provided the original author(s) and source publication are appropriately acknowledged. If so indicated, certain images may not be included under the Creative Commons license. In such cases users will need to obtain permission from the license holder to reproduce the material. More details and guidelines concerning content reuse and adaptation can be foundat http://www.intechopen.com/copyright-policy.html.

Notice

Statements and opinions expressed in the chapters are these of the individual contributors and not necessarily those of the editors or publisher. No responsibility is accepted for the accuracy of information contained in the published chapters. The publisher assumes no responsibility for any damage or injury to persons or property arising out of the use of any materials, instructions, methods or ideas contained in the book.

First published in London, United Kingdom, 2019 by IntechOpen
eBook (PDF) Published by IntechOpen, 2019
IntechOpen is the global imprint of INTECHOPEN LIMITED, registered in England and Wales, registration number: 11086078, The Shard, 25th floor, 32 London Bridge Street
London, SE19SG – United Kingdom
Printed in Croatia

British Library Cataloguing-in-Publication Data
A catalogue record for this book is available from the British Library

Additional hard and PDF copies can be obtained from orders@intechopen.com

RF Systems, Circuits and Components
Edited by Mamun Bin Ibne Reaz and Mohammad Arif Sobhan Bhuiyan

p. cm.

Print ISBN 978-1-78985-763-4

Online ISBN 978-1-78985-764-1

eBook (PDF) ISBN 978-1-83962-096-6

Meet the editors

Mamun Bin Ibne Reaz was born in Bangladesh in December 1963. He received his BSc and MSc degrees in Applied Physics and Electronics, both from University of Rajshahi, Bangladesh, in 1985 and 1986, respectively. He received his D.Eng. degree in 2007 from Ibaraki University, Japan. He is currently a Professor in the Department of Electrical, Electronic and Systems Engineering, Universiti Kebangsaan Malaysia, Malaysia, and is involved in teaching, research and industrial consultation. He is a Senior Associate of the Abdus Salam International Centre for Theoretical Physics (ICTP), Italy, since 2008. He is also a Senior Member of IEEE. He has published extensively in the area of IC Design, Biomedical application IC and Smart Home. He has authored and co-authored more than 300 research articles in design automation, IC design for biomedical applications and Smart Home. He is also the recipient of more than 50 research grants (national and international).

Mohammad Arif Sobhan Bhuiyan was born in Chittagong, Bangladesh, in 1985. He received his BSc and MSc degrees in Applied Physics, Electronics and Communication Engineering from the University of Chittagong, Bangladesh, in 2006 and 2007, respectively. He received his PhD from the Universiti Kebangsaan Malaysia, Malaysia, in 2017. He is currently an Assistant Professor at the department of Electrical and Electronics Engineering, Xiamen University Malaysia, Malaysia. His research interest is in the field of RFID, VLSI and Wireless Communication.

Contents

Preface XI

Chapter 1 **Design Concepts of Low-Noise Amplifier for Radio Frequency Receivers 1**
Sumathi Manickam

Chapter 2 **Study of the PIFA Antenna for RFID Applications 21**
Loubna Berrich and Lahbib Zenkouar

Chapter 3 **Low-Dimensional Materials for Disruptive Microwave Antennas Design 41**
Charlotte Tripon-Canseliet and Jean Chazelas

Chapter 4 **Computer-Aided Design of Microwave-Photonics-Based RF Circuits and Systems 61**
Mikhail E. Belkin, Vladislav Golovin, Yuri Tyschuk, Mikhail G. Vasil'ev and Alexander S. Sigov

Chapter 5 **Integration of Hybrid Passive Optical Networks (PON) with Radio over Fiber (RoF) 83**
Shahab Ahmad Niazi

Chapter 6 **RF Desensitization in Wireless Devices 101**
Chulsoon Hwang

Preface

Radio frequency(**RF**) refers to an oscillation rate of an alternating electric current or voltage or of a magnetic, electric or electromagnetic field or mechanical system with frequencies between the upper limit of audio frequencies (>20KHz) and the lower limit of infrared frequencies (<300GHz). The rapid development of modern compact wireless devices is driven by the fast growing market of wireless communication. The increased popularity and easy operation of RF devices for different end users and corporate applications such as RFID, Bluetooth, Zigbee and Wi-Fi devices, non-contacting medical instruments and sensors, in recent years, have raised the demand for small power and less off-chip components that tend to achieve integration of multiple transmitter/receiver chains on the same die with added security and convenience in our daily lives. Concurrent technologies allow scientists and researchers to reinvent low power, high performance and reliable RF systems, circuits and components for many home and commercial applications. The features of RF systems, circuits and components are still being researched and integrated in existing systems to create marketable and potential new RF systems and devices including many exciting applications.

The fulfilment of the increased demand for low power, high performance and reliable RF devices is now possible because of the continuous downscaling of CMOS technology. But at the same time, because of the downscaled CMOS process, many issues related to RF circuitries such as low noise amplifier (LNA), especially at the analogue front end, need to be considered and solved with reduced power supply.

An antenna is an inherent part of every RF communication system. Without an efficient, compact and low cost antenna, the RF communication for systems such as RFID and Wi-Fi. cannot be implemented. The choice of antenna type, size, shape and substrate material plays a vital role in the overall RF system. Specifically, carbon nanotube (CNT) based materials can be a good choice for a high-performance antenna substrate material for RF systems.

Today's telecommunication industry must provide services such as: mobility, high speed and large capacity to the end-users. Luckily, concurrent modern tools and technology help the researchers to implement suitable RF communication systems. It is obvious that RF provides the mobility whereas optical fiber ensures the speed and capacity. Therefore, radio over fiber (RoF) communication and microwave photonics (MWP) based circuitry will provide good support for the rapidly growing telecom industry.

The next decade will be the decade of internet of things (IoT). In order to achieve the benefits of IoT, electromagnetic interference (EMI) compensation will be a vital issue as it limits the radio range (RF desensitization). Therefore, an insightful and efficient RF desensitization model is necessary to estimate EMI levels on RF antennas so that the engineering issues such as where to place the IoT device or setting the radiation specification of the device etc. can be easily addressed.

In this book, we represent contributions from world-leading experts on the latest developments and state-of-the-art results in RF systems, circuits and components to address current research challenges. The book offers a comprehensive and systematic description of technologies, architectures and methodologies of various efficient, secure, scalable and reliable RF applications.

This book will serve as a valuable reference point for researchers, educators and engineers who are working with RF based applications as well as graduate students who wish to understand, learn and discover opportunities in this emerging research and development area. It is our hope that the work presented in this book will open new discussions and generate new and innovative ideas that will further develop this important area.

We thank the authors for their outstanding and timely contributions. We would like to thank InTech for the opportunity to publish this book. Our special thanks go to **Ms. Romina Skomersic** for her continued support and professionalism during the whole publication process of this book.

Mamun Bin Ibne Reaz
Centre of Advanced Electronic and Communication Engineering
Faculty of Engineering and Built Environment
Universiti Kebangsaan Malaysia, Malaysia

Mohammad Arif Sobhan Bhuiyan
Electrical and Electronics Engineering
School of Electrical and Computer Engineering
Xiamen University Malaysia, Malaysia

Chapter 1

Design Concepts of Low-Noise Amplifier for Radio Frequency Receivers

Sumathi Manickam

Additional information is available at the end of the chapter

http://dx.doi.org/10.5772/intechopen.79187

Abstract

The development of high-performance radio frequency (RF) transceivers or multi-standard/reconfigurable receivers requires an innovative RF front-end design to ensure the best from a good technology. In general, the performance of front-end and/or building blocks can be improved only by an increase in the supply voltage, width of the transistors or an additional stage at the output of a circuit. This leads to increase the design issues like circuit size and the power consumption. Presently, the wireless market and the need to develop efficient portable electronic systems have pushed the industry to the production of circuit designs with low-voltage power supply. The objective of this work is to introduce an innovative single-stage design structure of low noise amplifier (LNA) to achieve higher performance under low operating voltage. TSMC 0.18 micron CMOS technology scale is utilized for realizing LNA designs and the simulation process is carried out with a supply voltage of 1.8 V. The LNA performance measures are analyzed by using an Intel Core2 duo CPU E7400@2.80GHz processor with Agilent's Advanced Design System (ADS) 2009 version software.

Keywords: CMOS, RF circuits, VLSI design

1. Introduction

Today, there is an increased market demand for portable wireless communication devices and high-speed computing devices. This is true because low cost and high integration have resulted in the commercial success in wireless communication integrated circuits. But these devices are operated by batteries which have only a limited lifetime. The battery technology has not improved on par with electronics technology. As the developments in battery technology have failed to keep up with an increasing current consumption in wireless communication devices, innovative circuit design techniques are required in order to reduce the power consumption and to utilize the low voltage. Radio frequency ICs are the basic building blocks of portable wireless communication systems. The use of a manufacturing technology for implementing and integrating these circuits is very important. The decision is based mainly on cost and integration levels. In the radio frequency circuit design, the technologies such as GaAs (Gallium Arsenide), SiGe (Silicon Germanium), and BiCMOS (Bipolar CMOS) provide good performance in high-frequency characteristics. But these processes lead to an increase in cost and process complexity [1]. In recent years, CMOS technology has been used as it is the best for implementation of low cost and high integration level systems on the chip.

Another aspect for the realization of analog circuits in CMOS technology is the possibility of reduction in supply voltage with each technology generation. The development of low-voltage analog RF circuits is means economy. At the same time, the existing circuit topologies cannot conform to the required high-performance wireless specifications under low-voltage operation. Hence, it is of a great need to introduce new design evaluations of wireless direct conversion receiver front-end circuits that can successfully handle low-supply voltages. The choice of receiver architecture, circuit topology design, and systematic optimization of the front-end blocks is always important. The choice of the receiver architecture, fundamental receiver front-end parameters needed in RF circuit design, the significance of CMOS technology, and MOS transistors high-frequency characteristics are discussed briefly. IEEE 802.11b/g wireless standards and its front-end specifications are the main target applications for the designs evaluated and are then presented.

2. Review of receiver architectures

The purpose of the receiver in wireless communication system is to perform certain operations required for the received signal such as amplification, frequency translation, and analog-to-digital conversion with adequate signal-to-noise ratio before subjected to digital signal processing. The performance of a receiver is analyzed by the ability to receive the strong or weak signal in the presence of strong interferences. The performance measures are expressed in terms of sensitivity, selectivity, fidelity, and dynamic range. The selection of receiver architecture is based on performance, cost, and power dissipation. The integration level along with the number of off-chip components determines the cost of the receiver. The existing receiver topologies in RF transceivers are Zero-IF, Heterodyne, Low-IF, and Wide-band IF. The description of these receiver architectures is briefly given in this thesis.

2.1. Direct conversion receiver

A direct conversion receiver (DCR) is also named as homodyne, synchrodyne, or zero-IF receiver. It was developed in 1932 by a team of British scientists. This receiver provides the most natural solution to detect information transmitted by a carrier in just a single conversion stage. The simplified block diagram of a typical direct conversion receiver is shown in **Figure 1**.

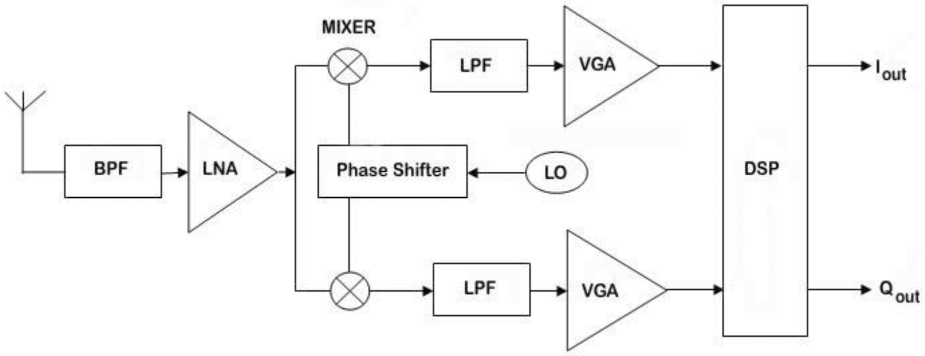

Figure 1. Direct conversion receiver.

A synchrodyne receiver is a radio receiver that demodulates the incoming radio signal using a synchronous detection driven by a local oscillator. The signal conversion (RF to IF) to baseband is done in a single-frequency conversion. The RF signal from the antenna is pre-filtered by a bandpass filter (BPF) to suppress the signals out of the reception band. The signal is amplified at the low-noise amplifier (LNA) stage and down-converted into zero intermediate frequency (IF) by the mixer stage. The resulting IF signal frequency is the difference between the RF and local oscillator signal frequencies. In the case of the phase and frequency-modulated signals, the down-conversion process should be performed in quadrature to prevent signal sidebands from aliasing on one another. As the local oscillator is centered in the desired channel, it requires signal and noise to occupy both the upper and lower sidebands. The down-conversion architecture produces an image at zero-IF frequency, and thus no image filter is required.

The important characteristic of the direct-conversion receiver is that amplification and filtering are mostly performed at the baseband rather than at the RF. The required signal is selected with the help of a low-pass-type baseband filter (BBF). The low-pass filter with a bandwidth of a half of the symbol rate removes the adjoining channels at baseband. As the filtering is performed at low frequencies, filters can be realized in on-chip without using external high-Q components. Most of the signal processing action takes place at low frequencies, thereby minimizing power consumption. The DCR eliminates the image rejection problem existing in other radio architectures [2]. However, an inadequate amplitude and phase balance between in-phase and quadrature-phase signals can increase the bit-error rate [3, 4]. It has its own disadvantages such as a highly sensitive to flicker noise and DC offsets. These problems can be eliminated in the wideband system design by making use of high-pass filters. The DCR avoids the complexity of the superheterodyne's two or more frequency conversions, IF stages, and image rejection issues. Recent research works proved that the zero-IF is always popular and is widely used for RF applications due to its simplicity, fewer off-chip components, and minimized power. Most of the receivers use the same RF front-end which includes LNA, mixer, and an oscillator. As per the constructional and performance point of view, direct conversion receivers are more suitable to satisfy the following constraints such as simplicity, integration level, less off-chip components, and power dissipation. The described front-end circuits are all targeted for direct conversion receivers.

CMOS is always cheap in processing cost and one of the best technologies for the implementation of analog design without any adaptations. Further, it can provide better integration of digital circuitry with high-performance analog circuits. Also, it provides the possibility of complete system on-chip, entire analog front-end, and the digital demodulator implemented on the same die. CMOS technology has the capability to operate at a lower supply voltage than the BiCMOS technology. This is due to the fact that each transistor has a typical switch on voltage of 0.7–0.8 V, and thus the minimum supply voltage required for BJT circuits is about 2–3 V. But modern CMOS processes provide many different threshold voltages (V_t) such as high, moderate, and low standards. For instance, MOS transistors with a lower threshold can be utilized in analog or digital circuits, where speed is important.

On the other hand, devices with a higher threshold are useful when the low-power consumption of the digital circuits is affected by leakage currents. This feature enables the circuitry design under low operating voltage even when technology is scaled down toward deep submicron CMOS processes.

Technology scaling is the primary factor in achieving high-performance circuit designs and systems. Each reduction in CMOS technology scaling has a reduced gate delay, doubled the device density, and a reduced energy per transition. To achieve this, each transistor width, length, and oxide dimensions are also scaled by 30%. Taiwan Semiconductor Manufacturing Company (TSMC) is the world's largest dedicated semiconductor foundry, providing the industry's leading process technology. TSMC 0.18 micron CMOS logic process is widely used for various electronic systems such as microprocessors, microcontrollers, and high-speed processors. It provides the device models under the operating voltage of 1.8 V. Therefore, this technology scale is utilized for realizing front-end designs. TSMC 0.18-μm RF CMOS models used in this research work are shown in **Figure 2**. The simplified device specifications are given in **Table 1**. The benefits and drawbacks of silicon technologies are highlighted in this section. The availability of accurate simulation models, high-frequency models, and noise models of devices are essential for accurately predicting the performance of RF circuits.

2.2. Overview of wireless standards

Currently, wireless applications in 2.4/5 GHz frequency range are receiving greater attention because it is relatively economical and its potential for system on-chip integration. IEEE 802.11a/b/g is a set of promising standard in the market of portable/wireless communication devices such as cellular phones, WLANs, RFID, global positioning systems, etc. In the 5-GHz frequency range, the IEEE 802.11a standard is purely based on orthogonal frequency division multiplexing (OFDM) modulation technology, and it is compatible with data rates up to 54 Mbps. It provides nearly four to five times the data rate and has 10 times the overall system capacity as currently available in IEEE 802.11b wireless systems [5, 6].

The IEEE 802.11b/g operates in the 2.4–2.5 GHz ISM band, which use the direct sequence, spread spectrum signaling (DSSS) with a maximum data rate of 11Mbps, and occupies the

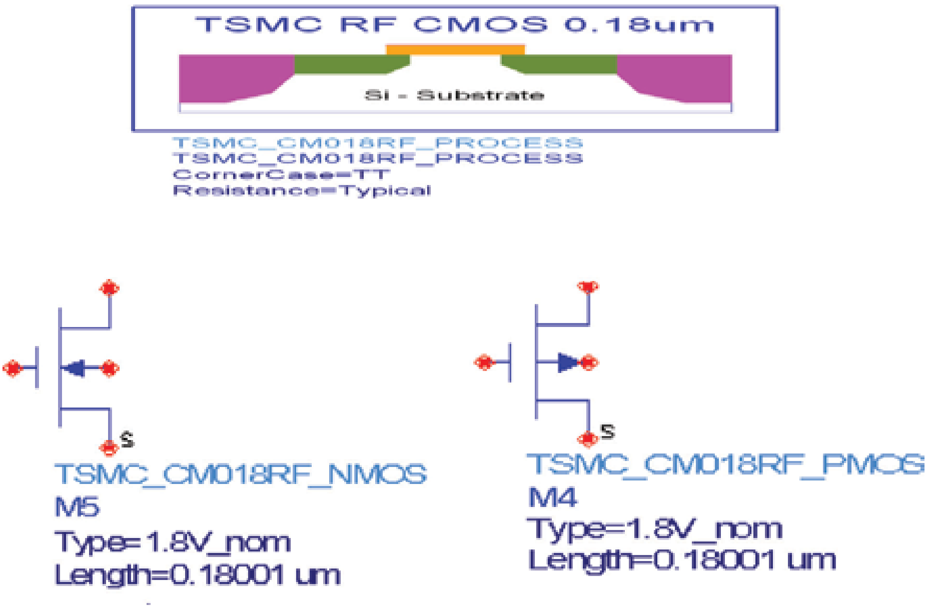

Figure 2. TSMC 0.18-μm RF CMOS models.

Blocks	Gain	Noise figure	IIP3
LNA	16 dB	3 dB	−5 dBm
MIXER	10 dB	4 nV/√Hz	10 dBm

Table 1. IEEE 802.11b/g DCR front-end specifications.

same frequency spectrum with a data rate of 54 Mbps with orthogonal frequency division multiplexing (OFDM) modulation methods, respectively. The proposed work is mainly highlighted to meet the direct conversion specification of IEEE 802.11b/g applications as shown in **Table 1**.

2.3. Research issues

Recently, reported designs are based on inductively degenerated cascode LNAs which do not satisfy an optimum gain, a lowest NF, and a better impedance matching. The evaluation of an active mixer with moderate linearity is one of the challenges in low-voltage design and has become an important issue in most analog IC applications. Gilbert mixer is the commonly used double-balanced, active mixer configuration. A better performance can be achieved using this structure. But this needs increase in the current through the transconductance stage and switching stage, and therefore a higher supply voltage will be required. It has a stacked structure which limits its use in low-voltage applications. In general, two types of oscillators namely LC tank and ring oscillators are often used to generate a local frequency. In GHz frequency applications, ring topology is usually preferred because of its improved noise performance and lower-power consumption. It avoids the use of spiral inductors which are employed in LC tank oscillators. But these oscillators need to be realized by using digitally controlled logics with efficient delay elements for a high-frequency generation.

Reported LC oscillator designs provided changes only to the elements in tuned circuitry and analyzed the performance. It is clearly understood that the performance of front-end blocks can be improved either by increasing the supply voltage or by providing additional stages at the output. The abovementioned problem motivated to introduce an innovative single-stage design of front-end blocks under low operating voltage for 2.4 GHz/5GHz wireless applications. The simplified block diagram of a direct conversion receiver (DCR) front-end used in this research work is shown in **Figure 3**. It represents the process of incoming 2.4 GHz RF signal frequency (f_{RF}) by the LNA and down-converted into 150-MHz intermediate frequency (f_{IF}) by the mixer. The first stage of a receiver front-end is typically a low-noise amplifier (LNA) whose main function is to provide sufficient gain in order to overcome the noise of next stages. The receiver's sensitivity mainly depends upon the LNA noise figure and gain. A down-conversion mixer is always followed by the RF low-noise amplifier. It is one of the most important parts and used to translate one frequency into another. It changes the RF signal into an IF output signal. Intermediate frequency (IF) is the difference between RF and LO signal frequencies.

Mixer plays an important role in improving the overall system linearity. Oscillator is a signal generation circuit where tuned and amplifier blocks only decide the required frequency of oscillation. The digital revolution and higher growth of portable wireless devices market require many changes to the analog front-ends. It also requires new architectures, techniques, and high integration level. The CMOS design is chosen in this research because it can provide an attractive solution for RF analog circuits in terms of cost and integration level. The technology scaling in CMOS has increased the cutoff frequency of transistors and allows the improved performance of analog circuits. This chapter describes the importance of front-end blocks along with the necessity of low-voltage design and then discusses the known techniques and structures for the performance of front-end circuits. As can be seen from **Figure 4**, front-end is

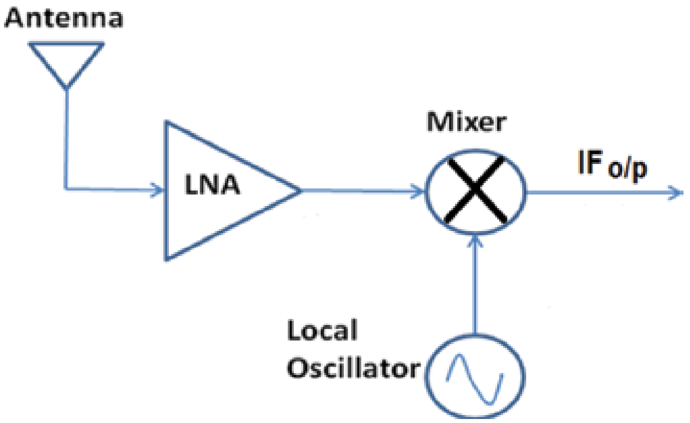

Figure 3. Block diagram of DCR front-end.

an interface between the antenna and the digital signal-processing unit of the wireless receiver. Basically, front-ends are responsible for tracking weak signal (RF) at a high frequency and translating into IF signal for transmitting with high power levels. It needs high-performance analog circuits like RF amplifier (LNA), mixer, and an oscillator. Recently, the wireless market and the need to develop efficient portable electronic systems have pushed the industry to the production of circuit designs with a low-voltage power supply. In the past years, low-power consumption usually was less considered among key design specifications. But today, both increased device/circuit density of current CMOS technology and battery-operated portable systems necessitate low-voltage, low-power system/circuit design [7–9].

Figure 5 represents the channel length and supply voltage variation in deep sub-micron CMOS technologies [6]. It is observed that CMOS technology leads to smaller and smaller channel lengths, and the performance of RF communication circuit design will continue to improve with the reduction of supply voltage. One common technique for reducing power in analog or digital circuits is to reduce the supply voltage. In this research, front-end designs are evaluated under the supply voltage of 1.8 V. The constraint toward the low-voltage design is the

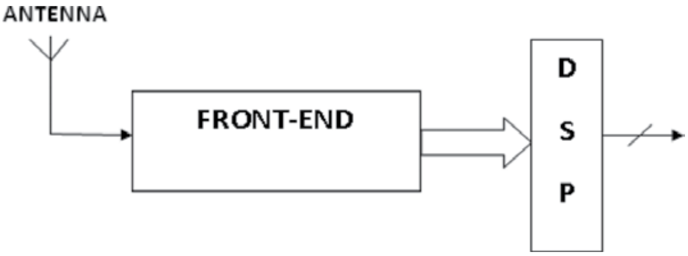

Figure 4. Front-end in wireless receiver.

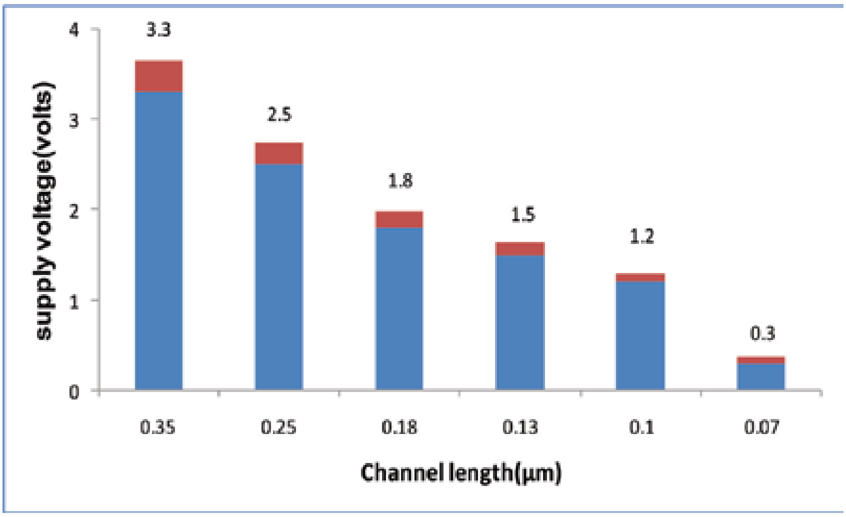

Figure 5. CMOS voltage scaling.

threshold voltage and drain-source saturation voltage which do not scale down at an exact rate as the supply voltage or do not scale under a low-supply voltage. It is a problem as well as a challenge to face for analog designer due to the limited voltage headroom. Some circuit designs can only operate under a higher supply voltage with desirable properties and lose their high performance in a low-voltage environment. Therefore, alternative circuit structures or even system topologies need to be investigated. In modern CMOS processes, critical analog and RF circuits can be implemented with dual-gate, multi-threshold, and thick-oxide MOSFETs, which tolerate higher supply voltages, but this solution increases the cost, since additional processing masks are required [10–15]. The development of low-voltage CMOS analog and RF front-end circuits is essential and economically advantageous.

2.4. Low-noise amplifier design

A low-noise amplifier is the first stage of the receiver front-end and it is used to increase the signal power coming from the antenna while introducing less noise by the same LNA. **Figure 6** shows the block diagram of LNA. In general, the LNA structure is composed of impedance matching block for input/output section (IMN, OMN) and amplification block (AMP). Matching networks account for performing part of filtering, optimum noise performance, and provides stability at the input as well as output. The matching elements are passive, consisting of strip lines, inductors, capacitors, and resistors. R_S and R_L represent the source and load impedances, respectively.

The cascode structure is popularly used in LNA for narrow-band wireless applications. It is a two-stage amplifier consisting of common source and common gate (CS-CG) stages. The following are the basic characteristics of a cascode amplifier such as a higher input-output isolation, a higher input/output impedance, and a higher gain with bandwidth. **Figure 7** represents the simplified cascode structure. It is a combination of an amplifying device (CS transistor- M_1) with a load device (CG transistor- M_2).

CS transistor M_1 is considered as input stage driven by a signal source V_{in}. It is also used to drive a CG transistor M_2 as output stage, with output signal V_{out}. L_g and L_s are the gate, source inductors of $M_{1,}$ respectively, responsible for impedance matching. L_d is the drain inductor of M_2, responsible for output impedance matching. The importance of CS and CG stages has been highlighted by design equations and is given subsequently.

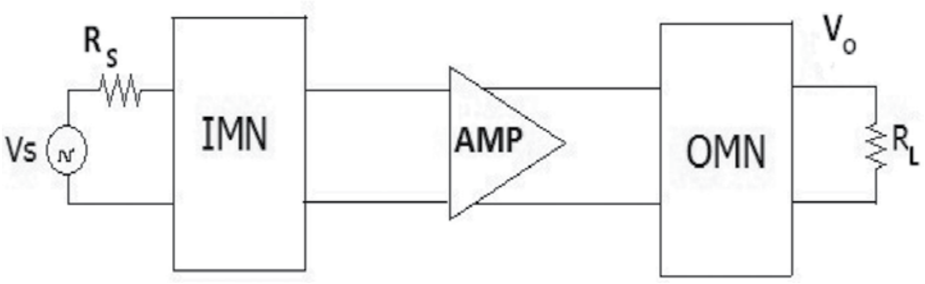

Figure 6. Block diagram of LNA.

2.4.1. Single-ended dual-CS low-noise amplifier (SDC LNA)

The amplification block (CS stage) of the cascode amplifier is revised in this research to achieve an optimized performance in single-ended and differential topologies using ADS software. These LNAs are titled as SDC and DDC LNA. The amplification block is altered by dual nMOS transistors at the CS stage. The purpose of this structure is to eliminate the use of an additional stage at the output for further amplification. It does not occupy much area in implementation and reduce the design complexity than two-stage LNA designs. **Figure 8** represents the dual CS stage of LNA. An inter-stage inductor is added in between the CS and CG stages for improving the impedance matching. **Figure 9** represents the schematic of SDC LNA architecture. It comprises input stage inductor L_g, inter-stage inductor L_{IS}, dual CS transistors M1 - M2, single CG transistor M3, and output impedance matching inductor L_d. The bias current is chosen to provide the optimum overdrive voltage for dual CS transistors using transistor M4 and resistor R, C_{in} and C_o are blocking capacitors used to block DC signal and allow only AC signal.

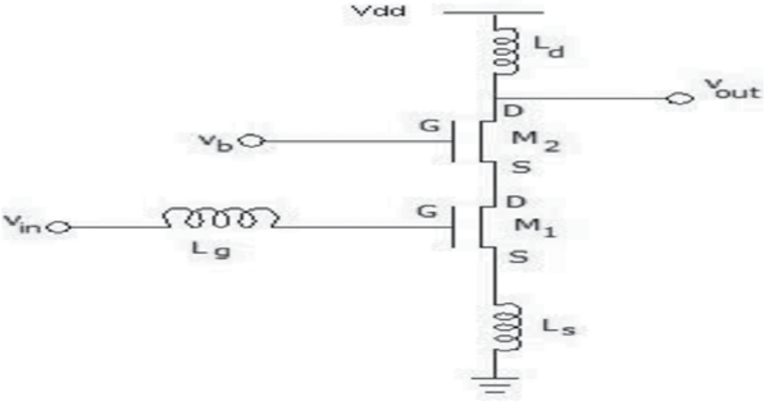

Figure 7. Cascode structure.

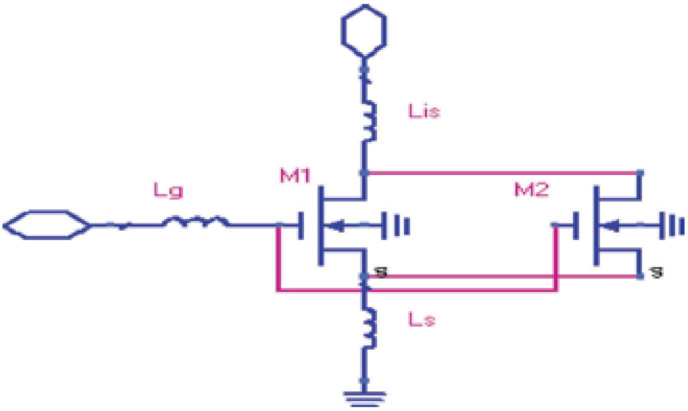

Figure 8. Structure of dual CS stage.

From the schematics, an equivalent model of input stage is developed for determining the simplified theoretical expressions of input impedance and output impedance of the dual CS stage and it is shown in **Figure 10**. The gate-source capacitances and drain-source currents are paralleled in this model. C_{gs1}, C_{gs2}, and $G_{m1,2}$ V_{gs} represent the gate-to-source capacitances of nMOS transistors M1, M2 and drain-source currents of both transistors. $G_{m1,2}$ is the sum of transconductances g_{m1} and g_{m2}. The input impedance of the MOSFET's without feedback is usually capacitive due to the gate-source capacitance. In order to get the resistive input impedance, an inductive feedback (L_s) is added to the source.

The input impedance seen at the gate of M1 and M2 is expressed in Eq. (1). At resonance, inductive and capacitive impedances are canceled out, and hence the input impedance becomes purely resistive.

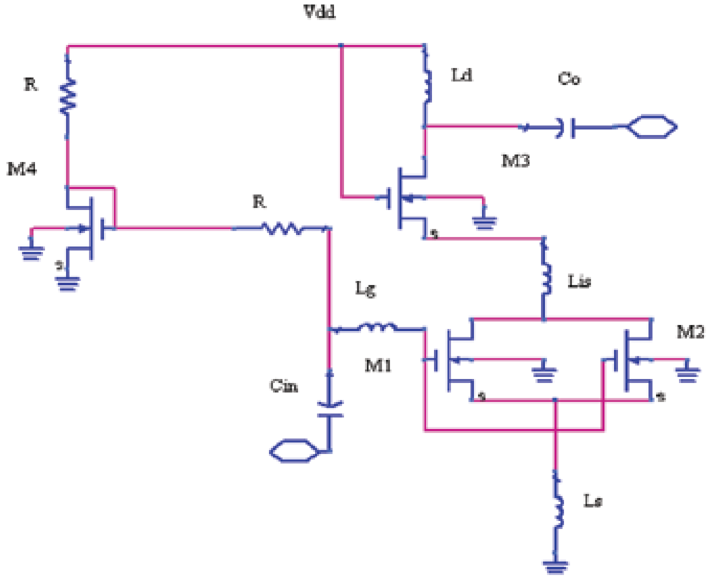

Figure 9. Schematic of SDC LNA.

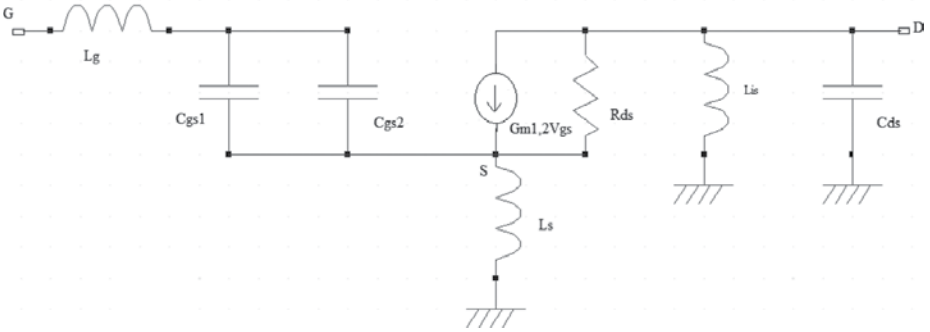

Figure 10. Equivalent model of input stage.

$$Z_{in} = \frac{L_s(g_{m1} + g_{m2})}{C_{gs1} + C_{gs2}} = \omega_T L_s \tag{1}$$

The required gate inductor (L_g) and source inductor (L_s) cancel out the imaginary part of the input impedance at 9 and 1 nH, respectively. The optimum quality factor (Q) for the best NF is about 8, with a corresponding F_{min} of 1.77 dB. An inter-stage matching inductor of 3 nH is placed in between the dual CS and CG stages.

The output impedance of the common source stage with inter-stage matching inductor is derived by using Eq. (2)

$$Z_{out} = SL_{is} + \frac{1}{S(C_{ds1} + C_{ds2})} + \frac{(g_{m1} + g_{m2})L_s}{(C_{ds1} + C_{ds2})} \tag{2}$$

where C_{ds1}, C_{ds2} are the drain-to-source capacitances of the transistors M1, M2. In the design of RF front-end, the mixer directly follows the LNA. Hence, the output impedance matching of LNA is not an issue. If the LNA output load is either an external filter or there is a need to measure the performance of the LNA alone, then the output of the LNA needs to be matched with certain impedance.

The selection of the cascode topology simplified the analysis by neglecting the gate-drain capacitance. The on-chip spiral inductor L_d and output capacitor C_o with values of 15 nH and 0.5 pF are used for output matching. The LNA circuit is designed by minimizing the noise figure for a gain constraint of 20 dB and an input and output matching constraints of −10 dB at 2.4 GHz. The width of the transistors in dual CS stage is assumed to be equal in the design analysis. The W/L ratio of cascode transistor (M3) is the same as that of a common source stage. The bias transistors width and current are arbitrarily selected as one-tenth of that of the CS transistor. With the help of operating frequency (ω_o) and the gate-to-source capacitance, the optimized width of the transistors can be computed at a particular frequency of interest. The optimized LNA performance is achieved by the transistor width values of 70–100 μm. The LNA performance is evaluated for radio frequencies of 2.4 and 5 GHz, respectively. The design analysis with suitable formulae has been expressed in the next section.

2.4.2. Differential dual CS low-noise amplifier (DDC LNA)

A differential topology approach is usually preferred in RF design due to its well-known characteristics of immunity to common mode disturbances, rejection to parasitic couplings, and an increased dynamic range. It produces a differential output which is more flexible for feeding signal information to the second stage of front-end. Here, the LNA is evaluated in differential topology, and its novel design is given in detail. **Figure 11** shows the schematic of DDC CMOS LNA. Each common source (CS) stage of cascode structure is built by two parallel transistors instead of one, and called as dual CS stage. It comprises an input stage formed by inductors L_g and L_s, two inter-stage inductors (L_{is}), four common source transistors (M1, 2 - M3, 4), and two common gate transistors (M5-M6). Two drain inductors L_D are used for output impedance matching. This structure is suitable for multiple demands of LNA such as gain, noise figure, and linearity. The equivalent circuit of the single cascode stage is shown in **Figure 12**, where the transistors M1, M2 are replaced by gate-source capacitances (C_{gs1}, C_{gs2}), channel currents ($g_{m1}V_{gs1}$, $g_{m2}V_{gs2}$), and gate-drain capacitances (C_{gd1}, C_{gd2}). r_{o1} and r_{o2} are the output resistances of two nMOS transistors M1, M2, respectively.

The cascoding transistors (M5, M6) reduce the interaction of the tuned output with the tuned input and nullify the effect of gate-drain capacitances of dual-CS transistors. The simplified expressions of input and output impedance have already been dealt in the previous section.

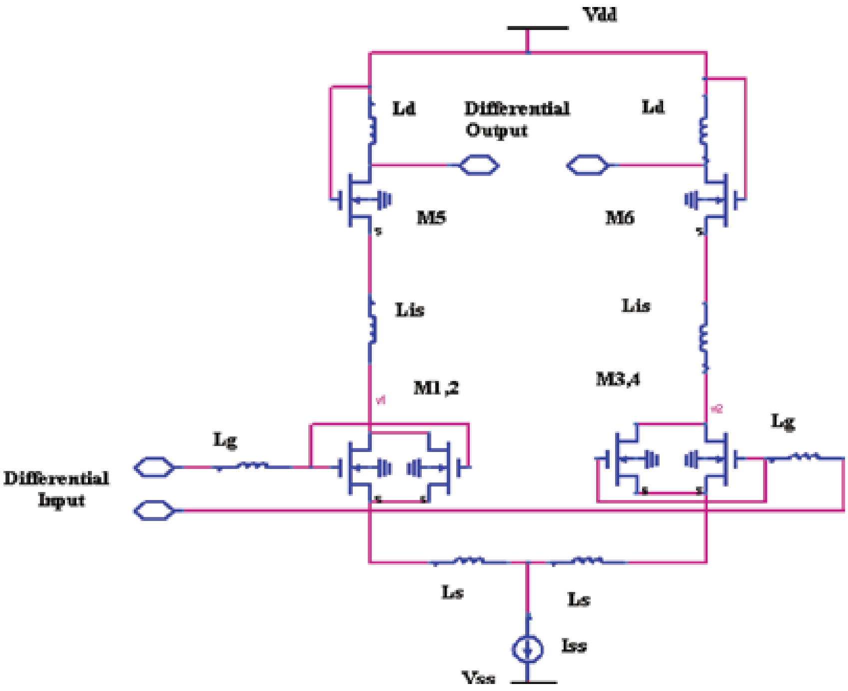

Figure 11. Schematic of DDC LNA.

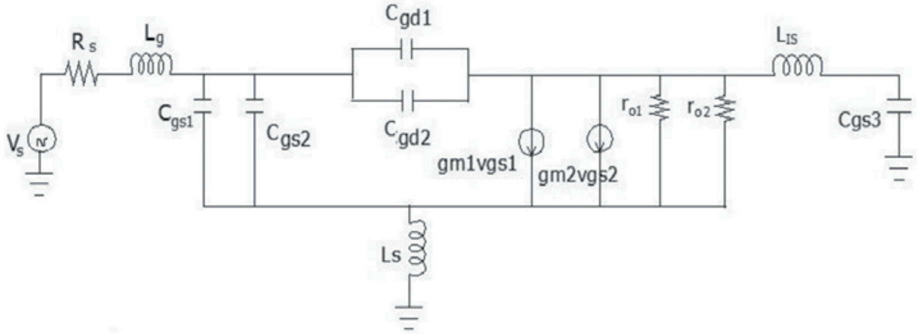

Figure 12. Equivalent circuit for input stage of DDC LNA.

The design increased the complexity in a differential structure. But the degree of design choice is satisfied with the multiple objectives such as gain, NF, and 1-dB gain compression point.

With reference to **Figure 10**, the theoretical expressions of performance factors are derived and highlighted. The total current flowing through the dual CS stage is represented by assuming that the transistors are operated in a saturation region, and it is shown in Eq. (3)

$$I_t = \frac{K}{L}\left[W_1\left(V_{gs1} - V_t\right)^2 + W_2\left(V_{gs2} - V_t\right)^2\right] \tag{3}$$

where K is the process-dependent term, L is the channel length, W_1 and W_2 are the gate widths of M1, M2, and V_{gs1}, V_{gs2}, V_t are the gate-source voltages and threshold voltage of transistors, respectively.

2.5. Design methodology

The structure of DDC LNA is a differential representation of two SDC LNAs. The design procedure is commonly described for SDC LNA and DDC LNA. Inductors and transistors are the basic building elements of LNA. Inductors are reactive and do not add noise into the circuit. The LC resonance always improves the gain and noise performance of LNA. The optimized width of the transistors and an inductance value of inductors are calculated by using appropriate design equations. The calculations are highlighted at design frequency (f_o) of 2.4 GHz with an essential feature of TSMC RF CMOS 0.18-μm technology scale. The design steps are elaborated through these design factors as follows:

1. gate inductance (L_g)
2. gate-source capacitance (C_{gs})
3. width of the transistor (W)

The center frequency

$$\omega = 2\pi f_o \tag{4}$$

where f_o is 2.4 GHz.

$$= 2\pi \times 2.4 \times 10^9 = 15.079 \times 10^9 \text{ rad/s.}$$

is calculated by using Eq. (4).

The value of gate inductor L_g is realized by means of Eq. (5). The Q of an inductor value is selected as 8, based on 0.18-μm CMOS scale characteristics. The source impedance is assumed to be 50 Ω

$$\begin{aligned} L_g &= \frac{Q_L R_s}{\omega_o} \\ &= \frac{(8 \times 50)}{15.079 \times 10^9} = 14.078\text{nH} \end{aligned} \tag{5}$$

It is observed in simulation, whenever the L_g value is reduced below 8 nH, the design frequency is shifted between 2 and 3 GHz and becomes very difficult to achieve the narrowband performance. At high frequencies, the careful design impact only reduces the component variations against the performance of LNAs.

The gate-source capacitance (C_{gs}) is expressed in terms of RF frequency, shown in Eq. (6). L_s is assumed to be 0.5–1 nH

$$\begin{aligned} C_{gs} &= \frac{1}{4\pi^2 f_o^2 \left(L_g + L_s\right)} \\ &= \frac{1}{227.4 \times 10^{18} \left(14.078 \times 10^{-9} + 1 \times 10^{-9}\right)} \\ &= 0.10050 \times 10^{-12} \\ C_{gs} &= 0.1\ pF \end{aligned} \tag{6}$$

From the technology-scale characteristics, the channel length (L) of 0.18 μm and oxide thickness (T_{ox}) of 4.1×10^{-9} m is observed. The permittivity of oxide is calculated by using this Eq. (7),

$$\varepsilon_{ox} = \varepsilon_o \varepsilon_s \tag{7}$$

where ε_0 is the dielectric constant of free space of 8.854×10^{-14} F/cm and εs the dielectric constant of silicon equal to 3.9. Therefore, the oxide capacitance or gate-oxide-specific capacitance is calculated by using Eq. (8)

$$\begin{aligned} C_{ox} &= \frac{\varepsilon_{ox}}{T_{ox}} \\ &= \frac{3.9 \times 8.85 \times 10^{-14}}{4.1 \times 10^{-9}} = 8.641 \times 10^{-8}\,\mathrm{F/mm^2} \end{aligned} \tag{8}$$

The optimized width of the transistors is calculated by substituting all the values in Eq. (9). The sizes of the transistors are assumed to be equal in dual CS stage

$$\begin{aligned} W &= \frac{3C_{gs}}{2C_{ox}L_{\min}} \\ W &= \frac{3 \times 0.1 \times 10^{-12}}{2 \times 8.64 \times 10^{-3} \times 0.18 \times 10^{-6}} \\ W &= 96.99\mathrm{mm} \end{aligned} \tag{9}$$

For DDC LNA, an additional design requirement is drain inductance of output stage inductors whose values are calculated by assuming C_{out} as 1 pF in Eq. (10). The inductance values of gate inductor L_d (10–15 nH) have been adjusted to vary the gain of the LNA

$$L_D = \frac{1}{4\pi^2 f_o^2 C_{out}} \tag{10}$$

The calculated values of components are used in the LNA design schematic with S-parameter test setup and simulated the performance of the designed circuit. With the transistor width of

97 μm, the DDC LNA achieved the optimum performance in terms of gain, NF, and impedance matching for this design. Both SDC and DDC LNA designs are also realized at a 5-GHz frequency by adopting the same procedure.

2.5.1. Performance metrics

The performance metrics namely gain and NF are derived commonly and used to analyze the circuit activity of the LNA design.

With reference to **Figure 12**, the overall dual CS stage transconductance can be expressed as

$$G_m = \left(g_{m1} + g_{m2}\right) Q_{in} \tag{11}$$

where Q_{in} is the effective Q of the amplifier input circuit. The increase in quality factor Q does not reduce the device transconductance, and therefore the overall stage transconductance remains unchanged. In general, the gain of a circuit is characterized by effective transconductance and load impedance.

At resonance frequency, the gain of LNA is expressed in terms of device transconductances g_{m1} and g_{m2} in Eq. (12),

$$A_V = \frac{\left(g_{m1} + g_{m2}\right) Q_L}{\omega_o C_{gs}} = \frac{g_m Q_L}{\omega_o C_{gs}} = \frac{\omega_T Q_L}{\omega_o} \tag{12}$$

where Q_L is the quality factor of the load element. The unity gain frequency is specified by, $\omega_T = \frac{g_m}{C_{gs}}$ and $g_m = g_{m1} + g_{m2}$. The device transconductance is evaluated in terms of unity gain frequency and gate-source capacitance.

The impact of Q on performance factors can be observed not only in theory but also in simulation. Using linearity test setup, the simulated value of gain saturation of SDC LNA is observed from the output 1-dB compression point of +6.16 dBm at 2.4 GHz RF frequency and with −2 dBm input referred value. **Figure 13** represents the equivalent noise model of the

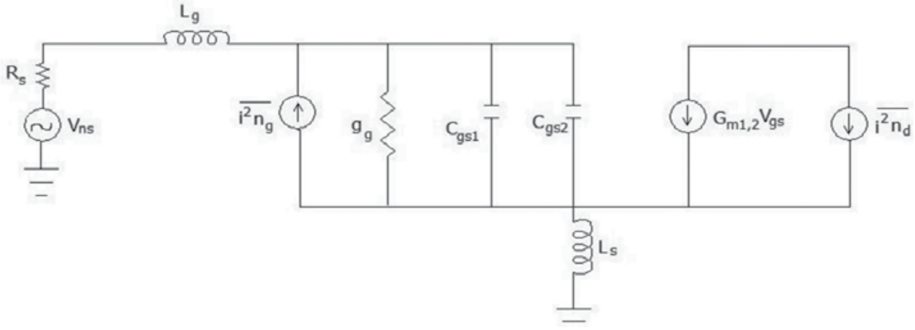

Figure 13. Equivalent noise model of input stage.

input stage of designed LNAs. The gate- and drain-induced noise current sources are shown with gate-source capacitances of the RF nMOS transistors.

The expressions for noise current densities have already been explained in previous sections. With reference to **Figure 13**, the noise factor is evaluated in terms of power spectral densities of drain noise current and gate noise current. It can be expressed as,

$$F = \frac{S_{Rs} + S_d + S_g}{S_{Rs}} \tag{13}$$

where S_{Rs} is the output noise power density due to the source impedance.

At series resonance condition, the output noise power density S_d due to the drain noise current can be written as

$$S_d = \frac{4kT\gamma g_{do}}{\left(1 + \frac{L_s}{R_s}\omega_T\right)^2} = \frac{4kT\gamma g_{do}}{\left(1 + \frac{g_m}{C_{gs}}\frac{L_s}{R_s}\right)^2} \tag{14}$$

where R_s is the source resistance and ω_T is the cutoff angular frequency.

In the same way, the output noise power density due to gate noise current, $S_{g,}$ can be written as

$$S_g = \frac{4kT\gamma g_{do}}{\left(1 + \frac{L_s}{R_s}\frac{g_m}{C_{gs}}\right)^2}\frac{\delta\alpha^2}{5\gamma}\left(1 - \left\|c^2\right\|\right)\left(1 + Q^2\right) \tag{15}$$

where c is the correlation factor between the gate and the channel noise current sources. The quality factor Q is a function of the source resistance and the gate-source capacitance of the MOSFETs.

By substituting Eqs. (14) and (15) in Eq. (16), the noise factor F can be expressed as

$$F = 1 + \frac{2\gamma}{\sqrt{5}\alpha}\left(\frac{f_o}{f_T}\right) \tag{16}$$

where f_o and f_T are design frequency and unity-gain frequency, respectively, and γ, α are channel noise factors.

Continuous improvement in technology will definitely lead to improve the noise performance at frequency of interest. The LNA can be designed to get NF equal to a minimum noise factor of the transistor, but also the lowest NF can be enumerated with the given CMOS technology scale.

Further, the NF of the DDC LNA is simplified, and it is given in Eq. (17)

$$NF = 10\log_{10}\left(1 + 2.4\left(\frac{f_o}{f_T}\right)\right) \tag{17}$$

By using Eqs. (12) and (17), the theoretical gain and noise figure of DDC LNA are calculated and are validated through simulations.

2.5.2. Performance analysis

SDC and DDC LNAs are designed and its performance is analyzed at 2.4- and 5-GHz frequencies. The devices and its characteristics used in designs are based on TSMC 0.18-μm RF CMOS process. Agilent's Advanced Design System (ADS) electronic design automation (EDA) tools are used for performance analysis. The various parameters analyzed here are S parameters, NF, and linearity to describe LNA performance with a supply voltage of 1.8 V. Scattering parameter (SP) analysis is the most useful linear small signal analysis for LNA. It is test setup by specifying the input, output ports, and the range of sweep frequencies. It is used for the characterization of forward gain (S_{21}), input impedance matching (S_{11}), output impedance matching (S_{22}), and reverse gain (S_{12}).

The graphs of S_{11} and S_{21} are provided in dB scale for both LNAs. SDC and DDC LNA graph of S parameter analysis with respect to RF frequency lies between the ranges of 1.0–3.0 GHz which are shown in **Figures 14** and **15**. The value of the input impedance matching of SDC LNA can be obtained from **Figure 14**. The results indicated by markers m1 and m2. Simulation result gives the input matching value as −10.99 dB which satisfies the requirement

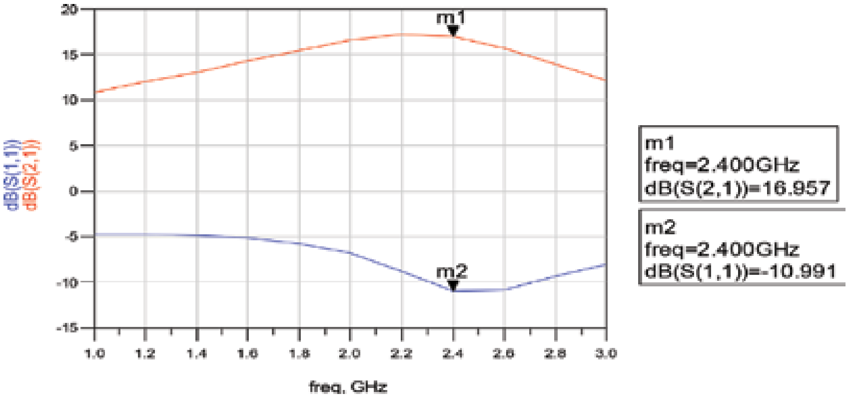

Figure 14. S-parameters of SDC LNA.

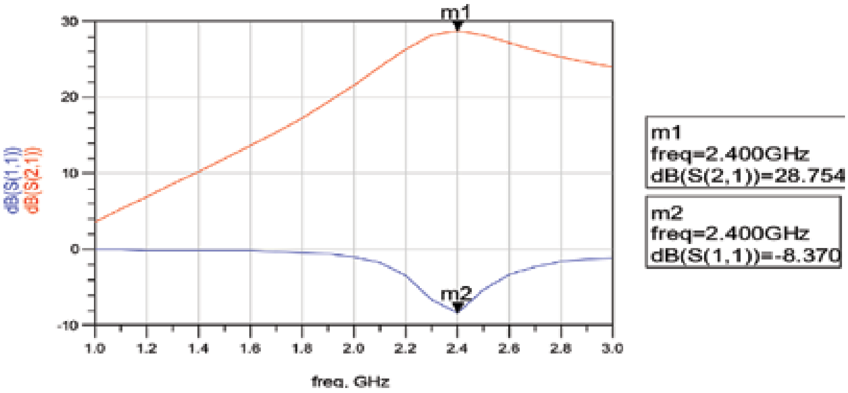

Figure 15. S-parameters of DDC LNA.

of matching constraint of LNA that is $S_{11} < -10$ dB at 2.4 GHz. The value of forward gain S_{21} is reached as 16.957 dB. Normally, the requirement of gain at 2.4 GHz is in the range of 15–30 dB. LNA satisfies the gain constraint but still the value is less. Moreover, it needs balun circuit additionally to process its output to the mixer as in the case of front-end design analysis. The graphs of S_{12}, S_{22} are not mentioned to avoid overlapping but traced during simulation.

To suppress the noise of the succeeding stages of front-end, the gain of LNA should be high. If the gain is too small, LNA cannot amplify the incoming weak signal to a desired value. If the gain is too large, LNA cannot degrade the linearity of the following mixer. It is one of the most important performance factors of LNA design. Therefore, DDC LNA satisfies the highest gain constraint at 2.4 GHz with optimized matching, and its performance is better than that of SDC LNA which is observed from results of **Figure 15**. The gain of DDC LNA is 28.75 dB. It is possible to feed the signal into the mixer directly due to its differential structure.

2.5.3. Noise figure

Noise figure is defined as the ratio of the total input noise to the total output noise due to the source. In general, the noise figure of LNA should remain below 5 dB to prevent inducing

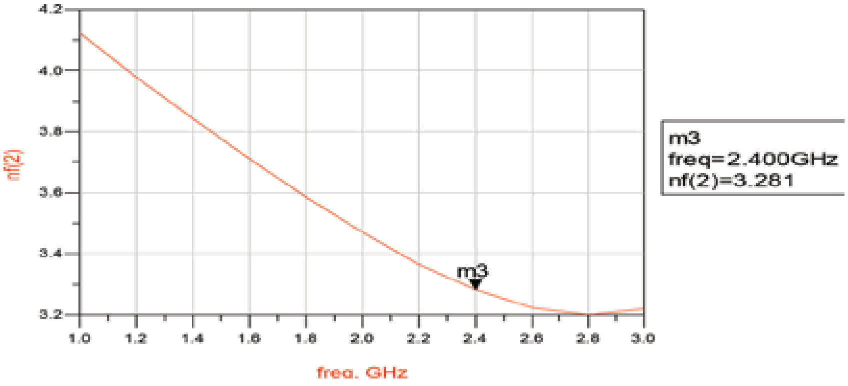

Figure 16. NF of SDC LNA.

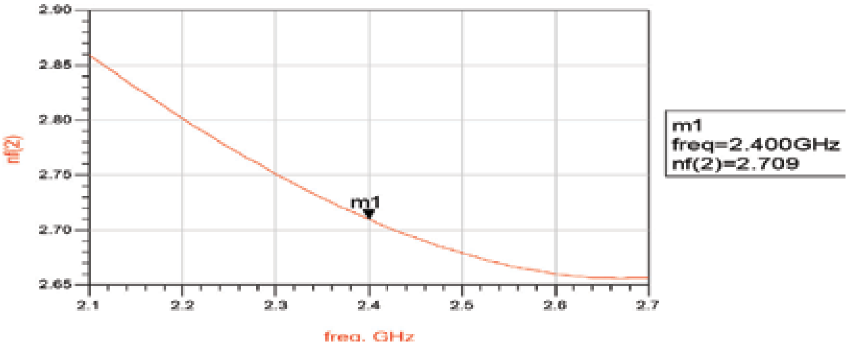

Figure 17. NF of DDC LNA.

noise problems in other stages of the receiver, like mixer, IF amplifier, etc. The NF graphs of the proposed LNA designs are given in **Figures 16** and **17**. The values of NF for SDC and DDC LNA are 3.281 and 2.7 dB, respectively. These values are highly desirable in wireless receiver. Typically, an NF of less than 4 dB is required in most standard CMOS LNAs. Both designs produce better NF and satisfy the noise reduction constraint. By making use of a single-stage structure, both SDC and DDC LNA designs satisfied the objectives of LNA. Simulation results show that DDC LNA structure presented here achieve better performances in what concerns S21, NF, and impedance matching at 2.4-GHz frequency. This analysis has also proved that DDC LNA achieved comparably good performance than other LNAs. This performance study helped us to select proper LNA architecture for front-end design.

Author details

Sumathi Manickam

Address all correspondence to: sumathi.ece@sathyabama.ac.in

Department of ECE, Sathyabama Institute of Science and Technology, Chennai, India

References

[1] Korotkov AS. Integrated receivers for wireless communications: A review. Russian Micro-Electronics. 2006;**35**(4):243-261

[2] Zolfaghari A, Razavi B. A low-power 2.4GHz transmitter/receiver IC. IEEE Journal of Solid-State Circuits. 2003;**38**(2):176-183

[3] Mihai AT, Sanduleanu M, Vidojkovic A. Receiver front-end circuits for future generations of wireless communications. IEEE Transactions on Circuits and Systems-II. 2008;**55**(4):299-303

[4] Aaron VD et al. An energy-aware CMOS receiver front-end for low-power 2.4GHz applications. IEEE Transactions on Circuits and Systems I. 2010;**57**(10):2675-2684

[5] Ragonese E et al. A 5-GHz highly integrated receiver front-end. Analog Integrated Circuits and Signal Processing, Springer Science Journal. 2007;**53**(1):3-7

[6] Razavi B. RF Microelectronics. Upper Saddle River, N.J: Prentice Hall; 2003. pp. 38-41, 48-50, 131-132, 138-143, 182-1873

[7] Youssef AA. Design guidelines for the noise optimization of a 0.18μm CMOS low noise amplifier. Analog Integrated Circuits and Signal Processing, Springer Science. 2002;**46**: 193-201

[8] Nieuwodt A et al. Design techniques for reducing the impact of component variations on narrow-band low noise amplifiers. Analog Integrated Circuits and Signal Processing, Springer Science Journal. 2008;**55**:189-193

[9] Liu B et al. An ultra-low voltage and ultra-low power 2.4GHz LNA design. Radio Engineering. 2009;**18**(4):527-531

[10] Bevin GP, Zhan J-HC. A 12mW, 7.5GHz bandwidth inductor-less CMOS LNA for multi-standard receivers. IEEE RFIC Symposium. 2007. pp. 82-86; DOI: 10.1109/RFIT.2007.4443926

[11] Leung B. VLSI for Wireless Communication. Prentice Hall; 2002

[12] Lee Thomas H. The Design of CMOS Radio Frequency Circuits. Cambridge, United Kingdom: Cambridge University Press; 1999. pp. 309-313, 319-321, 324

[13] Sumathi M. Performance and analysis of CML Logic gates and latches. IEEE International Symposium on Microwave, Antenna, Propagation and EMC Technologies for Wireless Communications; 2007. pp. 428-1432. DOI: 10.1109/MAPE.2007,4393548

[14] Sumathi M, Malarvizhi S. Design and performance analysis of 5 GHz CMOS RF front-end circuits for IEEE 802.11a application. European Journal of Scientific Research, published by Euro Journals. 2011;**54**(3):418-426

[15] Sumathi M, Malarvizhi S. Performance comparison of RF CMOS low noise amplifiers in 0.18-µm technology scale. International Journal on VLSI Design and Communication Systems, Published by AIRCC. 2011;**2**(2):45-54

Chapter 2

Study of the PIFA Antenna for RFID Applications

Loubna Berrich and Lahbib Zenkouar

Additional information is available at the end of the chapter

http://dx.doi.org/10.5772/intechopen.76564

Abstract

In this chapter, we did an introduction to radio frequency identification (RFID) technology, to define the different components of this system, then the frequencies of utilization for this application, and finally the advantages and disadvantages of this technology. Then we presented the design and simulation of a planar inverted-F antenna (PIFA) with a T-shaped slot. We studied the effect of changing the type of feed supply, the type of substrate, and the position of the connecting line between the ground plane and the radiating element. We chose the frequency of resonance of the antenna for the RFID applications at 5.8 GHz. The results obtained by the HFSS software are very satisfactory with a very minimal return loss.

Keywords: PIFA, RFID, slot, return loss, HFSS

1. Introduction

Radio frequency identification (RFID) is a technology used mainly to identify tagged items or to track their locations. The identification technology by radio frequency (RFID) uses electromagnetic fields to automatically identify and track tags attached to objects. The tags contain electronically stored information; passive tags collect energy from a nearby RFID reader's interrogating radio waves. Active tags have a local power source (such as a battery) and may operate hundreds of meters from the RFID reader. The first secure system identifying the friend and the foe (IFF) was the first form of RFID's technology. In 1948, Stockman (Stockman, 1948) proposed the identification from distance. He defended that it is possible to vary the amount of reflected power (also called load modulation antenna) by the alternation of the load of the tag antenna and consequently it has a modulation. Identification by radio frequency, known as RFID, is a smart technology that is very performed, flexible, and more suitable to automatic operations. RFID is an automatic identification method using radio waves to read the data contained in the devices called tag RFID. RFID technology is used to monitor, identify, and track objects, animals, and people away. The RFID system has two key features: RFID tag (label) and RFID reader. Today, this technology finds use in access controls, vehicle safety, animal tracking and patients in hospitals, and other applications [1].

The purpose of this chapter is the design and simulation of a PIFA with a T-shaped slot. We studied the effect of changing the type of feed supply, the type of substrate, and thus the position of the connecting line between the ground plane and the radiating element. The PIFA consist of a radiating element of length equal to the quarter wave and of a short circuit of several types: plane, tongue, or wire. This structure has advantages over a traditional patch antenna: cost and ease of manufacture, reduced size, thin profile, and bandwidth.

2. Principle of RFID

RFID is part of automatic identification technologies; this technology makes it possible to identify an object or a person, to follow the path and to know the characteristics at a distance thanks to label emitting radio waves, attached to or incorporated into the object or person. RFID technology allows reading of labels even without direct line of sight and can cross thin layers of materials [2, 3].

2.1. Components and operation of the RFID system

RFID includes labels, readers, encoders, and middleware which allow integrating the flow of data in the information system of the company.

2.1.1. The tag

One of the most used identification methods is to house a serial number or a sequence of data in a chip and connect it to a small antenna. This couple (chip + antenna) is then encapsulated in a support. These "tags" can then be incorporated in objects or be glued on products, **Figure 1**. The format of the data on the labels is standardized at the initiative of electronic product code (EPC) Global.

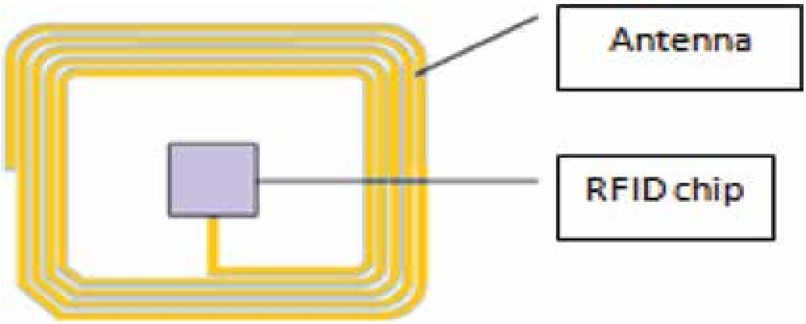

Figure 1. Tag antenna.

2.1.2. *The reader*

The reader/recorder is constituted of a circuit that emits electromagnetic energy through an antenna and an electronics that receives and decodes the information sent by the transponder and sends them to the data collection device. Not content to read RFID tags, he is able to write their content. The RFID reader is the element responsible for reading radiofrequency labels and transmitting the information they contain (EPC code or other, status information, cryptographic key, etc.) to the next level of the system (middleware). This communication between the reader and the label takes place in four stages:

1. The reader transmits by radio the energy necessary for the activation of the tag.
2. It launches a query querying the tags nearby.
3. It listens to answers and eliminates duplicates or collisions between answers.
4. Finally, it transmits the results obtained to the applications concerned.

2.2. The different types of tags and their technical specificities

2.2.1. *Active tags and passive tags*

To exploit the information contained in these labels, it is imperative to have the appropriate reader. This one emits radio waves toward the capsule which allows to supply it with energy (electromagnetic induction feed); in other words to activate it, these chips are not able to perform dynamic treatments but only to return static data (**Figure 2**).

2.2.2. *Passive tags (without battery)*

Without any external power supply, they depend on the electromagnetic effect of receiving a signal emitted by the reader. It is this current that allows them to power their microcircuits. They are inexpensive to produce and are generally reserved for volume productions. They

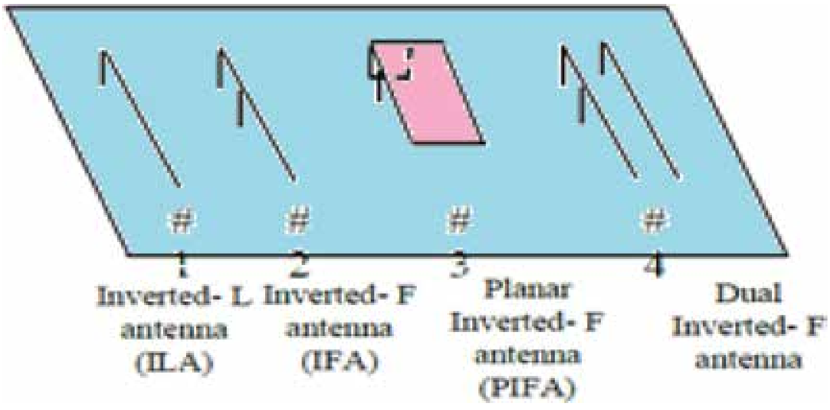

Figure 2. The different geometries of the inverted antennas.

are the ones we find especially in logistics and transport. They use different radio frequency bands according to their capacity to transmit remotely more or less important and through different substances (air, water, metal). The reading distance is less than 1 m. Low and high frequencies are standardized worldwide. These chips are stuck on the products for a follow-up. They are disposable or reusable depending on the case.

2.2.3. Semi-passive tags

These tags are similar to passive ID cards. They use similar technologies but with some important differences. They also have a small battery which works constantly, which frees the antenna for other tasks, in particular the reception of return signals. These tags are more robust and faster in reading and transmission than passive tags, but they are also more expensive.

2.2.4. Active tags

Active tags are the most expensive because they are more complex to produce and provide transmission functions, functions of capture or processing of the captured information, and either or both. Thereby, they need an onboard power supply you have to know that these labels prove particularly well adapted to certain functions, including the creation of authentication systems, security, anti-theft, etc.

Short, they are ideal for triggering an alert or alarm. They can emit several hundred meters.

2.3. Frequencies used in RFID

RFID systems generate and reflect electromagnetic waves. In particular, RFID systems must be careful not to disrupt the operation of other radio systems. We cannot, in principle, use only the frequency ranges specifically reserved for industrial, scientific, or medical applications. These frequency ranges are called industrial-scientific-medical (ISM). The main frequency ranges used by RFID systems are the low frequencies (125 and 134.5 kHz) and ISM frequencies: 6.78, 13.56, 27.125, 40.68, 433.92, 869.0, 915.0 MHz (not in Europe), 2.45, 5.8, and 24.125 GHz.

2.4. Advantages and constraints of radio frequency tags

The advantages of radio frequency labels over the barcode are

- The ability to update the content

Unlike bar code for which data are frozen once printed or marked, the content of the data stored in a radio frequency tag will be able to be modified, increased, or decreased by authorized stakeholders (read and write tags).

- Greater content capacity

Certainly bar codes that can store important content data appeared these last years, two-dimensional or matrix barcodes. However their use in industrial or logistic worlds remains problematic; they require conditions printing and reading. The commonly used barcodes are limited to data contents of less than fifty characters and in these extreme cases require an A4 or A5 size label. In a radio frequency tag, a capacity of 1000 characters is easily storable on 1 and 2 mm and can easily reach 10,000 characters in a logistics label affixed to a pallet.

- The marking speed

The barcode in a logistic context most often requires the printing of a paper medium. Handling and labeling are manual or mechanical operations. The radio frequency labels can be included in the handling support or in the packaging from the outset. Data concerning objects contained or transported are written in a split second at the time of the constitution of the logistics or transport unit, without further manipulation.

- Security of access to the content

Like any digital medium, the radio frequency tag can be protected by password in writing or reading.

The data can be encrypted. In the same label, a part of the information can be freely accessible and the other protected. This faculty makes the RF tag, a tool adapted to the fight against theft and counterfeiting.

- Longer life

In applications where the same object can be used multiple times, as the identification of handling supports, or the consignment of the container, a radio frequency tag can be reused 1,000,000 times.

- Greater positioning flexibility

To enable the automation of the reading of the logistic barcode labels, standardization bodies like EAN, have defined positioning rules on logistics units. With the radio frequency tag, it is possible to abstract constraints related to optical reading; she does not need to be seen. It is enough for him to enter the field of the reader so that his presence is detected.

- Better protection against environmental conditions

RFID tags do not need to be positioned outside the object to be identified. They can therefore be better protected from attacks related to storage, to the handling or transport. In addition, their operating principle does not make them susceptible to soiling or various spots that interfere with the use of the barcode.

2.5. Constraints of radio frequency labels

- Disturbance by the physical environment

The reading of radio frequency tags is disturbed by the presence, for example, of metals in their immediate environment. Solutions must be studied case by case to minimize these disturbances.

- Disturbances induced by the labels between them

In many applications, several radio frequency tags may occur at the same time in the reader's field voluntarily or involuntarily. This can be wanted in store, at the time of checkout or between anti-theft doors.

In this last case just detect a stolen object, a label not inhibited by the box. Technology allows it today. More complex is the need to identify and read the contents of several labels in a field without forgetting; to do this the readers use algorithms or anti-collision techniques, etc.

- Sensitivity to parasitic magnetic waves

In certain circumstances, RFID reading systems are sensitive to spurious electromagnetic waves issued by computer equipment (computer screens) or lighting systems more generally by electrical equipment. Their use must be tested taking into account the environment.

- The regulatory constraints related to the impact on health

This question has been debated for a few years, in particular concerning the anti-theft gates and cell phones. Passive tags themselves present no risk whatever their number is since they are active only when they are in the field of a reader. The studies therefore focus on readers and aim to define the regulatory criteria of their emission power to prevent them from creating disruptions.

2.6. Examples of applications

RFID tag applications are already very numerous; we give some examples of the possibilities offered by this technology:

- Tracking and sorting luggage

The airlines are currently studying the replacement of RFID tags.

- The automatic toll

Many management companies' toll motorways have already put in place systems subscription based on RFID tags and microwave, placed in vehicles. Subscribers benefit in special way of crossing toll gates. Payment is made without stopping the vehicle, by simply reading his identification.

- Access control

RFID tags are already used for access control of buildings or car parks.

- Animal tracking

More and more applications of animal traceability are growing, whether it's ear tags on farm animals or the subcutaneous labels for horses or pets. In all cases, it's about ensuring animal traceability for the purpose of sanitary control or the quality of herds.

- Cleaning clothes

For the cleaning of work clothes, companies are putting in place systems uniform identification based on RFID tag with a diameter of 20 mm and a thickness of 2.5 mm, the frequency 13.56 MHz read/write at 20 m.

These labels are attached to the garment; they resist washing operations. They allow a follow-up of the washing operations and easy identification of the wearer of the uniform.

- Waste collection

In Europe as well as in Japan and the United States, household or industrial waste collection companies are concerned with improving the load distribution of garbage collection and treatment. The principle is to equip each bin or container of an RFID tag and the collection trucks for readers and weighing system, so that each operation can automatically identify the "producer" and measure the weight of the collected material.

- Supply chain management

In logistics, four levels of applications can be distinguished:

- Delivery
- Home
- In transit
- Local

At the time of shipment, labels can facilitate the collection of products and the constitution of pallets, sorted by destination and loading control. The label may contain, in addition to the product identification, or the contents of a pallet, that of the manufacturing lot number, consignee identification, order number, handling details, etc. This information collected at the time of loading can be stored in the RFID tag container or means of transport to facilitate checks during transit, customs, access, or exit authorization. Similarly, upon receipt of the goods, the data can be collected to automatically perform audits and update the inventory and make reconciliations with commercial documents or EDI messages. In transit, the label is used to trace the product at each point of loading and unloading or simply passing. Thus, the sender can be informed at any time transport stream. Locally, labels allow product inventory but also media management handling and equipment (gas bottles, etc.).

3. The choice of the PIFA

There are several types of antennas for RFID applications; among these antennas we mention that antennas of the planar inverted-F antenna (PIFA) type are the most used in portable devices for GSM, Wi-Fi, RFID applications, etc. due to their low manufacturing cost and their compactness, as it has very small dimensions compared to a half-wave antenna. The PIFA is obtained by placing the short circuit (plane, wired, or tongue-like) between the half-wave resonator and the ground plane, at the precise point where the electric field vanishes for the fundamental mode. This makes it possible to overcome one half of the resonator and thus have an X/4 resonance. This type of antenna has the advantage of presenting a desired quasi-isotropic radiation in RFID applications, since the relative orientation of the tag relative to the reader is uncertain.

4. Study and design of a PIFA

4.1. Structure of a PIFA

The PIFA is the result of the transformation of the inverted-F antenna (IFA) from a horizontal wire element to a planar structure to compensate for his loss of maladjustment and improve its radiation characteristics. The planar inverted-F antenna (PIFA) is a quarter wave antenna integrated and miniaturized by comparing it with monopole antennas. Also, it has good advantages over a traditional patch antenna (cost and ease of manufacture, small size, and bandwidth). The inverted plane antenna F is a rectangular microstrip antenna powered by a coaxial probe. It is called an inverted-F antenna because the side view of this antenna resembles the letter F with its face down [4, 5–9].

The ILA consists of a short vertical monopole with the addition of a long horizontal arm at the top. Its input impedance is almost equivalent to that of the short monopole with the addition of the reactance caused by the horizontal wire above the ground plane. In general, it is difficult to match the impedance to a power supply line since its input impedance consists of low resistance and high reactance. Adding the additional inverted-L element adjusts the input impedance of the antenna. The impedance bandwidth of the IFA antenna is less than 2% on the center frequency. One way to increase the bandwidth of the IFA antenna is to replace the upper horizontal arm with a plate oriented parallel to the ground plane to form the inverted plane antenna F (PIFA). More generally called planar inverted-F antenna (PIFA) in the scientific literature, they have the advantage of being compact with a wide bandwidth. **Figure 3** shows the different elements of the PIFA [4].

Figure 4 shows the side view of the PIFA.

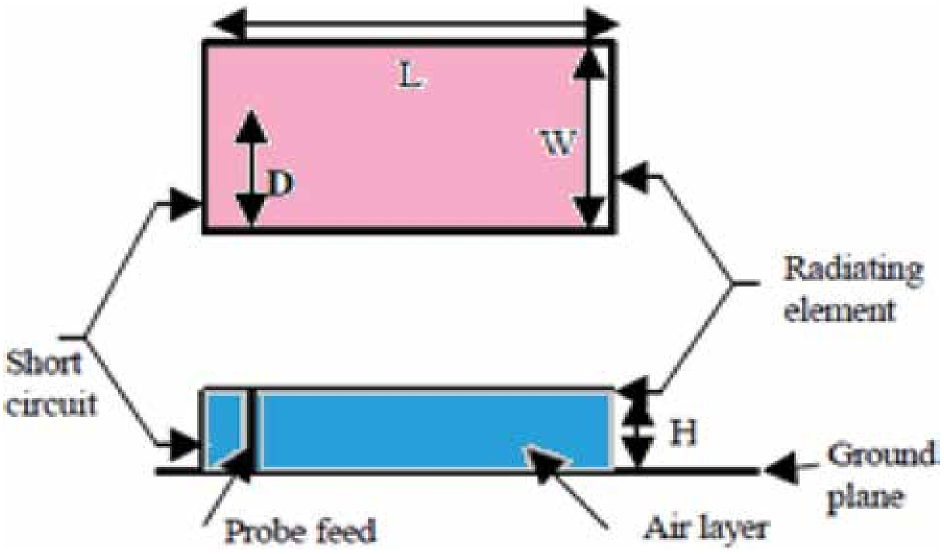

Figure 3. The PIFA.

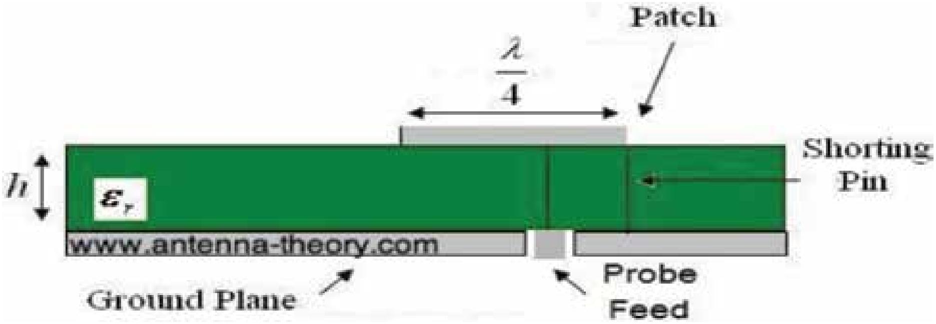

Figure 4. The PIFA (side view).

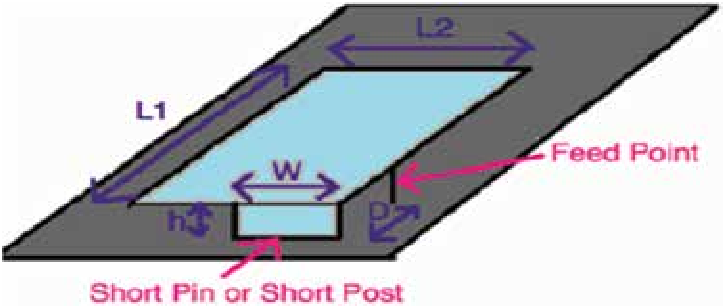

Figure 5. PIFA.

More generally called planar inverted-F antenna (PIFA) in the scientific literature, they have the advantage of being compact with a large bandwidth; it is mainly characterized by the presence of a plate that plays the role of a short circuit between the radiating patch and the ground plane as shown in **Figure 5** where h is the height of the short circuit, W its width, and D the distance between the short circuit and the feed point of the patch antenna.

The resonance frequency of a PIFA is approximated by equation (Eq. (1)).

$$L_1 + L_2 - W = \frac{\lambda}{4} \tag{1}$$

With L_1 and L_2 the dimensions of the radiating patch, λ is the calculated wavelength for the medium separating the patch and the ground plane [4, 5–9].

5. Results and discussion

The antenna proposed is an antenna consisting of a rectangular patch with a width W = 20 mm and a length L = 18 mm placed on a substrate with a width W = 30 mm and a length L = 30 mm using FR4_epoxy, characterized by a relative permittivity of 4.4, a relative permeability of 1, tgδ of the dielectric losses = 0.02, and a thickness e = 0.7 mm. The antenna is connected to the ground plane through a rod with a height h = 10 mm and a width of 10 mm, **Figure 6**.

5.1. Effect of the slot

In contrary to a conventional PIFA, the short circuit is not realized over the entire width of the antenna but through a flat short circuit which is a metal tongue of width W. A T-slot with a width of 0.5 mm in the metal radiating element ensures a good match between the impedance of the chip and the input impedance of the PIFA. The geometry of this antenna is shown in **Figure 7**.

The Ansoft high frequency structure simulator (HFSS) logger is a very high-performance microwave simulator that models and simulates 3D global fields radiated by microwave structures (antennas, filters, guides, connectors, PCBs, etc.). Characteristics for antennas such as (Gain, SAR, VSWR, Sij, etc.). It is based on the finite element model which consists in solving the equations of the field in discrete points defined in an orderly way in the complete domain of the structure. It directly solves the Maxwell equations in their differential form by replacing the differential operators by difference operators, thus realizing a discretization approximation.

The results of the both PIFA antennas with and without slot at 5.8 GHz are:

Figure 8 shows the return loss of the PIFA, S11 = −21 dB with a bandwidth equal to 200 MHz.

Figure 9 shows the reflection coefficient of the PIFA, S_{11} = −33 dB with a passband equal to 150 MHz.

Figure 9 shows that our antenna is well adapted.

Another essential character for knowing the parameters of the antenna is the SWR of the antenna PIFA.

Figure 10 shows the SWR of the antenna PIFA SWR = 1.09 < 2.

The SWR parameter of the PIFA fitted with a T-slot is less than 2 (**Figures 11–13**).

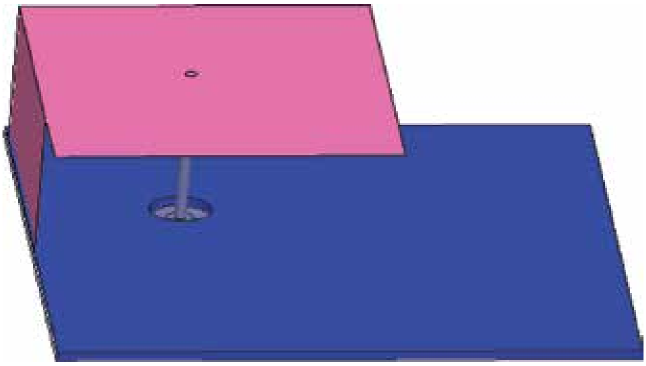

Figure 6. The structure of the PIFA on HFSS.

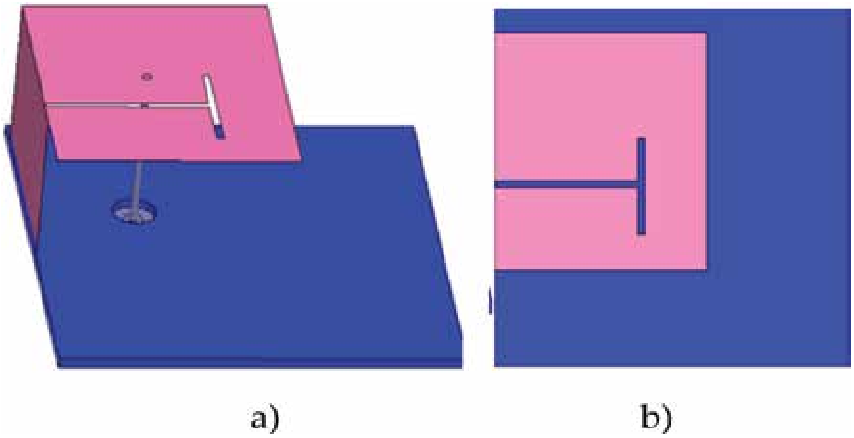

Figure 7. The structure of the PIFA with T-slot on HFSS. (a) side view and (b) top view.

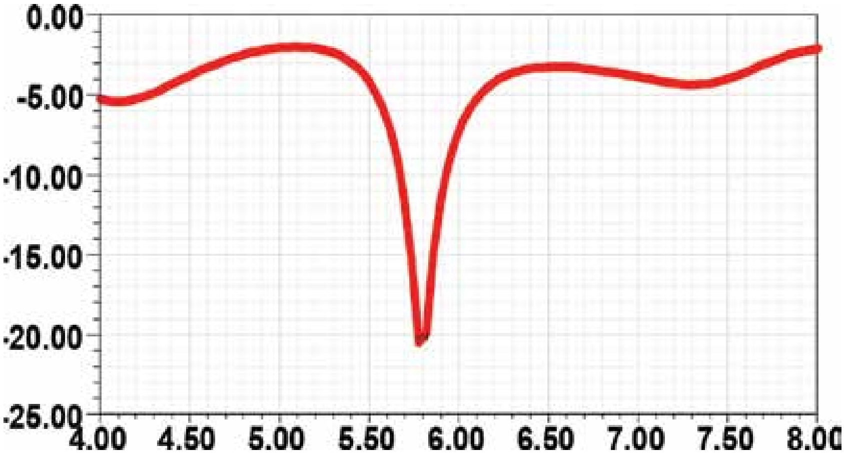

Figure 8. Return loss of the PIFA.

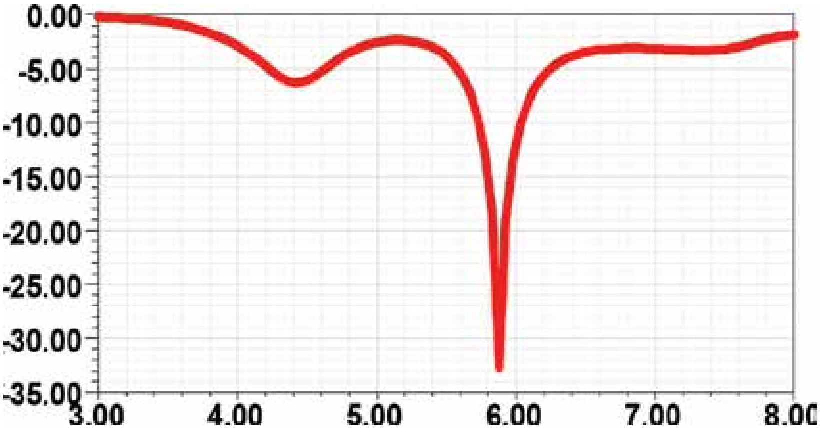

Figure 9. Reflection coefficient of the PIFA.

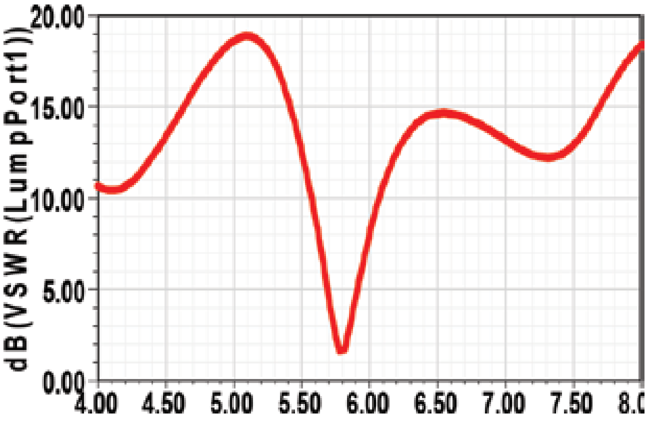

Figure 10. The SWR of the PIFA.

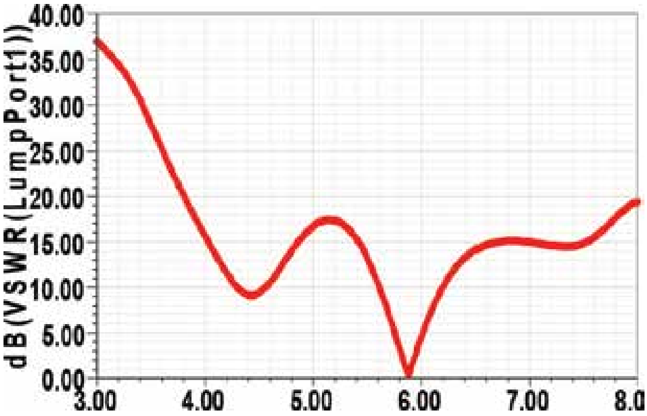

Figure 11. The SWR of the antenna with T-slot.

The appearance of **Figure 14** shows the gain of the PIFA without slot equal to 2.4 dB around the resonance frequency 5.8 GHz.

The appearance of **Figure 15** shows the gain of the PIFA is equal to 3.4 dB around the resonance frequency 5.8 GHz (**Table 1**).

From the results obtained, we notice that the T-slot has a positive effect on our PIFA: a decrease in return loss and an increase in gain.

5.2. The effect of changing the substrate type

Changing the substrate has a major effect on the antenna especially on the return loss and the resonance frequency. In this work we studied the effect of substrate change; we used three types of substrate: FR4 epoxy with a permittivity equal to 4.4, Rogers RT/Duroid 6006 with a permittivity equal to 6.15, and Rogers RT/Duroid 5880 with a permittivity equal to 2.2.

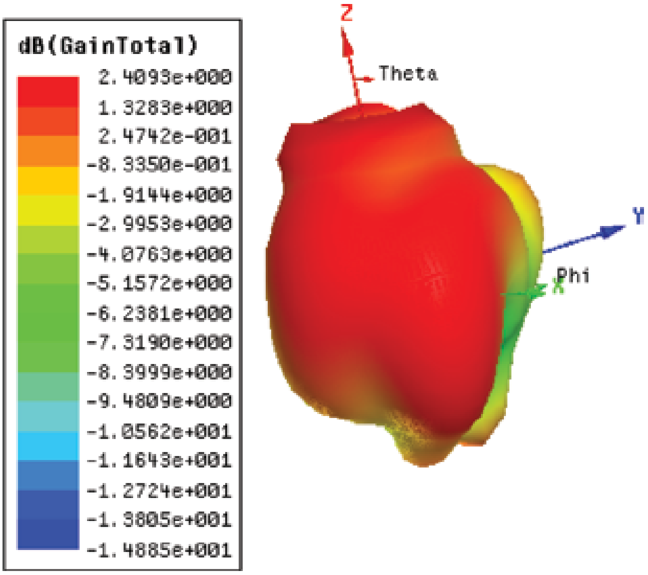

Figure 12. The 3D radiation pattern of the PIFA.

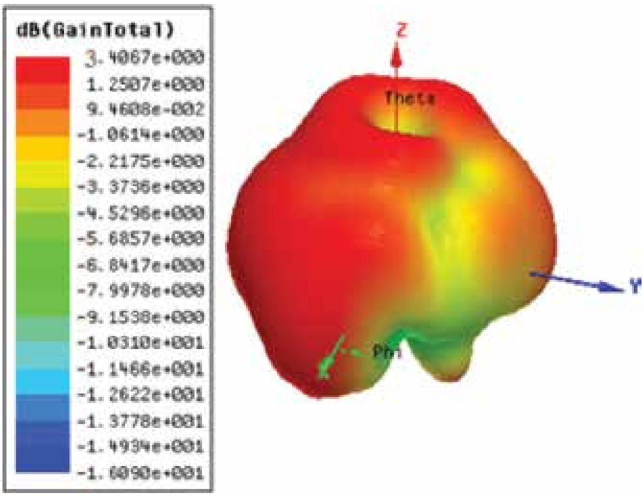

Figure 13. The 3D radiation pattern of the PIFA with T-slot.

Figures 16–18 show the reflection coefficient of the PIFA for the three substrates used:

The change of substrate has a major effect on the antenna especially on the reflection coefficient and the resonant frequency used in this work. To achieve the resonance frequency 5.8 GHz, it is necessary to modify the dimensions of the radiating element, which automatically influences the reflection coefficient.

The following table summarizes the results of the three simulations:

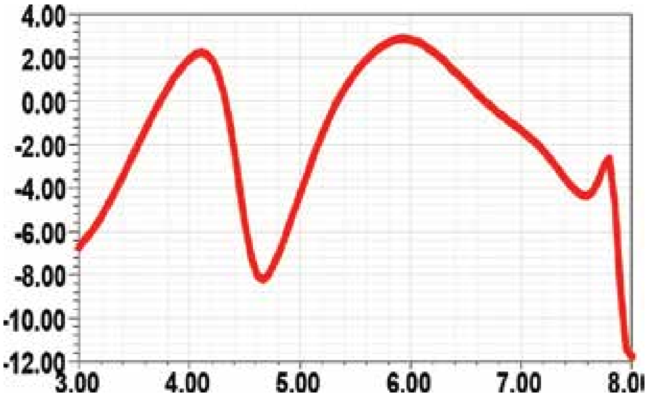

Figure 14. Gain of the PIFA.

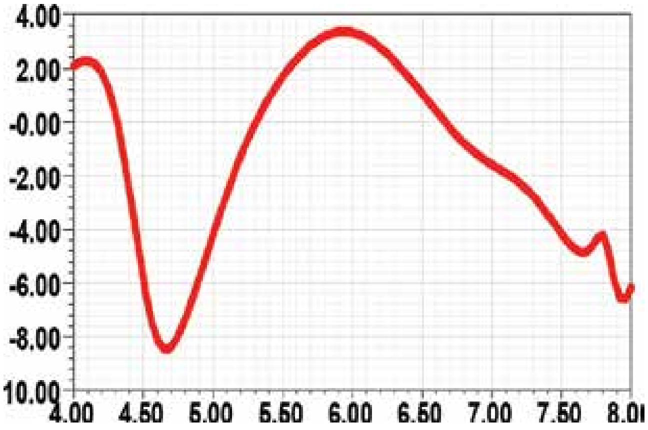

Figure 15. Gain of PIFA with slot.

	PIFA without T-slot	PIFA with T-slot
S_{11}	–21 dB	–33 dB
Gain	2.4 dB	3.4 dB
SWR	1.09	1.01

Table 1. Recapitulation of the results.

From **Figures 16–18** and **Table 2**, we noted that for the substrate FR4 epoxy (εr = 4.4), the antenna resonates at (5.8 GHz) with a return loss is equal to −33 dB.

For RO6006 (ε_r = 6.15) the antenna resonates at (5.78 GHz), and the return loss is −26 dB, but for Ro5880 (ε_r= 2.2), the antenna has a resonant frequency (5.8 GHz) with a return loss of −17 dB.

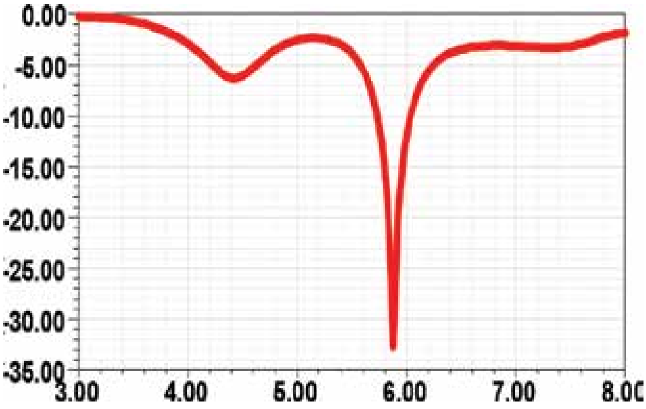

Figure 16. Return loss (epoxy FR4).

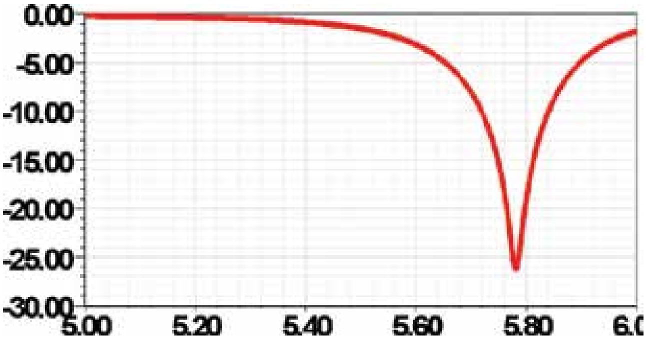

Figure 17. Return loss (Rogers RT/Duroid 6006).

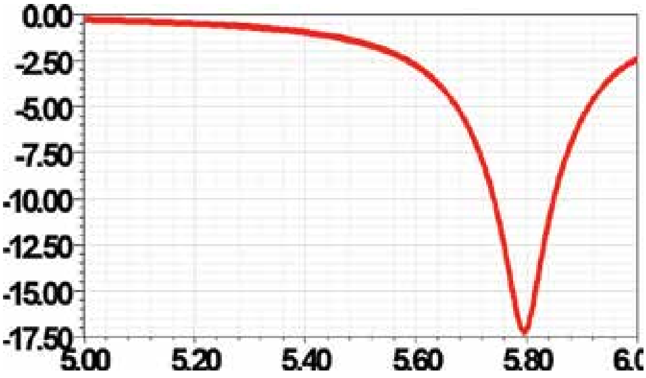

Figure 18. Return loss (Rogers RT/Duroid 5880).

5.3. Changing the position of the line

The connecting line between the substrate and the radiating element of the PIFA can take several positions, either at the end or at the center of the radiating element.

In this study we compared the results of simulations of the PIFA with three different positions of the connection line.

Figures 19–21 present the return loss of the antenna PIFA for the three positions.

	RO5880	FR4 epoxy	RO6006
Width	32 mm	30 mm	29 mm
Length	26 mm	26 mm	26 mm
f_r	5.8 GHz	5.8 GHz	5.78 GHz
S_{11}	−17 dB	−33 dB	−27 dB

Table 2. Recapitulation of the results.

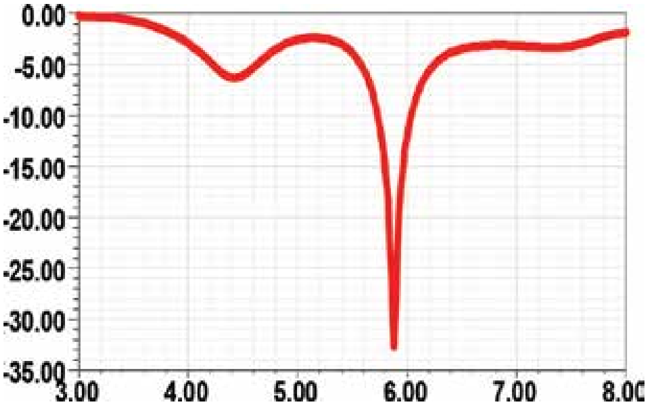

Figure 19. Return loss (Position 1).

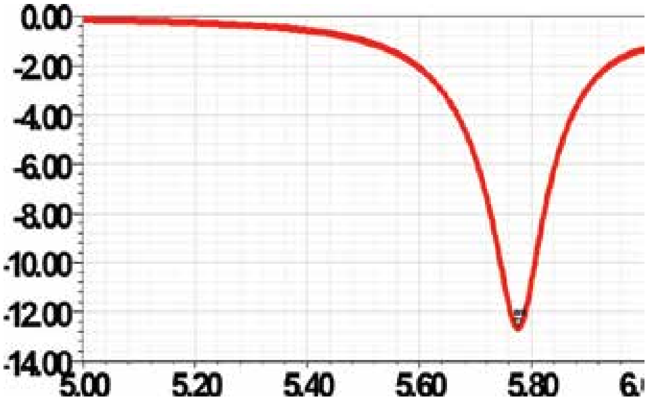

Figure 20. Return loss (Position 2).

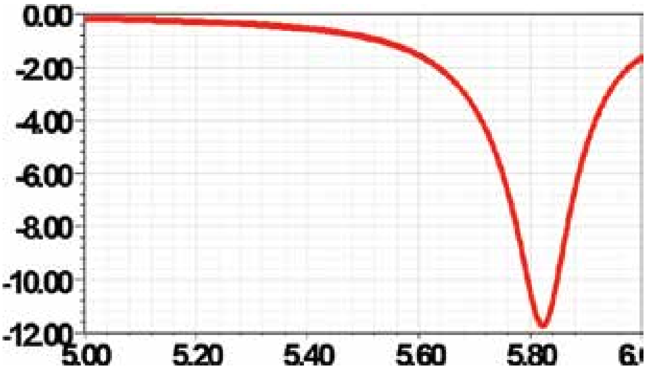

Figure 21. Return loss (Position 3).

Position	P_{x1}	P_{x2}	P_{x3}
S_{11}	−33 dB	−20 dB	−17 dB

Table 3. Recapitulation of the results.

From **Figures 19–21** and **Table 3**, we noted that for = 10 mm the antenna resonates at (5.8 GHz) with a return loss is equal to −33 dB. For p_{x2} = 15 mm the antenna resonates at (5.78GHz) and the return loss is –26 dB, but for p_{x3} = 20 mm, the antenna has a resonance frequency (5.8 GHz) with a return loss is of –17 dB.

Based on the results we deduced that as one moves away from the end of the radiating element the return loss becomes greater.

5.4. Change of power supply type

Microstrip feed line and the coaxial cable feed are easy to implement; nevertheless this type of power supply generates of parasitic radiation, which affects the radiation pattern. In this study we chose to feed our antenna via a coaxial cable and secondly via a microstrip line. We will compare the results obtained for these two feeding modes. To use these power modes, the microstrip line or the coaxial cable is adapted. For printed antennas this is parameter S_{11} which reflects the adaptation of the antenna.

In this work, we chose to feed our antenna via a microstrip line and secondly via a coaxial cable. We will compare the results obtained for these two modes of feeding. To use these power modes, it is necessary that the microstrip line or the coaxial cable is adapted. For printed antennas it is the parameter S11 that reflects the adaptation of the antenna. Otherwise, an antenna is considered suitable and isolated when the parameter S_{11} is less than −10 dB, which equates to at least 10% of losses. **Figures 22** and **23** show the reflection coefficient of the PIFA fed via a coaxial cable and a microstrip line.

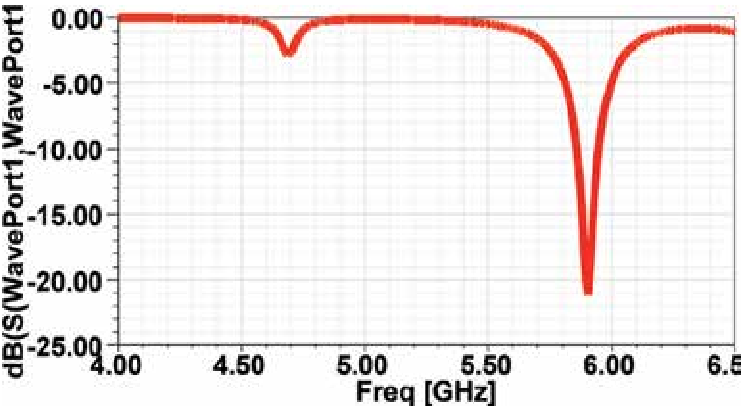

Figure 22. Return loss of the antenna supplied via microstrip line.

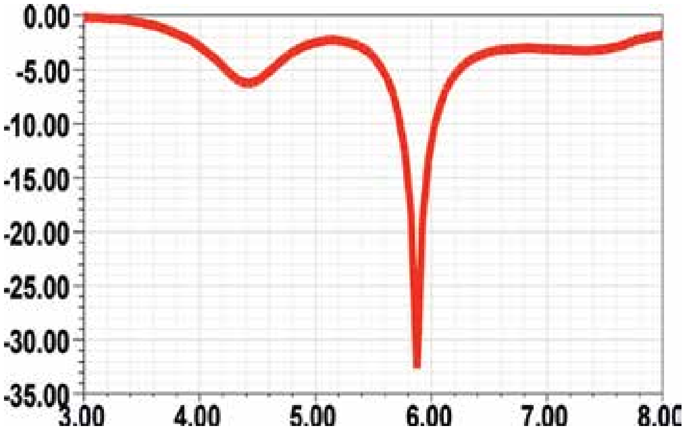

Figure 23. Return loss of the antenna supplied via coaxial cable.

From **Figures 22** and **23**, we notice that the reflection coefficient PIFA powered by coaxial cable is equal to −33 and −22 dB for the antenna powered by a microstrip line. So feeding via a coaxial cable is the best technique to power a PIFA.

6. Conclusion

In this chapter, in the first part, we did an introduction to automatic identification technology, to define the different components of this system, then the frequencies of utilization for this application, and finally the advantages and disadvantages of this technology. In the second part, we presented the design and simulation of a PIFA adapted by a T-slot and powered by a coaxial cable. We studied the effect of changing the type of feed and the substrate type and thus the position of the connecting line between the ground plane and the radiating element.

We chose as the resonance frequency of the antenna for RFID applications the frequency 5.8 GHz. We compared the results of simulations obtained by the Ansoft HFSS software. The results obtained are in perfect harmony for RFID applications, either in terms of frequency or bandwidth. Similarly, the significant maxima have been obtained for parameters S11, Gain, SWR, and radiation pattern.

Author details

Loubna Berrich* and Lahbib Zenkouar

*Address all correspondence to: loubna.berrich@gmail.com

Department of Electrical Engineering, Mohammadia School of Engineers, Research Team in Smart Communications (ERSC), E3S Research Center, Rabat, Morocco

References

[1] Stockman H. Communication by means of reflected power. Proceeding of the IRE. 1948:1196-1204

[2] Labdt I, Los Almas N, Lab N. The history of RFID. Potentials IEEE. 2005;**24**(4):2-11

[3] Balanis A. Antenna Theory Analysis and Design; New York: Wiley; 1997

[4] Berrich L, Lahsaini M, Zenkouar L. Comparison of rectangular and circular microstrip antenna's array for a WIFI and RFID applications at 2.45 GHZ and 5.8 GHZ. International Journal on Communications Antenna and Propagation (I.Re.C.A.P.). 2015;**5**:212-212

[5] Berrich L, Zenkouar L. PIFA antenna for RFID application at 5.8 GHZ. ARPN Journal of Engineering and Applications Sciences. 2017;**12**(15):4565-4569

[6] Belhadef Y, Boukli Hacene N. Antennas design for multistandard terminals. World Applied Sciences Journal. 2011;**14**(10):1523-1529

[7] Berrich L, Zenkouar L. Microruban dipole antenna for RFID applications at 2.45 GHz. International Journal of Electrical and Computer Engineering IJECE. 2016;**6**(6):2891-2899

[8] El ouadih A. Oulad-said A. Conception d'une Antenne PIFA Tribande avec Fente pour Integration sur les Stations Mobiles de Réseaux de Télécommunication: Telecom'2013 & 8émé JFMMA; 2013

[9] El Ouadih A, Oulad-said A, Mrabet Hassani M. Design and simulation by HFSS of a slim UWB PIFa antenna. World Journal of Engineering and Technology. 2013;**1**:17-22

Chapter 3

Low-Dimensional Materials for Disruptive Microwave Antennas Design

Charlotte Tripon-Canseliet and Jean Chazelas

Additional information is available at the end of the chapter

http://dx.doi.org/10.5772/intechopen.79514

Abstract

This chapter is devoted to a complete analysis of remarkable electromagnetic properties of nanomaterials suitable for antenna design miniaturization. After a review of state of the art mesoscopic scale modeling tools and characterization techniques in microwave domain, new approaches based on wideband material parameters identification (complex permittivity and conductivity) will be described from impedance equivalence formulation achievement by de-embedding techniques applicable in integrated technology or in free space. A focus on performances of 1D materials such as vertically aligned multi-wall carbon nanotube (VA-MWCNT) bundles, from theory to technology, will be presented as a disruptive demonstration for defense and civil applications as in radar systems.

Keywords: nanotechnology, electromagnetism, multiscale modeling, 3D full-wave analysis

1. Introduction: miniaturization challenges in microwave domain

Material band gap engineering opens new avenues for the optical control of these new nanomaterials and achieves a drastic miniaturization degree for wideband frequency devices. Electronics and optoelectronics applications, based on materials with a bandgap in the band structure, would require combinations of atomically thin two-dimensional (2D) semiconductors in hybrid devices. The feasibility of separating and even synthesizing atomically thin layers of MoS2, MoSe2, WSe2 and WS2 has been demonstrated, and this offers new perspectives for the development of electronics and optoelectronics based on atomically thin films. This research area relies on the investigation of atomically thin two-dimensional (2D) systems, including growth and studies of atomically thin 2D crystals beyond graphene; investigation of their electronic and optical properties; development of applications of hybrid systems in functional device; and growth and preparation of new layered systems for spintronics. By reducing the dimensionality of materials, a new class of devices could be foreseen which are ultra-thin (nanometers), ultra-light, flexible, wearable, bendable and energy harvesting.

This emerging research area deals with technological breakthroughs benefits from quantum effects exaltation by the use of nanomaterials/nanotechnologies in the definition and description of next future electromagnetic (EM) nanosystems. This area addresses and brings responses to the main challenges in the design of future EM systems such as: (1) how quantum effects will improve the performances of EM systems; (2) how to design an EM system based on nanomaterials; (3) how to control or reconfigure a system based on nanomaterials; and (4) how to define and design an EM nanosystem.

Emerging nanotechnologies dedicated to 1D and 2D materials processing offer today the possibility of design innovations in broadband reconfigurable EM systems. By enabling exceptional electromagnetic material properties, high degree of confinement of electromagnetic waves, near field coupling access and drastic miniaturization.

Material engineering starts from energy band profile study, which legislates excitonic energy transfers allowing charge carriers transport. Since decades, conventional electronics and optoelectronics components benefits from well-known bulk semiconducting materials properties in which carriers can easily diffuse in three dimensions following parabolic band profiles. By eliminating progressively one spatial dimension, energy transfer possibilities become more and more confined as they are governed by sharp transitions sustained by step or Dirac band profile, such as in 2D, 1D or 0D materials. Furthermore, monoatomic layer materials defined by atoms arrangement witness even more in-plane anisotropic properties from nonsymmetrical lattice configuration or chirality. From these statements, majority carriers diffusion and transport optimization are under study by surface functionalization techniques and heterostructures process elaboration.

Today, it becomes obvious that by promoting the confinement of electromagnetic interactions new electronic and optoelectronic devices design optimizations will move toward the definition of 2D structures supporting surface wave propagation.

2. Carbon-based materials as promising low-dimensional materials technologies for electronic systems

Low-dimensional materials belong to a new class of materials in which space confinement appears in one or two dimensions. Carbon-based materials such as graphene and SW/MW CNTs represent the most mature material family in nanotechnologies that could strongly alleviate the silicon technology limits compared to alternative approaches such as Si-Ge and III-V high mobility semiconductors, with particular emphasis on their possible applications in microwave and mmm wave electronics.

Indeed, the extraordinary mechanical and electrical properties of CNTs make them ideal candidates as building blocks for RF ICs. They can be metallic or semiconducting depending on their chirality. The high conductivity of single-wall metallic nanotubes (SWNT) or multi-wall nanotubes (MWNT) allows for designing simple actuation systems based on the direct electrostatic coupling with metallic gates. These properties make them particularly suitable for both basic building blocks of active components as well as electrical interconnects.

Graphene has emerged as a promising material for electronics in the last years. It is chemically and thermally one of the most robust materials available. Furthermore, it has proven potential for ultra-high frequency electronics. In less than 6 years from the material discovery by A. Geim and K. Novoselov, and despite the remaining technological issues still under heavy development, scientist has managed to provide proof of concept active devices (FETs) operating at frequency comparable to the state of the art. Especially for wireless applications, an important factor is that graphene microwave devices can be easily accommodated to the standard 50 W impedance. Additionally, the nonlinear behavior of the I-V dependence of graphene contacted with metals can be used to multiply or detect RF signals. Moreover, graphene growth is rapidly progressing from a purely scientific field into the world of applications (**Tables 1** and **2**).

2.1. Single- and multi-walled carbon nanotubes (SW/MWCNT) as 1D materials candidates

The main growth techniques recently studied concern in-situ growth by CVD/PECVD or dispersed solutions or external deposition techniques on substrate by the use of dielectrophoresis (DEP) and droplet techniques.

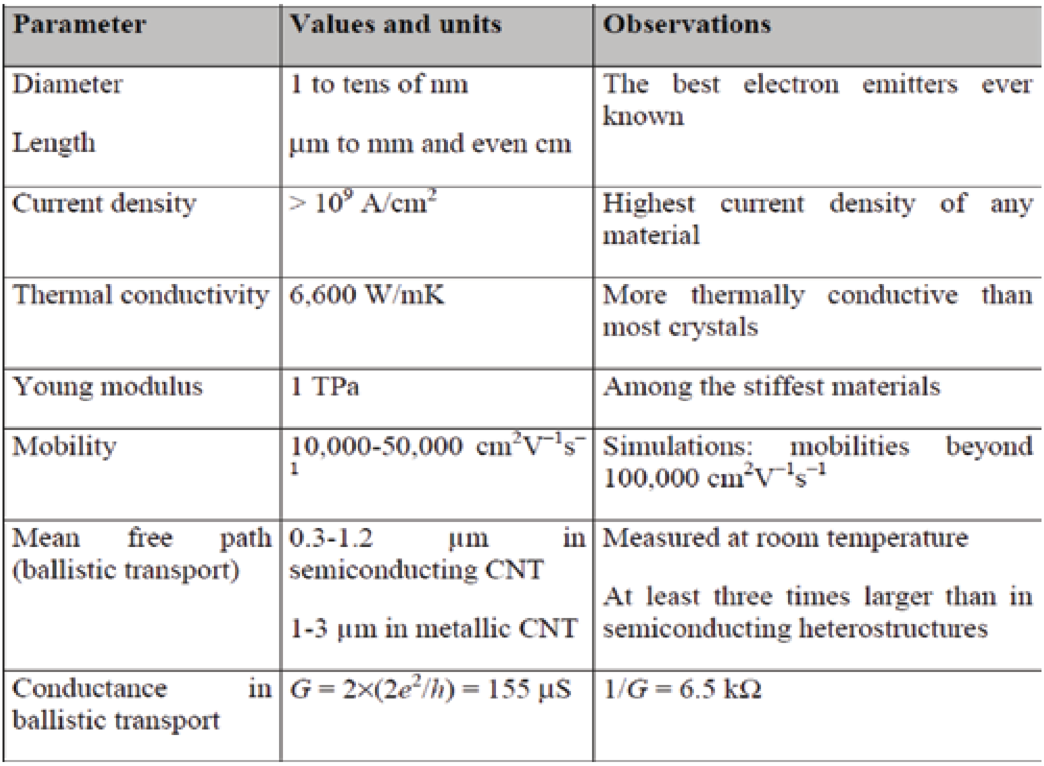

Parameter	Values and units	Observations
Diameter Length	1 to tens of nm µm to mm and even cm	The best electron emitters ever known
Current density	$> 10^9$ A/cm^2	Highest current density of any material
Thermal conductivity	6,600 W/mK	More thermally conductive than most crystals
Young modulus	1 TPa	Among the stiffest materials
Mobility	10,000-50,000 cm^{2}V^{-1}s^{-1}	Simulations: mobilities beyond 100,000 cm^{2}V^{-1}s^{-1}
Mean free path (ballistic transport)	0.3-1.2 µm in semiconducting CNT 1-3 µm in metallic CNT	Measured at room temperature At least three times larger than in semiconducting heterostructures
Conductance in ballistic transport	$G = 2\times(2e^2/h) = 155$ µS	$1/G = 6.5$ kΩ

Table 1. Summary of CNT properties.

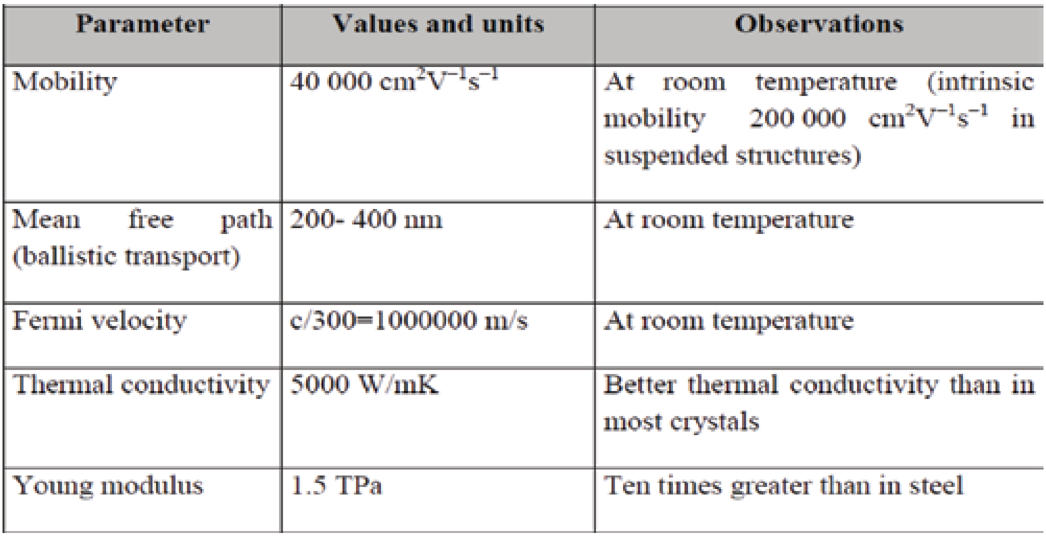

Parameter	Values and units	Observations
Mobility	40 000 $cm^2V^{-1}s^{-1}$	At room temperature (intrinsic mobility 200 000 $cm^2V^{-1}s^{-1}$ in suspended structures)
Mean free path (ballistic transport)	200- 400 nm	At room temperature
Fermi velocity	c/300=1000000 m/s	At room temperature
Thermal conductivity	5000 W/mK	Better thermal conductivity than in most crystals
Young modulus	1.5 TPa	Ten times greater than in steel

Table 2. Summary of graphene properties.

Carbon nanotubes (CNTs) are molecular-scale tubes of graphitic carbon and can be considered as the stiffest and strongest fibers known and have remarkable electronic properties and many other unique characteristics. In many applications such as field emission sources, biosensors, electrical interconnects and micromechanical devices, it is necessary to grow CNTs vertically aligned on the substrates. This alignment in the vertical direction can be achieved through these two methods: thermal CVD (TCVD) and plasma enhanced CVD (PECVD). The alignment in TCVD is achieved by crowding effect from neighboring CNTs [1]. For building a waveguide antenna, CNT bundles have been proposed to mitigate the problem of impedance mismatch by adjusting different tube diameter, length and bundle cross-section size. The exact positioning of the nanotubes is also vital for applications such as RF filters and micro switches. Uniform and vertically aligned CNTs of desired sizes can be grown at precisely determined locations by the process of PECVD [2, 3]. The PECVD method has the advantage of being controllable with tube diameter and length less than 5% deviation. For nano electromechanical devices, a good contact to the underlying metal electrode is essential [4]. The optimum condition of catalyst and metal underlayer can be tailored and controlled. According to the growth of vertically aligned carbon nanotubes, state of the art in **Figure 1** shows the CNT arrays on the Si substrate.

2.2. Graphene as 2D materials candidate

Synthesis and scalability of 2D layered materials is one of the most competitive challenges in the material science research area. The first well-known technique of process by mechanical exfoliation discovered by A. Geim for remarkable graphene delivering the best material properties has faced limitations in terms of needs of complementary steps for material encapsulation to guarantee a minimum air and humidity stability. Today, some scalable manufacturing

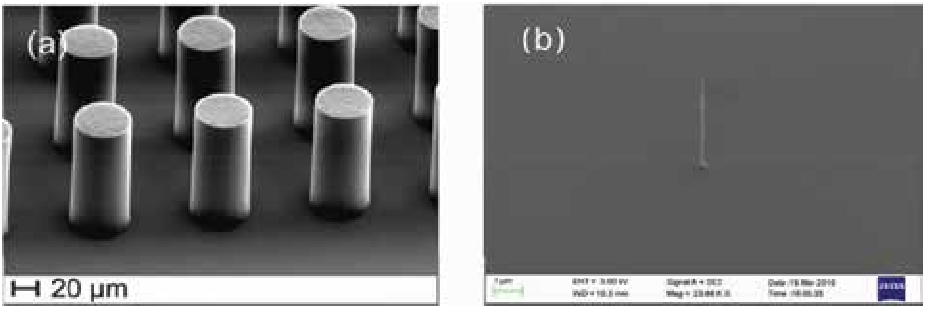

Figure 1. (a) CNT bundles grown by TCVD and (b) single CNTs grown by PECVD.

processes are identified to help in large-scale development of graphene/CNT-based devices and system development.

In the area of solution-based synthesis, solvent-based exfoliation methods have been recently demonstrated for mono and few layer nanosheets fabrications, with efforts brought to solvent toxicity elimination thanks to the use of water [Casigari]. In association, emerging ink-jet printing techniques become promising for large-scale synthesis of 2D materials. Structural imperfections may occur locally compared to other approaches but more adequate for low-end electronics applications, as technological key for large-scale material heterostructures ordering on flexible substrates.

Molecular beam epitaxy (MBE) growth technique, mainly used for bulk semiconducting materials manufacturing still remains one of the most controlled technique for highly precise thickness management with high level of material quality, with availability of in-situ material characterization during process.

In the area of vapor-based synthesis, metalorganic chemical and physical vapor deposition (MOCVD), as well as atomic layer deposition (ALD) approaches are proposed for TMD materials synthesis avoiding any catalyst layer presence for growth in some cases.

2.3. Material integration in electronic devices: scaling electrical contacts

In order to benefit from exceptional electromagnetic properties of nanomaterials in microwave domain, crucial intrinsic impedance considerations may be studied to maximize electrical signal transmission. For this aspect, material Fermi level location knowledge is crucial, and must be subsequently confronted to the working function of selected noble metals to be used as electrodes such as Au, Ti, Ag, Fe and Pd as the most common examples. Depending on the spatial constitution of materials, different approaches can be employed to optimize electrons and holes flows and recombination processes, that is, charged injection electronic devices.

The second aspect to be considered concern the skin depth effect which occurs in any metal and imposes material thickness constraints for electrical ohmic losses minimization, as a function of frequency and material conductivity. In the case of low-dimensional materials, where at least one dimension of material is atomically thin, unprecedent behavior with frequency is expected.

With the decrease of the dimensions of electronic devices, the role played by electrical contacts is ever increasing, eventually coming to dominate the overall device volume and total resistance. This is especially problematic for monolayers of semiconducting transition-metal dichalcogenides (TMDs), which are promising candidates for atomically thin electronics. Ideal electrical contacts to them would require the use of similarly thin electrode materials while maintaining low contact resistances.

As reproduced in **Figure 2**, 2**D** material heterostructure constitution for a complementary matching process or a specific choice of metal may be needed to form an alloy avoiding Van der Walls gap naturally imposed by some 2D materials in contact with noble metals, by orbital overlapping lack [5].

Recently, valley dynamics of excitons in semimetals are taken under considerations for semimetals. Tunnel barrier introduction at electrical contacts assumed by ferromagnetic electrodes has been investigated in order to modulate the contact resistance of graphene and TMDSs with electrodes by spin injection, allowing impedance matching by magnetoresistance signal detection.

Main considerations for charge transfer maximization are focused also on contact transfer length L_T, which defines the length over which injection occurs from the contact edge, defining then the contact resistance R_c as [6, 7].

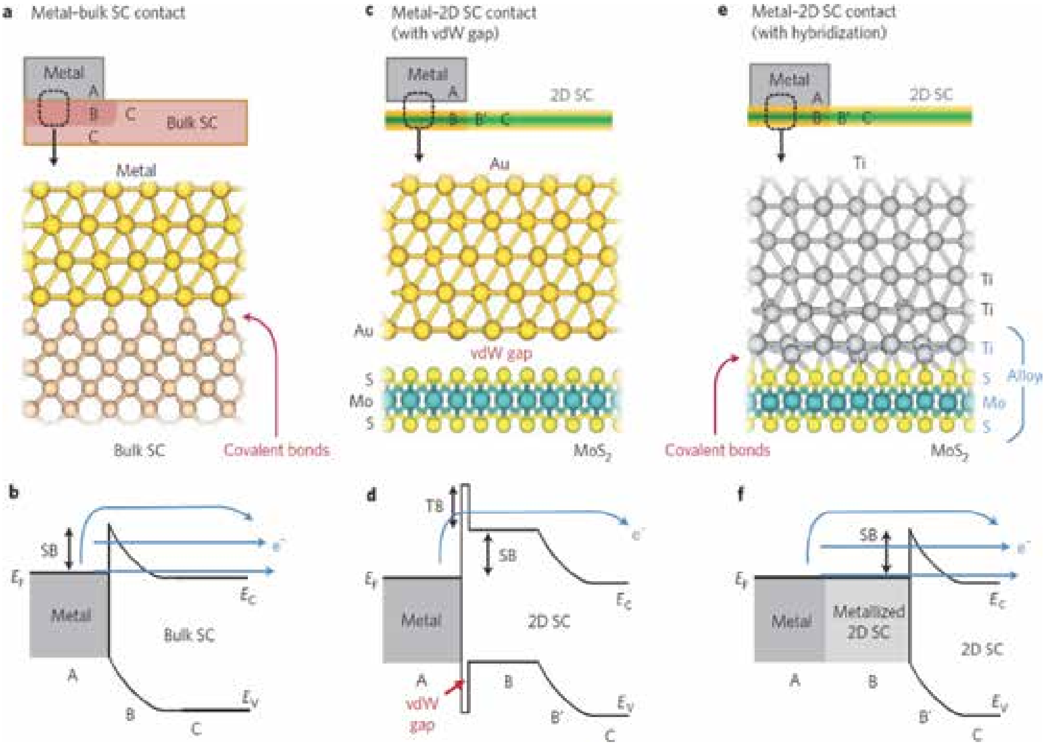

Figure 2. Different types of metal-SC junctions and their respective band diagrams for (a, b) bulk interface, (c, d) metal/2D SC interface lik MoS2/au contact, (e, f) hybridization of metal/2D SC interface [6].

$$\mathrm{R_c} = \sqrt{\rho_\mathrm{c}.\mathrm{R_s}}\,\mathrm{cotanh}\left(\frac{\mathrm{L}}{\mathrm{L_T}}\right)/\mathrm{L_W} \tag{1}$$

With

$$\mathrm{L_T} = \sqrt{\frac{\rho_\mathrm{c}}{\mathrm{R_s}}} \tag{2}$$

where L is the length and Lw is the width of the contact, ρ_c is the nanomaterial resistivity and Rs is the metal-material interface resistivity. It can be seen that the dependence of Rc on L is nonlinear because of current crowding.

2.4. Latest study-case examples

2.4.1. CNT-based transistors

Carbon nanotube (CNT) field effect transistors (FETs) are under investigation as replacements for silicon and III-V high-speed electronics [8]. Semiconducting CNTs are unique electronic materials with room temperature carrier mobility in excess of 100,000 $cm^2/V/s$, three times larger than that of InAs, and a band gap of −0.9 eV, which is close to that of Silicon. Some of the key semiconducting properties of CNTs are compared with other materials in **Table 3** [9]. The high mobility makes CNT FETs attractive for low-power amplifiers and the high-saturated electron velocity leads to projected operation into the THz range [10]. Single-wall nanotubes (SWNTs) are inherently small, ~nm in diameter. This ultra-small diameter enables effectively one-dimensional conduction with the potential for ultra-low shot-noise performance and improved linearity. An additional benefit of small size is extremely low capacitance, which translates into high operating speeds without the need for extreme lithography.

CNT FETs based on SWNTs have been extensively characterized at DC. Much of this attention has been motivated by the near ballistic conduction, high current and transconductance density of CNT transistors [11]. But their high-frequency application faces a challenge of impedance matching due to the inherent mismatch between the resistance quantum (~ 25 kΩ) typical

	Bandgap eV	Electron mobility $cm^2/V/s$	Saturated electron velocity 10^7 cm/s	Thermal conductivity W/cm/K
CNT	0.9	100,000	>10	>30
InAs	0.36	33,000	0.04	0.27
Silicon	1.1	1500	0.3	1.5
GaAs	1.42	8500	0.4	0.5
InP	1.35	5400	0.5	0.7
4H-SiC	3.26	700	2	4.5
GaN	3.49	900	3.3	20

Table 3. Electrical properties of material for FETs.

of nanodevices and the characteristic impedance of RF circuits (50 Ω). There are only a few reports on HF performances measurement of CNT transistors. In terms of cut-off frequency, Purdue University measured f t = 2.5 GHz (intrinsic value) [12], NEC research laboratory measured f_t = 10 GHz (intrinsic value) [13]. The state of the art is the direct measurement of a current gain cut-off frequency of 4 GHz and an intrinsic value of 30 GHz (calculation by removing access and parasitics capacitances) on a transistor composed of a large number of CNTs [14]. Nevertheless, a large part of the deposited CNTs is metallic and this prevents transistor operation at higher microwave frequencies. CNT FET technology can potentially improve in comparison to that of a scaled silicon technology. As a quasi-one-dimensional (1D) conductor, a CNT channel resistance is limited by the fundamental quantum resistance (R Q) of 6.5 kΩ per tube. The simplest idea is to deliver to this quantum resistance (ignoring metallic versus semiconducting behavior) a 1 V operating voltage, which will give a current of about 150 μA/nanotube. With all its non-idealities like poor contacts, scattering as well as existence of tunneling barriers, the state of the art CNT FETs can deliver around 20 μA/nanotube at ~1 V.

Moreover, the capacitance per nanotube is ~2–5 aF, which corresponds to ~1 fF/μm, not far from a silicon transistor. The conclusion is that the 1D CNT array technology can potentially deliver a much higher current in the same area and for identical gate capacitance, which will lead to increased current density and lower delay at higher integration density. It can be also concluded that an arrayed CNT FET using the same interconnect parasitics, as the most advanced 65 nm CNT transistor will feature an 8-times area improvement and 5-times delay reduction [15]. To verify performance at microwave frequencies, Pesetski et al. [16] proposed to develop an alternate measurement technique: instead of observing the output at the input frequency, which was susceptible to crosstalk, they performed a two-tone measurement and observed the intermodulation products. As a result, the CNT FET acts like a mixer, producing an intermodulation product at 10 kHz; and no evidence of a roll-off caused by the CNT FET was observed, even at 23 GHz.

2.4.2. Graphene-based transistors

Transition-metal dichalcogenides have developed important visibility [17] in the recent years due to advances in nanotechnology. Several potential applications [18] are well suited for TMDCs among which they are also interesting for transistor applications. Regarding high-frequency transistors, not a lot of results are published mainly due to lack of large area material, the best results were obtained using a MoS_2-based channel with a thickness of few monolayers. The channel length was 1 μm, whereas the backgate capacitance was 11.5 nF/cm^2. The mobility reported was 170 cm^2/Vs for a drain voltage of 0.5 V and a backgate voltage of 20 V. The MoS_2 thickness is critical for high performance FET transistors. The thickness considered [19] is in the range 2–7 nm. Reducing the dimensions of the channel length to 116 nm, the FETs showed a transconductance of 60 μS/μm at a drain voltage of 5 V and a drain conductance of less than 2 μS/μm, indicating an intrinsic gain of 30 with an on–off ratio higher than 10^7. The cut-off frequency was 42 GHz and the maximum oscillation frequency was 50 GHz. Even though technology is still at its early stages [20], TMDS-based devices already exhibit good metrics, comparable or even higher to those achieved by graphene.

2.4.3. CNT-based interconnects

As previously mentioned, 3D IC technology is one of the main driving forces for the continuous down scaling of the IC device [21, 22]. There are many interconnection technologies such as wire bonding, edge connect and capacitive or inductive coupling method to fabricate 3D-IC devices [23, 24]. However, the most key technology for enabling 3D-IC package is through-silicon via (TSV) technology which acts as paths for signal exchange and power delivery between the stacked chips [25, 26]. TSV technology has allowed great progress in reducing signal delay, enhancing the IC integration and decreasing the overall packaging volume [27]. Thus, the development of this technology is accelerating the miniaturization of 3D-IC devices as well as integration of I/O systems. The key performance of TSVs is determined by the filling materials used in the silicon via. There are various materials that have been used for the TSV, such as tungsten (W), copper (CU) [28, 29] and a Ag/polypyrrole composites [30]. The copper is the most commonly used filling material for TSV due to its excellent electrical conductivity and low process costs. However, the main limiting factor for Cu-TSV technology is the large difference in the coefficient of thermal expansion (CTE) between Cu and Si, which results in mechanical stress in the TSV and the surrounding Si [31]. In addition, the electro-migration and skin effects also limit the application of Cu TSV in high-frequency applications [32]. However, it is currently not technologically possible to use Cu for high aspect ratio via structures [33].

A series of modeling work on CNT interconnects has been done by Naeemi and Meindl [34]. The modeling of the capacitance and inductance components of CNT interconnects can be found in [35]. A high-frequency analysis of CNT interconnects has also been performed [36], in which one interesting conclusion is that the skin effect of CNT interconnects is significantly less severe than that of metal lines. Based on the model described in the reference listed above, the resistances of CNT off-chip interconnects, such as through-silicon-vias (TSVs), can be estimated by straightforward calculations assuming some typical dimensions. An MWNT with 30 nm outer diameter and 15 nm inner diameter, 100 μm length and 1 μm electron mean free path, at room temperature has a conductance of 0.048 $k\Omega^{-1}$. This leads to an estimated resistance of 21 kΩ for such an MWNT if all its walls can be contacted. Note that here the electron mean free path is taken as 1 μm based on experimental observations. Therefore, if a loosely packed CNT forest can be densified into closely packed bundle, the conductivity of such a structure can be greatly increased [37].

3. Exceptional electromagnetic material properties for microwave applications

Effective theoretical frequency-dependent material conductivity of carbon-based nanomaterials: from individual to collective (bundle) configuration.

Frequency-dependent graphene conductivity can be approximated using Kubo formula.

$$\begin{aligned}\sigma_s(\omega) &= \mathrm{i}\frac{1}{\pi\hbar^2}\frac{e^2 k_B T}{\omega+\mathrm{i}2\Gamma}\left\{\frac{\mu_c}{k_B T}+2\ln\left[\exp\left(-\frac{\mu_c}{k_B T}\right)+1\right]\right\} \\ &+\mathrm{i}\frac{e^2}{4\pi\hbar}\ln\left[\frac{2|\mu_c|-\hbar(\omega+\mathrm{i}2\Gamma)}{2|\mu_c|+\hbar(\omega+\mathrm{i}2\Gamma)}\right]\end{aligned} \tag{3}$$

with the chemical potential μ_c and the relaxation rate Γ. This complex expression in which Γ has been experimentally calculated to 0.1 meV, demonstrates a complex behavior with σ_{real} and σ_{imag} as real and imaginary parts of $\sigma_s(\omega)$ depending on value μ_c. From a dyadic Green's function formulation of electromagnetic fields propagation through Sommerfeld integrals, TE or TM mode surface wave propagation operation has been validated whether positive or negative value of σ_{imag} [38].

3.1. SW/MWCNT conductivity

Individual SW CNT consist in a spatial unique angled-rolling of a graphene sheet depending on the associated chiral vector which defines their metallicity degree.

Starting from graphene conductivity formulation above, armchair and zigzag enrollment configuration leading to a metallic behavior implies also a complex conductivity definition in which imaginary part existence can be detected (see **Figure 3**).

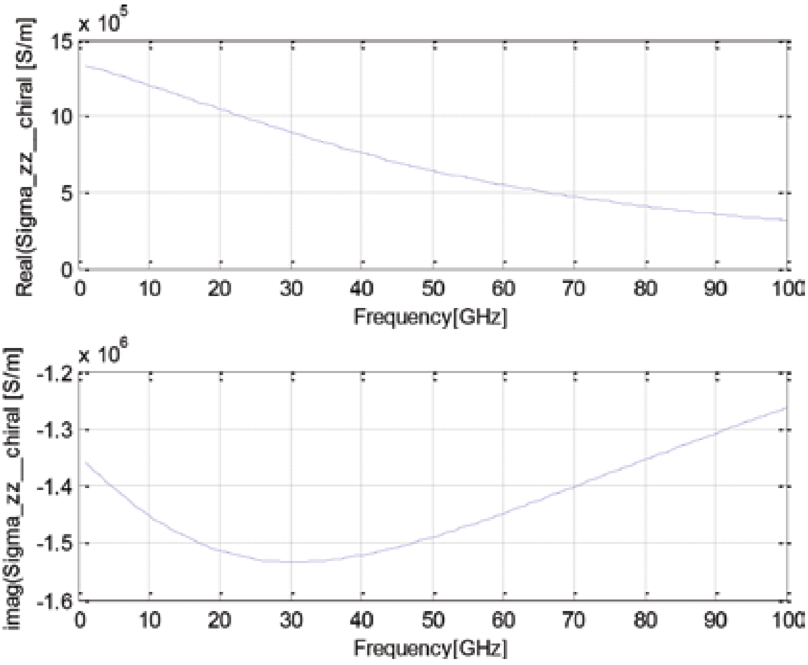

Figure 3. Dynamic conductivity as a function of frequency of a metallic chiral CNT.

$$\sigma_{zz_{\mathrm{chiral}}} = -j\frac{8\pi e^2 \gamma_0 \sqrt{3}}{h^2\sqrt{m^2 + n^2(\omega - j\nu) + mn}} \text{ with } 2m + n = 3N \tag{4}$$

(m and n equal to 1)

As a consequence, for SW CNT, an equivalence must be inserted between the surface conductivity of a cylinder and the conductivity of a material with a dependency on 1/r, where r is the radius of the CNT cylinder, for the definition of the material impedance, which still remains a complex expression.

For MW CNT, the conductivity appears as a sum of individual density current of each wall.

3.2. State of the art microwave material modeling techniques

3.2.1. 1D materials: individual SW and MW CNT

In 2007, first modeling tools of these 1D nanomaterials were developed for optical scattering predictions of metallic SWCNTs array by Hao and Hanson [39] by using periodic Green's function applied to an array of finite-length conducting elements with quantum conductance given previously. At the same time, Maksimenko [40] defined a competitive electromagnetic approach based on Leontovich-Levin Integral Eqs. (IE) method. First surface impedance model of CNT appeared in 2008 from Fichtner by using Hallens'type IE with a modified Kernel function in equations. Electromagnetic modeling work for infinite objects was pursed by Berres and Hanson in 2011 in the microwave and IR frequency regime using a semi-classical approach [41]. For bindle-type configuration of arrays of MWCNT, resulting global conductivity calculation was adopted by Choï and Saranbandi. In this last case, Method of Moments (MoM) and the Mixed Potential Integral Equation (MPIE) were implemented to predict CNT-based strip antennas and thin gold films [42].

3.3. State of the art microwave material characterization techniques

EM material parameters identification at RF/microwave frequencies is a milestone to understand and design new RF components for future implementation in next generation of microwave systems. Principles and techniques of material parameters characterization in microwave domain using transmission lines have been widely studied for determination of bulk material permittivity, permeability and conductivity in frequency domain. Non-destructive method by electromagnetic coupling of unknown material thin layer with a quasi-TEM propagation mode in planar configuration (microstrip or coplanar line) becomes the most appropriate methodology today to achieve a complete and broadband characterization.

3.3.1. Coaxial environment

For nanomaterials characterization, coaxial lines techniques have been mainly used because of direct commercial provision access of 2D/1D materials in disperse solutions. These techniques imply frequency bandwidth limitations because of waveguides dimensions and random material orientation in relation to e-field polarization direction.

3.3.2. Probe-test environment

Device downscaling motivation has progressively opened the route for the development of electromagnetic properties identification at dimensions which must be consistent with operating frequency.

Some research groups involved in ultra-thin layers deposition on reference substrates have reused former modeling tools dedicated to homogenous material frequency-dependent permittivity identification by conformal mapping technique. In this approach, where a parallel-type capacitance equivalence of any material layer is assumed from permittivity elliptic integrals equations applied to a coplanar line configuration (K and K′), direct extraction of real permittivity of an unknown material layer is reachable if stacked uniformly (i.e., complete layer under/overlying) in plane from signal line to ground planes in a well-known multilayer coplanar structure. Complementary de-embedding structures need to be fabricated in order to eliminate probe-test parasitic on measurement results.

This technique is based on microwave S-parameters measurements of dedicated test beds structures designed in microstrip and coplanar technology. After analytic S-to-ABCD-matrix conversion for the exact determination of effective propagation constant and permittivity of the transverse multilayered structure, frequency relative permittivity of 2D/1D material is obtained as an inverse problem by using a conformal mapping technique from the Veyres-Fouad Hanna approximation assuming multiple layers as a superposition of capacitances. This specific characterization technique in frequency allows experimental detection of anisotropic behavior of nanomaterials thanks to electromagnetic fields orientation access and opens routes to the use of nanotechnology for the definition of new multiscale microwave devices design.

A complementary modeling tool based on a circuit-type approach could have been added to this procedure where equivalent lineic R, L, C values of the studied material are estimated from circuit simulations in commercial softwares. This approach has been performed to graphene flakes, as in Ref. [43].

3.3.3. Free space environment

For antennas and radars systems, an equivalent approach in free space has been implemented by assuming a bi-static experimental configuration for multilayered samples, using a contactless technique avoiding anechoidal environment. This technique is based on reflection coefficient measurement of bulk materials, which imposes self-consistent calibration structures. Thanks to horn antennas electromagnetic excitation, material impedance in both TM and TE modes can be extracted allowing the identification of material permittivity and conductivity with anisotropic behavior checking. Limitation on material thickness reduction is not identified yet because of characterization configuration in reflective manner and dimension to wavelength, and allows broadband materials parameters identification.

A complementary approach is now under study in order to extend bi-static measurements to low-dimensional materials. Technical challenges target characterization technique limitations as compared to material thickness. This approach is assisted by electromagnetic simulations which help in the definition of de-embedding structures, as well as planarity material requirement and material surface constraints. In this way, a 40–67 GHz frequency band has been selected to overcome these boundary conditions allowing access to centimeter-squared surface scale characterization of materials with atomic thickness.

3.4. Material impedance equivalence: toward "Mattertronics"

In order to solve multiscale problem, characterization techniques customization to low-dimensional materials becomes crucial for any device design work by full-wave analysis in which implemented material constitutive parameters from classical electromagnetic material Drude/Lorentz representation and Kramers/Kronig relationships [44] are used for material R, L,C circuit equivalence. Material complex permittivity (ε), conductivity (σ) and permeability (μ) knowledge helps in the definition of material impedance Z equivalence.

4. Application to microwave antenna design: toward subwavelength radiation

4.1. Fundamental antenna parameters requirements: from theory to technology qualification

The simplest representation of a radiating element consists in a LC resonant cell. Wire antennas are the oldest and most versatile antennas suited for various applications. It is a simple device to understand most of the radiation mechanism and the dipole structure simplification of radiating elements. The typical configuration is made up of two conductor wires, with a length of $\lambda/2$.

The current distribution in the conductor wires can be considered in one dimension due to the geometry (usually the z-axis direction). The time variation of the current distribution will generate a radiated electromagnetic field in the surrounding space. Maxwell's equations lead to the relation between the current variation I(z) and the radiated field E_θ in the far field space. Along with the radiation pattern is a set of other key parameters that are used to quantify an antenna and its performances:

- input impedance is the impedance the power input circuit will have to match in order to transmit the maximum power to the radiating device.
- gain is the ratio of intensity, in a given direction, to the radiation intensity that would be obtained if the power accepted by the antenna was radiated isotropically. The radiation intensity corresponding to the isotropic radiated power is equal to the input power accepted by the antenna divided by 4π.
- directivity is the ratio of the radiation intensity in a given direction from the antenna to the radiation intensity average over all directions.
- The radiation efficiency which is the ratio of the radiated power over the accepted power and is a dimensionless combined factor of both the conduction efficiency (losses through

metal conduction) and dielectric efficiency (losses through propagation in dielectric space) considered in one dimension, due to the geometry (usually the z-axis direction). This is the time variation of the current distribution that will generate a radiated electromagnetic field in the surrounding space. Maxwell's equations lead to the relation between the current variation I(z) and the radiated field E_θ in the far field space.

From material point of view, targeting radiation performances, similar parameters must be strongly considered such as:

- Lineic inductance/capacitance in order to define the efficient dimension of a LC resonant cell
- Dynamic permittivity which allows the definition of plasma resonance frequency
- Band diagram and work function definition in a metallic atomic configuration to identify efficient contact type with microwave electrode access to match input impedance.

4.2. MWCNT bundle-based microwave antenna design case: from theory to experiment demonstration

As main technological challenge relies on experimental material impedance identification in microwave domain, first studies have led to the choice of a differential-type approach. In order to overcome physical constraints imposed by material dimensions access, following technological process, preliminary planar resonant structures in CPW technology have been achieved with suitable taper-based electrodes (**Figure 4**), for which a resonant frequency shift assumed by VA-MWCNT bundle is expected. For microwave signal coupling methodology, different ended geometries have been tested in order to validate the material properties from different devices.

From this approach, the equivalent impedance of VA-MWCNT bundles connected in series to the microwave test bed structure is obtained by direct input impedance subtraction de-embedding techniques.

Preliminary research works have been done on sub-wavelength MWCNT-based antennas design benefiting from natural LC behavior or complex conductivity never achieved in classical conductors in microwave domain. By exploiting also a vertically aligned CNT bundle configuration reducing drastically the contact resistance of individual MWCNT [39], first demonstration of resonance frequency shift of coplanar antennas incorporating a 500 μm-length MW CNT circular bundle have been experimentally revealed at a microwave frequency around 60 GHz (**Figure 4**). In parallel, electromagnetic material properties identification by experimental material complex impedance extraction under TE or TM mode excitation is under progress.

A broadband microwave characterization is performed using a CASCADE MICROTECH probe-test equipment allowing S-parameters measurements with a vectorial network analyzer in the 0.2–67 GHz frequency bandwidth, calibrated by the SOLT method.

From reflection coefficient measurements, input impedance of resonant structure has been extracted. The validity of the measurements requires to apply this methodology away from the resonant frequency band, in order to avoid undefined behavior.

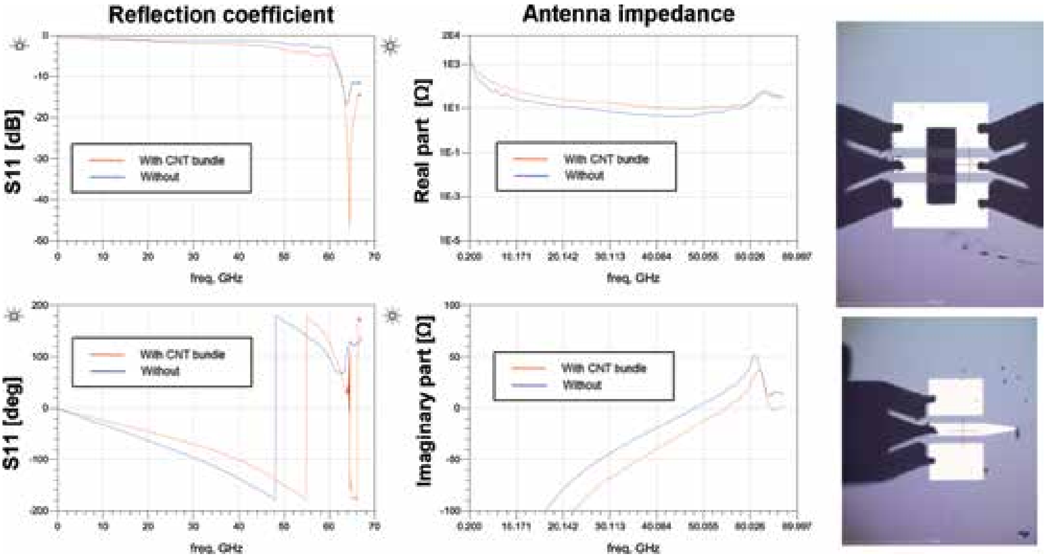

Figure 4. Microwave performances of a MWCNT-based nano antenna in coplanar technology: (a) reflection coefficient in magnitude and phase of device with (red) and without (blue) MW CNT bundle, (b) antenna impedance in real and imaginary part with (red) and without (blue) MW CNT bundle, (c) optical image of MWCNT-based test bed structure–(d) optical image of the MW CNT-based nano antenna.

By adopting a specific de-embedding technique procedure, frequency-dependent CNT bundle impedance extraction in TE and TM mode excitation confirms accessible additional design matching solutions at a frequency of 10 GHz.

Today, by benefitting of technological processes achievement access, 3D electromagnetic modeling parametrization of MW CNT bundles with technology will add complementary degree of freedom in MW CNT-based sub-lambda antenna and array design. On-chip emitting/receiving modules design validation by on-wafer sub-lambda S-parameters measurements (DC-110 GHz) [45] will be assisted by preliminary equivalent electromagnetic material properties experimental validation (ε, μ and σ) fulfilling anisotropic behavior of individual vertically aligned MW CNTs grown in bundle with length-to-diameter aspect ratio dependency comparable to theoretical predictions made for metallic nanowire-based antenna [46], governing MW CNT-based individual sub-lambda antenna design.

5. Conclusions and prospects

This chapter addresses the emerging research area dealing with technological breakthroughs benefitting from quantum effects exaltation by the use of nanomaterials/nanotechnologies in the definition and description of next future electromagnetic (EM) nanosystems.

It is shown that emerging nanotechnologies dedicated to exceptional electromagnetic properties of 1D and 2D materials processing offer today the possibility of design innovations in broadband reconfigurable EM systems with high degree of confinement of electromagnetic waves and extreme miniaturization.

In the field of electromagnetism, the near future will be governed by the merging of three apparently independent domains:

- The first one is dealing with the generation, control and processing of surface waves
- The second one is associated to the merging area of antennas based on nano-radiating elements and nanoantennas
- The third one is covering the ever growing field of new materials, especially one- and two-dimensional materials, nanostructured materials and the associated topological effects

The symbiosis of these three areas will give birth to revolutionary concepts such as nanoarchitectronics (the science and technology for building extreme multiscale systems covering from nanometer to mesoscopic scales) and artificial nano-engineered interfaces.

Acknowledgements

The authors would like to acknowledge the SHT company for providing MW CNT bundles.

Author details

Charlotte Tripon-Canseliet[1]* and Jean Chazelas[2]

*Address all correspondence to: charlotte.tripon-canseliet@espci.fr

1 LPEM, ESPCI Paris, PSL Research University, CNRS, Sorbonne Université, Paris, France

2 THALES DMS, Elancourt, France

References

[1] Esconjauregui S, Fouquet M, Bayer BC, Ducati C, Smajda R, et al. Growth of Ultrahigh Density Vertically Aligned Carbon Nanotube Forests for Interconnects. ACS Nano. 2010;**4**: 7431-7436

[2] Teo KBK, Chhowalla M, Amaratunga GAJ, Milne WI, Hasko DG, Pirio G, Legagneux P, Wyczisk F, Pribat D. Uniform patterned growth of carbon nanotubes without surface carbon. Applied Physics Letters. 2001;**79**:1534-1536

[3] Chhowalla M, Teo KBK, Ducati C, Rupesinghe NL, Amaratunga GAJ, Ferrari AC, Roy D, Robertson J, Milne WI. Growth process conditions of vertically aligned carbon nanotubes using plasma enhanced chemical vapor deposition. Journal of Applied Physics. 2001;**90**: 5308-5317

[4] Lee SW, Lee DS, Morjan RE, Jhang SH, Sveningsson M, Nerushev OA, Park YW, Campbell. A Three-Terminal Carbon Nanorelay. Nano Letters. 2004;**4**:2027-2030

[5] Kang J et al. Computational study of metal contact to monolayer TMD semiconductors. Physical Review X. 2014;**4**:031005

[6] Leonard F. Electrical contacts to one and two-dimensional nanomaterials. Nature Nanotechnology. 2011;**6**:773-783

[7] Allain A et al. Electrical contacts to two-dimensional semiconductors. Nature Materials. 2015;**14**:1195-1205

[8] McEuen PL, Fuhrer MS, Park H. Single-walled carbon nanotube electronics. IEEE Transactions on Nanotechnology. Mar. 2002;**1**(1):78-85

[9] Zolper JC. Status, challenges, and future opportunities for compound semiconductor electronics. In: 25th Annual Gallium Arsenide Integrated Circuits Symposium. pp. 3-6; 2003

[10] Burke PJ. AC performance of nanoelectronics: Towards a THz nanotube transistor. Solid State Electronics. 2004;**40**:1981

[11] Xing CJ et al. Investigation on self-heating effect in carbon nanotubes field-effect transistors. IEEE Transaction on Electron Devices. 2010;**58**:523

[12] Kim S. et al. A poly-Si gate carbon nanotube field effect transistor for high frequency applications. IEEE Intern. Microwave Symposium. 2005:303-306

[13] Narita et al. RF performances of multiple channel carbon nanotube transistors, Trends in Nanotechnology Conference, Grenoble. 2006

[14] Le Louarn A et al. Intrinsic current gain cutoff frequency of 30 GHz with CN transistors. Applied Physics Letters. 2007;**90**:233108

[15] Keshavarzi A et al. Carbon Nanotube Field-Effect Transistors for High- Performance Digital Circuits—Transient Analysis, Parasitics, and Scalability. IEEE Transactions on Electron Devices. 2006;**53**(11):2718-2726

[16] Pesetski A et al. Carbon nanotube field-effect transistor operation at microwave frequencies. Applied Physics Letters. 2006;**88**:113103

[17] Wang QH, Kalantar-Zadeh K, Kis A, Coleman JN, Strano MS. Electronics and optoelectronics of two-dimensional transition metal dichalcogenides. Nature Nanotechnology. 2012;**7**:699-712

[18] Jariwala D, Sangwan VK, Lauhon LJ, Marks TJ, Hersam MC. Emerging device applications for semiconducting two-dimensional transition metal dichalcogenides. ACS Nano. 2014;**8**:1102-1120

[19] Cheng R, Jiang S, Chen Y, Liu Y, Weiss N, Cheng H-C, Wu H, Huang Y, Duan X. Few-layer molybdenum disulfide transistors and circuits for high-flexible electronics. Nature Communications. 2014;**5**:5143

[20] Tong X, Ashalley E, Lin F, Li H, Wang ZM. Advances in MoS2-based field effect transistors (FETs). Nano-Micro Letters. 2015;**7**:203-218

[21] Lau JH. Overview and outlook of through-silicon via (TSV) and 3D integrations. Micro-Electronics International. May 2011;**28**(2):8-22

[22] Ramm P et al. 3D integration technology: Status and application development. In: 2010 Proceedings of the ESSCIRC; 2010. pp. 9-16

[23] Carson FP, Kim YC, Yoon IS. 3-D stacked package technology and trends. Proceedings of the IEEE. Jan. 2009;**97**(1):31-42

[24] Motoyoshi M. Through-silicon via (TSV). Proceedings of the IEEE. Jan. 2009;**97**(1):43-48

[25] Dong M, Santagata F, Sokolovskij R, Wei J, Yuan C, Zhang G. 3D system-in-package design using stacked silicon submount technology. MicroElectronics International. Apr. 2015;**32**(2):63-72

[26] Santagata F et al. Fully back-end TSV process by cu electro-less plating for 3D smart sensor systems. Journal of Micromechanics and Microengineering. May 2013;**23**(5):55014

[27] Lu JJ-Q, Cale TS, Gutmann RJ. Rensselaer 3D integration processes. In: Garrou P, Bower C, Ramm P, editors. Handbook of 3D Integration. Wiley-VCH, Weinheim. Vol. 11. 2008. pp. 447-462

[28] Kikuchi H et al. Tungsten through-silicon via technology for three-dimensional LSIs. Japanese Journal of Applied Physics. Apr. 2008;**47**(4S):2801

[29] Wolf MJ et al. High aspect ratio TSV copper filling with different seed layers. In: Electronic Components and Technology Conference, 2008. ECTC. 58th ed; 2008. pp. 563-570

[30] Horváth B, Kawakita J, Chikyow T. Through silicon via filling methods with metal/polymer composite for three-dimensional LSI. Japanese Journal of Applied Physics. Jun. 2014; **53**:6S

[31] Selvanayagam CS, Lau JH, Zhang X, Seah SKW, Vaidyanathan K, Chai TC. Nonlinear thermal stress/strain analyses of copper filled TSV (through silicon via) and their flip-chip microbumps. IEEE Transactions on Advanced Packaging. Nov. 2009;**32**(4):720-728

[32] Gupta T. Copper Interconnect Technology. New York, NY : Springer Science+Business Media, LLC. 2009

[33] Gu C, Xu H, Zhang T-Y. Fabrication of high aspect ratio through-wafer copper interconnects by reverse pulse electroplating. Journal of Micromechanics and Microengineering. Jun. 2009;**19**(6):65011

[34] Naeemi A, Meindl JD. Performance modeling for single- and multiwall carbon nanotubes as signal and power interconnects in Gigascale systems. IEEE Transactions on Electron Devices. Oct. 2008;**55**(10):2574-2582

[35] Naeemi A, Meindl JD. Physical modeling of temperature coefficient of resistance for single- and multi-wall carbon nanotube interconnects. IEEE Electron Device Letters. Feb. 2007;**28**(2):135-138

[36] Li H, Banerjee K. High-frequency analysis of carbon nanotube interconnects and implications for on-chip inductor design. IEEE Transactions on Electron Devices. Oct. 2009;**56**(10): 2202-2214

[37] Kajiura H, Nandyala A, Bezryadin A. Quasi-ballistic electron transport in as-produced and annealed multiwall carbon nanotubes. Carbon. May 2005;**43**(6):1317-1319

[38] Hanson GW. Dyadic Green's functions and guided surface waves for a surface conductivity model of graphene. Journal of Applied Physics. 2008;**103**:064302. DOI: 10.1063/1.2891452

[39] Hao J, Hanson G. Optical scattering from a planar array of finite-length metallic carbon nanotubes. Physical Review B. Apr. 2007;**75**(165416):1-7

[40] Maksimenko S, Slepyan G, Nemilentsau A, Shuba M. Carbon nanotube antenna: Far-field, near-field and thermal-noise properties. Physica E. 2008;**40**:2360-2364

[41] Berres J, Hanson G. Multiwall carbon nanotubes at RF-THz frequencies: Scattering, shielding, effective conductivity, and power dissipation. IEEE Transactions on Antennas and Propagation. Aug. 2011;**59**(8):3098-3103

[42] Choi S, Sarabandi K. Performance assessment of bundled carbon nanotube for antenna applications at terahertz frequencies and higher. IEEE Transactions on Antennas and Propagation. Mar. 2011;**59**(3):802-809

[43] Vincenzi et al. Open-thru de-embedding for graphene RF devices. IEEE IMS 2014. Jun. 2014. DOI: 10.1109/MWSYM.2014.6848457

[44] Quéré Y. Physique des matériaux. Collection Ellipses. ISBN: 2729888586

[45] Tripon-Canseliet C, Xavier S, Modreanu M, Ziaei A, Chazelas J. Vertically-grown MW CNT bundles microwave characterization for antenna applications. In: IEEE Conference on Numerical Electromagnetic Modeling and Optimization for RF, Microwave and Terahertz Applications (NEMO), Pavia, Italie; 2014

[46] Tripon-Canseliet C, Xavier S, Deligeorgis G, Coccetti F, Ziaei A, Modreanu M, Chazelas J. Electromagnetic modelling of MW CNT bundles from microwave characterization: Application to small microwave antenna design in integrated technology. In: IEEE European Microwave Conference, Special Workshop on Advances in the "Carbon Based Smart System for Wireless Application", Rome, Italy; 2014

Chapter 4

Computer-Aided Design of Microwave-Photonics-Based RF Circuits and Systems

Mikhail E. Belkin, Vladislav Golovin, Yuri Tyschuk,
Mikhail G. Vasil'ev and Alexander S. Sigov

Additional information is available at the end of the chapter

http://dx.doi.org/10.5772/intechopen.78945

Abstract

In the process of design, a developer of new microwave-photonics-based RF apparatuses is facing a problem of choosing appropriate software. As of today, the existing optical and optoelectronic CAD tools (OE-CAD) are not developed like CAD tools intended for modeling of RF circuits (E-CAD). On the contrary, operating at symbolic level, modern high-power microwave E-CAD tools simply and with high precision solve this problem, but there are no models of active photonic components in their libraries. To overcome this problem, we proposed and validated experimentally a new approach to model a broad class of promising analog microwave radio-electronics systems based on microwave photonics technology. This chapter reviews our known, updated, new models and simulation results using microwave-electronics off-the-shelf computer tool NI AWRDE to pursue advanced performances corresponding to the last generation of key photonics structural elements and important RF devices on their basis.

Keywords: computer-aided design, microwave photonics, photonic components,
RF circuits and system

1. Introduction

Microwave photonics (MWP) is a relatively fresh scientific and technological direction arising among radio-electronic R&D society at the last quarter of twentieth century in the result of combining the achievements of microwave-electronics and photonics techniques [1]. Initially, MWP was an area of interest for a military platform [2, 3] such as radar and electronic warfare means; but, nowadays, it is becoming an object of study and development for emerging areas of telecom industry [4] such as 5G-class wireless networks. For today, MWP technology might be considered as a perspective direction of modern radio-electronics for signals generation, transmission, and processing in various radio-frequency (RF) circuits and systems. Implementation of this concept will enhance the key technical and economical features and such important characteristics as electromagnetic and environmental compatibilities, immunity to external interferences.

Figure 1 demonstrates a typical MWP circuit that is started with RF-to-optical converter (RF/O) and concluded with optical-to-RF converter (O/RF). Between these interfaces, there are a host of efficient photonics processing units in optical domain.

In the process of design, a developer of new MWP-based RF apparatuses is facing a problem of choosing an appropriate software. As of today, the existing optical and optoelectronic CAD tools (OE-CAD) are not developed like being perfected for three decades CAD tools intended for modeling of RF circuits (E-CAD). On the contrary, operating at symbolic level modern high-power microwave E-CAD tool solves this problem enough simply and with high precision, but there are no models of specific active and passive photonic components in its library. To overcome this problem, we have been proposed and validated experimentally a new approach to model a broad class of promising analog microwave radio-electronics systems based on the microwave photonics technology. In particular, the classification of active photonic components and the comparison with a modern OE-CAD tool were described in Ref. [5] and later in more detail version in Ref. [6]. Based on them, the electrical equivalent circuit models for the different types of semiconductor laser [7, 8], photodetector [9, 10], and optical modulator of Mach-Zehnder interferometer configuration [6] were published. Using these components, a number of RF circuit models and successful simulation results for microwave-band optoelectronic oscillator [11], mixer [12], and phased array antenna beam-former network [13] were proposed.

The general concept behind the design is the following. A developer of these novel RF circuits has no basic knowledge about the physical features of active and passive photonic devices, but one has a toolset to measure carefully their transmission characteristics in linear and nonlinear modes. Based on it, the design principles of the equivalent-circuit models to be considered below fully reflect the common building principle of the available E-CAD tools including closed-form or table-specified library models of current and voltage sources, nonlinear active devices, as well as passive elements that subject to frequency band are built on a linear circuitry with lumped (for RF band) or distributed (for microwave and millimeter-wave bands) parameters.

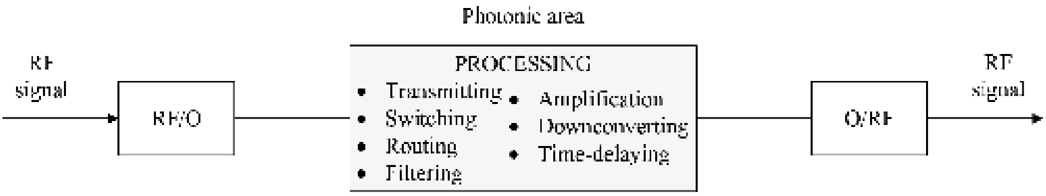

Figure 1. A typical arrangement of MWP circuit.

This chapter reviews our updated and new equivalent-circuit-based models and simulation results using microwave-electronics off-the-shelf computer tool NI AWRDE to pursue advanced performances corresponding to the last generation of key MWP photonics structural elements and important devices on their basis. In particular, Section 2 describes two laser models referred to direct RF-to-optical conversion. In addition, Section 3 presents three optical modulator models for the case of external RF-to-optical conversion. There is a description of two models for optical-to-RF conversion realized by the equivalent-circuit models of photodetector component in Section 4. The component part concludes the discussion of the specific models for optical passives in Section 5. Following the result of the previous sections, some advanced MWP-based RF circuits are modeled in Section 6. Finally, Section 7 concludes the chapter.

2. Direct RF-to-optical conversion

As well known, in a digital fiber-optic communication link, injection-current driven semiconductor laser is a requisite for simple direct conversion to optical band with the speeds up to 10 Gbit/s. In this case, a laser operates in bi-stable mode with two transmitting positions: optical emission is switched off when the injection current is below the threshold of the laser light-current plot (LCP) or is switched on when it is beyond the threshold of the LCP. The main distinguish feature of MWP link, which is a medium for analog RF-signal transmission, is in continuous mode operation presetting DC bias in the middle of LCP's linear area that provides a different approach to design. Below, we demonstrate two laser models usable for various microwave photonic circuits.

2.1. Single-carrier laser model

Figure 2 depicts updated nonlinear model of a semiconductor laser emitter in the form of an electric equivalent circuit, suitable for developers of RF-subcarriers modulated analog fiber-optics systems, devices of microwave optoelectronics, as well as optical interconnects in the

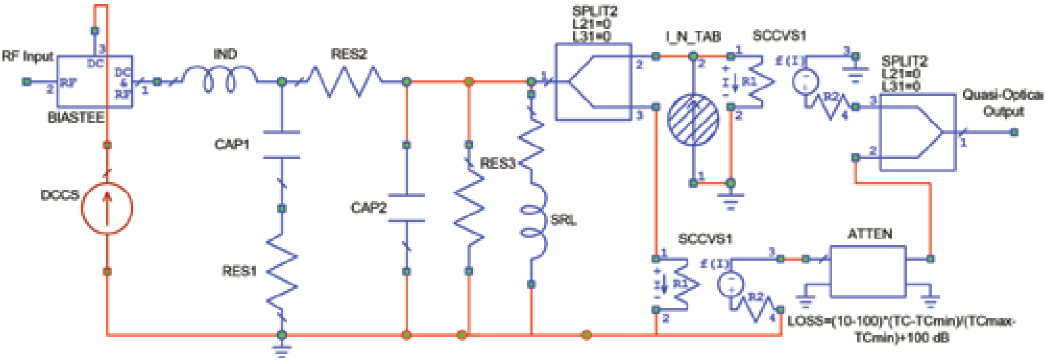

Figure 2. Single-carrier model of a semiconductor laser in the form of an equivalent circuit.

integrated circuits. In this circuit model, each element has a clear physical interpretation. Namely, the active circuitry in according to the previous versions [7, 8] includes library models of DC current source DCCS to adjust operation point, polynomial-approximated SPICE current-controlled voltage source SCCVS1 imitating laser's LCP, and the noise source I_N_TAB allowing to take into account the noise properties of the laser, which are usually expressed in the form of relative intensity noise (RIN) or relative phase noise. Data for the source are specified in tabular form from the results of measurements. Besides, RF input through ideal model of bias-T element (BIASTEE) connects to inductor model (IND) emulating a wire from RF-connector to laser chip. The laser chip itself is represented by elements CAP1 and RES1 simulating the pad capacitance and loss, series resistance RES2, junction capacitance and resistance, and CAP2 and RES3, respectively, and element SRL represents the laser mirror losses and photon storage effects. Notice that the values of all abovementioned passive elements simulate frequency response of RF-to-optical conversion. As a new function, the dependence of the output power on the ambient temperature is added, which makes the model under simulation more suitable for real systems. The temperature drift of the LCP in the circuit is realized on the basis of two models of ideal splitters SPLIT2, the lower unit of SCCVS1, which output is in antiphase relative to the main channel, and the model of attenuator ATTEN, the value of which is a function of a temperature.

Using the proposed model together with a reference photodetector, a set of typical for radio-engineering circuit simulation experiments is able to fulfill including signal transmitting characteristics (S_{21} and S_{11}), noise figure, nonlinearity due to harmonic or intermodulation distortions, and so on. **Figure 3** exemplifies the simulation results of small-signal frequency response (a) and LCPs in the temperature range of 20–70°C (b).

2.2. Multi-carrier laser model

As noted, the great advantage of photonic technology in comparison with the radio-electronic counterpart is the ultra-wide bandwidth of optical fiber, exceeding 10 THz. Following it, in modern MWP circuits, the so-called method of wavelength division multiplexing (WDM) is

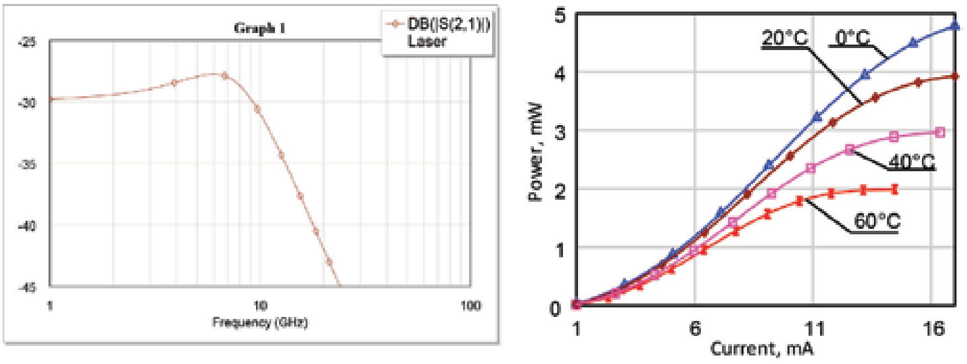

(a) (b)

Figure 3. The examples of simulation experiments: (a) small-signal frequency response, and (b) light-current plot.

widely used [14], in which simultaneous transmission of information on a plurality of optical carriers is provided. The lack in aptitude does not allow the previous model to design correctly multi-carrier MWP circuits and has led to a new generation of laser model feasible for WDM circuit simulation [5, 6]. **Figure 4** depicts the updated nonlinear model of a semiconductor laser emitter suitable for MWP WDM circuits and systems. The model has the simplest configuration including only one quasi-optical (QO) unmodulated carrier and one RF signal but its building principle allows aggregating both optical and RF channels.

In contrast to the model of **Figure 2**, this model has two main input ports titled as "Quasi-Optical Input 1" and "RF Input"; the first one receives waveforms of optical band and the second one is for waveforms of RF-band. Such an approach is correct for a software tool working at the symbolic level. The chain of RF channel consists of sub-circuit network (SUBCKT) including the schematic of **Figure 2** and the model of 9-order Butterworth bandpass filter (BPFB1), which is designed to eliminate spurious output signals of the subcircuit. In line with the standard radio engineering approach, both signals are then mixed using an ideal full-wave diode multiplier. Another model of the BPFB2 with modulated QO signal at the Quasi-Optical Output is terminated by the circuit. In the model, the dependence of the QO carrier frequency versus temperature is additionally introduced, which is realized by means of an additional Quasi-Optical Input 2. The main (foptic-1000 GHz, port 1) and the additional

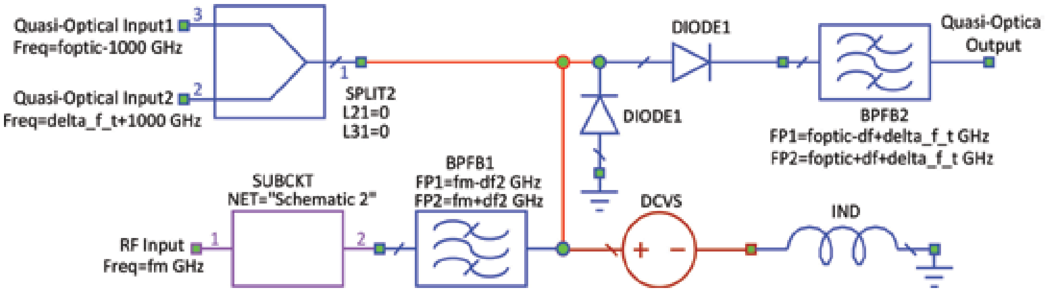

Figure 4. Double-carrier laser model.

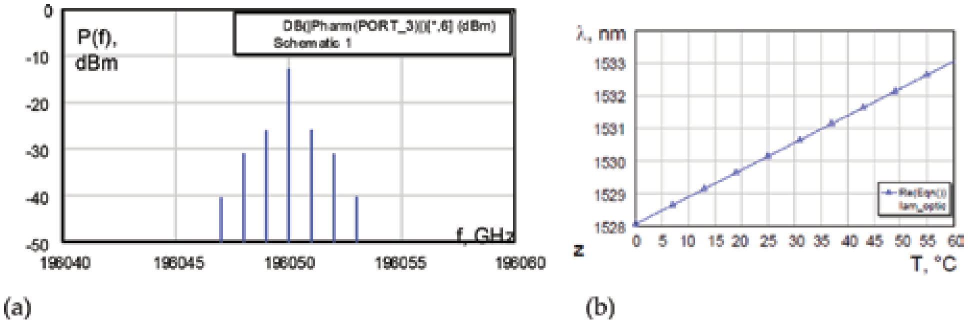

Figure 5. The examples of simulation experiments.

(delta_f_t + 1000 GHz, port 2) signals are fed to the diode multiplier. The value of the auxiliary frequency depends on the factor delta_f_t, which describes the experimental emitted wavelength-temperature dependence of the laser chip. The frequency band of the FPFB2 is also corrected taking into account this factor. **Figure 5** exemplifies the simulation results of output laser spectrum modulated by RF tone of 1 GHz and power 10 dBm (a) and wavelength versus temperature dependence in the range of 0–60°C (b).

3. External RF-to-optical conversion

In spite of cost-efficiency, the direct RF-to-optical conversion has a number of limiting factors including bandwidth, dynamic range, chirping (parasitic frequency modulation), etc. To overcome them, as in radio engineering technique, an external RF-to-optical conversion using a separate device titled "optical modulator" is in common practice for MWP circuits. As in RF systems, there are two classes of optical modulators: phase and amplitude ones; the latter in connection with the specialties of lightwave transmission called "the intensity modulator". Building principles and layouts of microwave-band optical modulators as well as initial equivalent-circuit models are described elsewhere [6]. Below, two updated models of optical phase modulator (OPM) and Mach-Zehnder interferometer-based optical intensity modulator (MZM), as such as a novel model for so-called electro-absorption intensity modulator (EAM), are demonstrated and discussed.

3.1. Optical phase modulator model

The core element of OPM model is the phase-shifting cell (PSC). **Figure 6** depicts the equivalent circuit of PSC, where the phase shift is simulated by the library varactor model VRCTR, whose nonlinear characteristic is extracted from the measured data. The phase shift of the quasi-optical signal is fed to the cell output via a diplexer acting as a high-pass filter. The

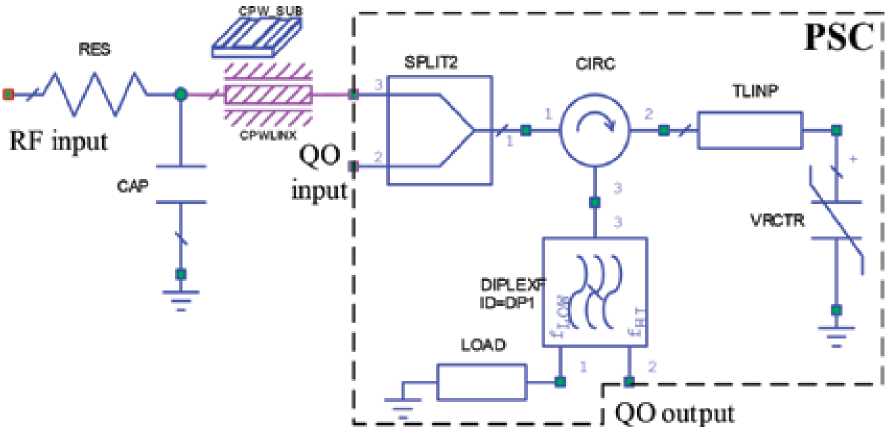

Figure 6. The model of phase-shifting cell.

difference from the known model [6] is the larger correctness due to the introduction of library models of transmission line with frequency-dependent loss TLINP, symmetric coplanar line with table-based interpolation CPWLINX, and so on.

Figure 7 shows the equivalent model of optical phase modulator including PSCs as subcircuits. The number of PSCs is increased to 4 to provide a quasi-linear adjustment of the insertion phase shift within more than 180°, typically required for OPM operation. The resulting phase shift is formed in the OPM as the algebraic sum of the phase shifts of the each PSC, since the signal at the optical frequency sequentially passes through all the cells.

Figure 8 exemplifies the simulation results demonstrating the linearity of the phase shift versus control voltage in PSC (a) and 35-dB suppression of higher harmonics in output spectrum (b).

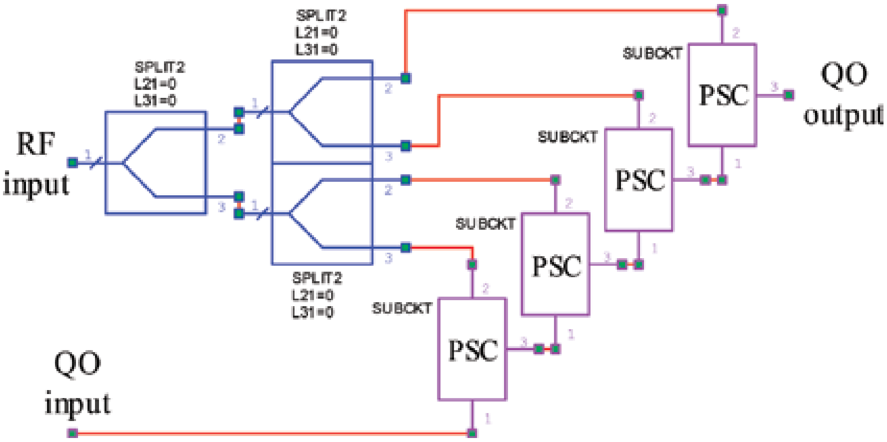

Figure 7. Model of optical phase modulator.

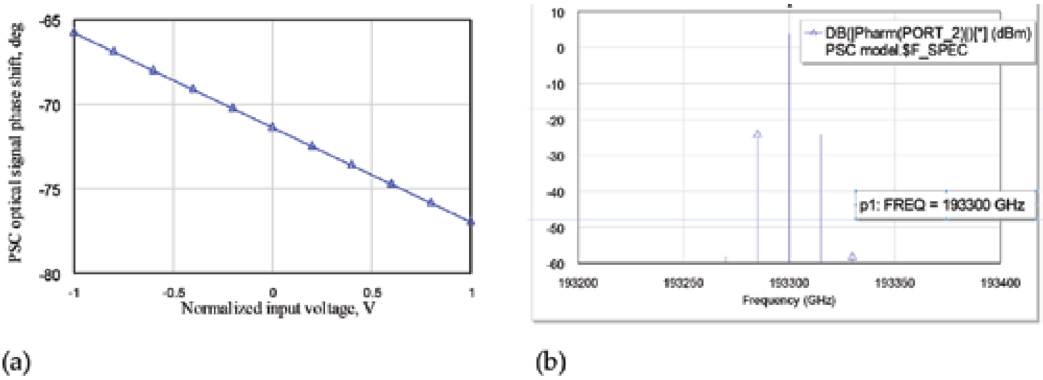

Figure 8. The examples of simulation experiments: (a) phase-voltage dependence of PSC and (b) quasi-optical spectrum at OPM output.

3.2. Mach-Zehnder interferometer-based intensity modulator model

As is known [6], an optical intensity modulator of a MZM type contains a two-arm interferometer, in each arm of which an optical phase modulator is introduced. **Figure 9** depicts the AWRDE model of optical MZM with two OPMs of **Figure 7** as subcircuits. Inside it, the RF signal is applied in antiphase to the inputs of both OPMs via the coplanar transmission line CPWLINX and the ideal splitter SPLIT2. The output channel of one of the OPMs includes two phase-shifter library elements PHASE2, of which the first is responsible for setting the operating point on the MZM transfer characteristic and the second PHASE2 adjusts a fixed phase difference in the arms of realistic MZM. The interference of two phase-modulated signals is carried out at the output of the splitter model SPLIT2. The output attenuator is used to calibrate the power loss of the optical signal introduced by the MZM.

Figure 10 exemplifies the simulation results demonstrating the advantage in the bandwidth and linearity of the external RF-to-optical conversion using a MZM compared to direct one. In particular, **Figure 10(a)** simulates the optical modulated spectrum using the RF tone of 15 GHz and the same input power as in Section 2.2. Comparison with **Figure 5(a)** shows an increase in

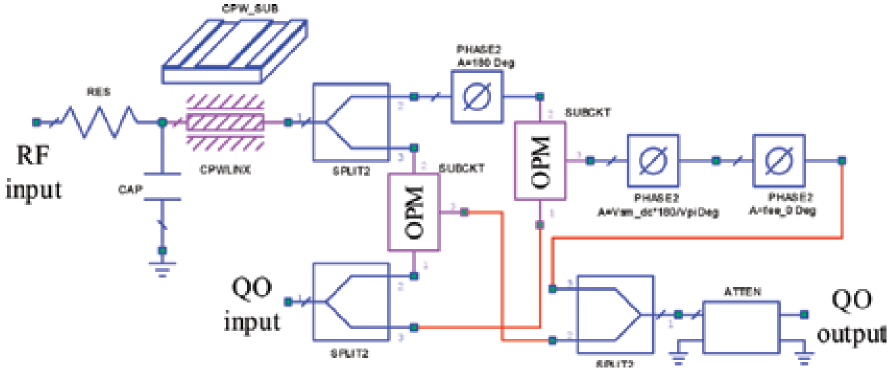

Figure 9. Mach-Zehnder interferometer-based intensity optical modulator model.

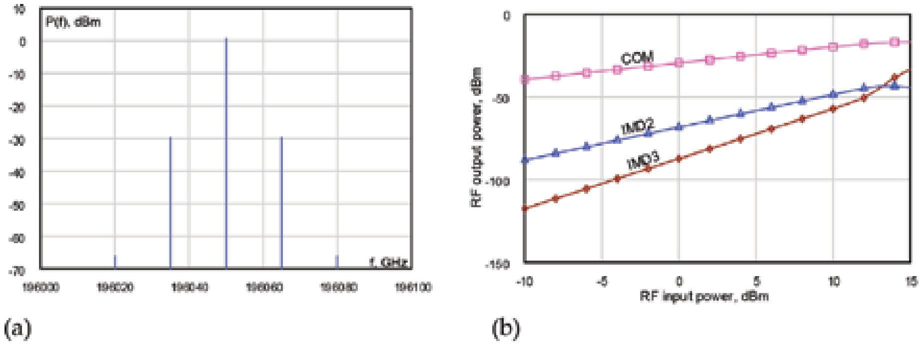

(a)

(b)

Figure 10. The examples of simulation experiments: (a) optical modulated spectrum and (b) large-signal transmission characteristics.

the suppression of the second harmonic by more than 30 dB. Besides, **Figure 10(b)** simulates the dependence of RF output power (after ideal optical-to-RF conversion) on input RF power for the fundamental RF modulation tone (COM), 2-order intermodulation distortion (IMD2), and 3-order intermodulation distortion (IMD3) that shows the better linearity feature than a power microwave transistor.

3.3. Electro-absorption effect-based intensity modulator model

In spite of high linearity of RF-to-optical conversion, the main shortcoming of MZM is bulky sizes, which is a concern for a number of very important radio engineering applications. An intriguing solution to the problem is the usage of an electro-absorption intensity modulator (EAM) that can be integrated with a laser chip [15]. **Figure 11** depicts the AWRDE model of optical EAM. The nonlinear model of EAM is implemented based on the modified Materka field effect transistor (MATRK) library model. The EAM model includes two MATRK elements, which are controlled by a RF signal and act as attenuators that are connected in serious to the quasi-optical channel. The use of two MATRK elements provides deep intensity (amplitude) modulation of the optical carrier. The limits of the dynamic range for the input signals are determined by the selection of the parameters of the library resistor models (RES). The circuit is terminated by BPFB and closed-form amplifier (AMP) library models to eliminate higher harmonics and calibrate the loss inserted by the EAM path (for AMP, any gain value including less than 0 dB could be set). In addition, there are three ideal isolator models (ISOL8R) to ensure the isolation of the inputs and outputs.

Figure 12 exemplifies the simulation results demonstrating the advantage in the bandwidth and linearity of the external RF-to-optical conversion using an EAM compared to direct RF/O one but some disadvantage in compare to external RF/O conversion by a MZM. In particular, **Figure 12(a)** simulates the optical modulated spectrum using the RF tone of 10 GHz and the same input power as in Section 2.2. Comparison with **Figure 5(a)** shows an increase in the suppression of the second harmonic by more than 20 dB. Besides, **Figure 12(b)** simulates the dependence of RF output power (after ideal optical-to-RF conversion) on input RF power for the fundamental RF modulation tone (COM), 2-order intermodulation distortion (IMD2), and 3-order intermodulation distortion (IMD3) that shows the linearity features compared to middle power microwave transistor.

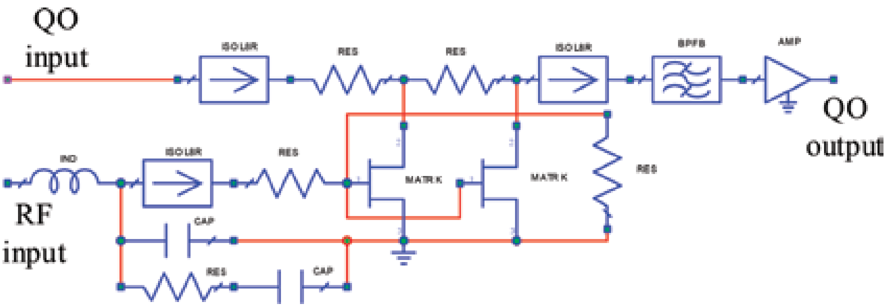

Figure 11. Electro-absorption effect-based intensity modulator model.

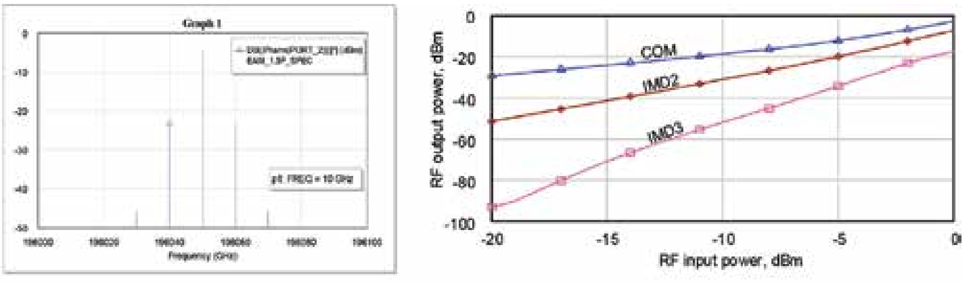

(a) (b)

Figure 12. The examples of simulation experiments: (a) optical modulated spectrum and (b) large-signal transmission characteristics.

4. Direct optical-to-RF conversion

Nowadays, there is a plurality of direct optical-to-RF conversion elements (photodetectors) but only photodiodes of so-called PIN structure are in common use for analog fiber-optic systems. Among them, long wavelength GaInAs-based PIN photodetectors (PD) are ubiquitous in modern MWP circuits due to their inherent combination of ultra-high speed, high sensitivity, and linearity features [16]. Early, we described and studied in detail the AWRDE nonlinear model of microwave-band PIN PD [9, 10]. **Figure 13** shows the updated more realistic PD model where noise sources (INOISE) including shot noise of photodiode and heat noise of the equivalent resistors (RES) are taken into account. From the viewpoint of the RF circuitry, a PIN PD can be modeled as a current source with high output impedance that is imitated by the library model of voltage controlled current source (VCCS). Besides, the nonlinear features are emulated by temperature-dependent diode model (DIODE1) and barrier capacitance of p-n junction (PNCAP) tunable in according with applied reverse voltage from DCVS model. The linear circuitry representing the frequency distortions due to stray PD elements agrees with small-signal PD model that was described elsewhere [17].

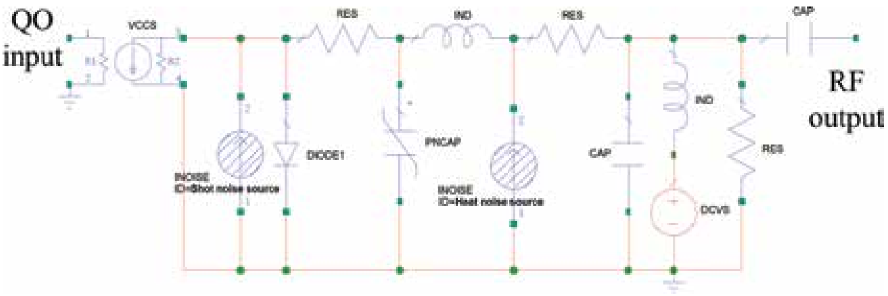

Figure 13. AWRDE nonlinear model of microwave-band PIN photodetector.

The collection of photo-detecting elements includes a number of advanced constructions. The most feasible among them is a balanced one that has an advantage of more linear O/RF conversion [14]. **Figure 14** depicts the AWRDE model of a balanced photodetector.

As well-known from radio-engineering technique, the circuit consists of two arms and each of them includes the photodetector model of **Figure 13** as subcircuit. To provide antiphase excitation of the subcircuits, there is a library reciprocal model of phase shifter PHASE2 in the upper arm. **Figure 15** exemplifies the simulation results for the both types of direct O/RF conversion elements under consideration. In particular, **Figure 15(a)** simulates small-signal frequency response ($|S_{21}|$) of realistic PD using **Figure 13**'s model. As seen, the 3-dB bandwidth is near 20 GHz. Besides, **Figure 15(b)** simulates the dependence of RF output power on input RF power (before ideal RF-to-optical conversion) for the fundamental RF modulation tone (COM) and 3-order intermodulation distortions for the models of **Figure 13** (line 1) and **Figure 14** (line 2). In the figure, one can see two characteristic cross-points of the lines 1 and 2 with the line "COM." These points are termed as output intercept points of 3-order (OIP3) representing very important metric of O/RF conversion linearity [14]. Following the results, one can conclude that firstly, photodetector demonstrates the most linear conversion feature in compare to MZM (**Figure 10(b)**) or EAM (**Figure 12(b)**) and secondly, balanced version of

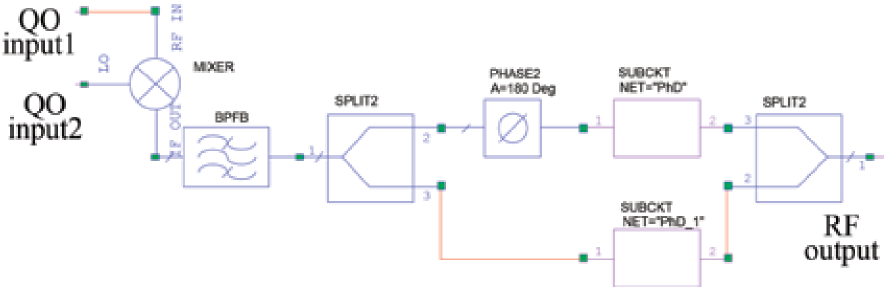

Figure 14. AWRDE model of a balanced photodetector.

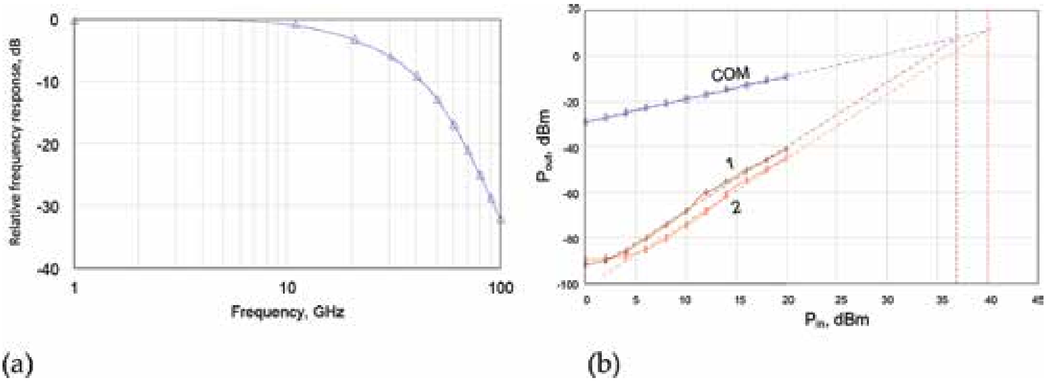

Figure 15. The examples of simulation experiments: a—small-signal frequency response; b—large-signal transmission characteristics of the single-ended (1) and balanced (2) photodetectors.

photodetector has near 3-dB advantage in linearity. The both conclusions and the OIP3 values (37–40 dBm) received by the simulation are in close coincidence to modern realistic photodetectors [9, 14].

5. Passive optical components

Low-loss, interference-insensible transmitting is the most attractive feature of an optical fiber for diverse processing in photonic area. As a part of a MWP circuit, it may be defined as a medium connecting RF-to-optical and optical-to-RF converters. In general, in comparison with a coaxial cable, the optical waveguide has three orders of magnitude less attenuation, the bandwidth independent of the RF signal frequency, much better weight and size characteristics, as well as the weaker phase-to-temperature dependence of the transmitted RF signal. Nevertheless, the quality of the transmitted signal may deteriorate due to a number of limiting factors, for example, dispersion, reflection, scattering, nonlinearity, etc. Another important advantage of an optical fiber is that it can be used to design extremely narrow-bandwidth pass-band and notch filters. Below, two new AWRDE behavior models of single mode optical fiber and fiber-based ultra-narrow-bandwidth filter are demonstrated and discussed.

5.1. Single-mode fiber model

Figure 16 depicts AWRDE reciprocal models of single-mode optical fiber feasible for various operating regimes of a realistic fiber-optic link. The first model (**Figure 16(a)**) represents the transmission on a single optical carrier with multiple modulating RF signals (so-called, subcarrier multiplexed mode). Here, a set of limiting factors are taken into account, such as chromatic dispersion, time delay, loss, temperature dependence of characteristics, as well as cross-interference between RF channels.

The basic element for the model of **Figure 16(a)** is the library model of ideal transmission line with loss (TLINP). A mode propagating across the line is specified by its effective dielectric constant and per-unit-length attenuation at user specified frequency. The model scales loss with evaluation frequency. In the model, the frequency band of one 100-GHz optical channel is divided into 16 discrete bands of equal width (more than 6 GHz). Each of them is provided by one TLINP with values of the dielectric constant and attenuation corresponding to a central frequency of a specific band. All TLINPs have the same length, equal to the length of the optical fiber, and are combined using ideal multiplexer models (MUX). The first MUX shares the spectrum of the quasi-optical signal between 16 sections, each of which exploits the corresponding TLINP. The second MUX restores the signal spectrum.

Besides, the second model (**Figure 16(b)**) represents the transmission on a multiple optical carriers (so-called, wavelength division multiplexed (WDM) mode). Here, a cross-interference noise between the carriers is added to the above limiting factors. The main element of each QO channel (CHL) is subcircuit (SUBCKT "CHL"), which structure is discussed above for a single spectral channel. Sixteen SUBCKT "CHL" ones correspond to 16 standard channels of the

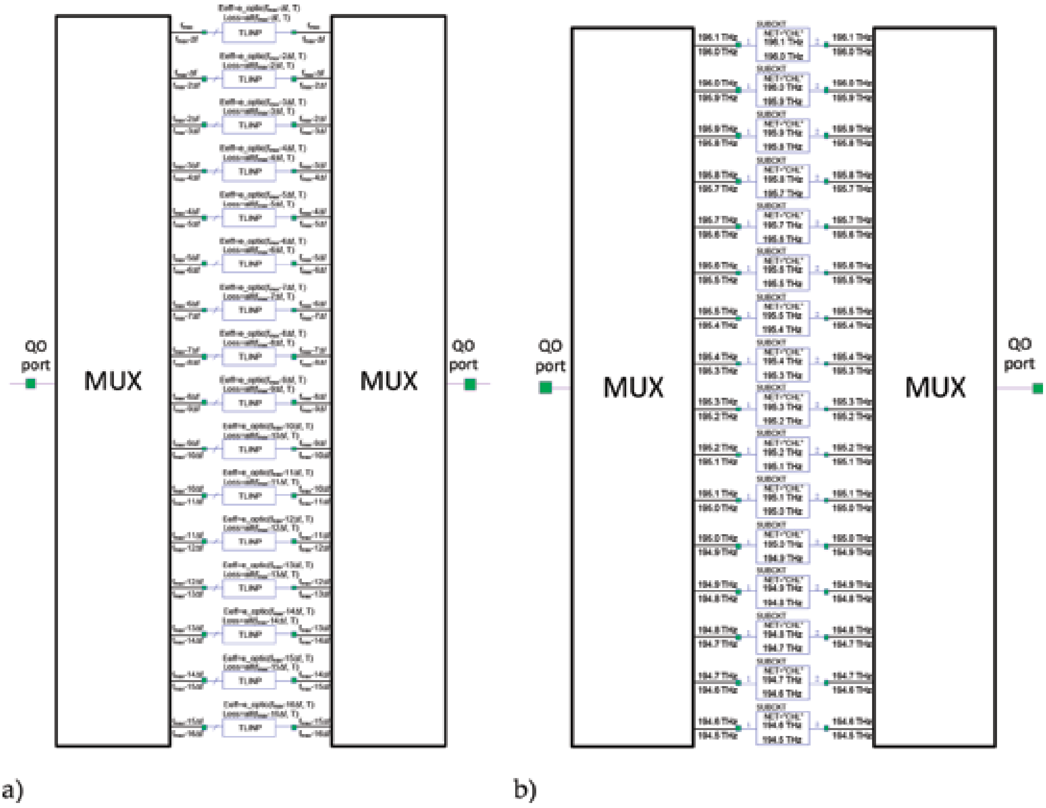

Figure 16. AWRDE models of single-mode optical fiber in various operating regimes: (a) with subcarrier multiplexed mode; and (b) with wavelength division multiplexed mode.

WDM system, so the overall number of RF channels to be transmitted simultaneously is 256. In the model, all SUBCKT "CHL" groups are combined/divided using the same MUX library models that provide the distribution of the input QO spectra according to the corresponding

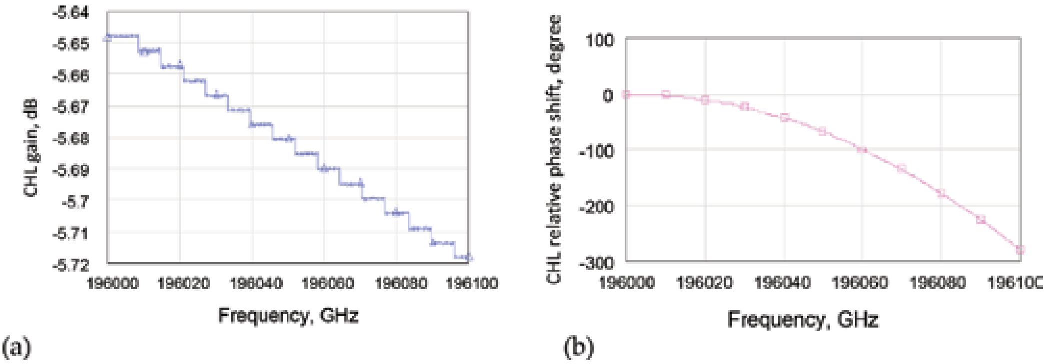

Figure 17. The examples of simulation experiments: (a) QO channel gain versus QO frequency of single-mode optical fiber; (b) QO channel relative phase shift versus QO frequency of single-mode optical fiber.

subcircuits over the single fiber and further restoration of the group spectrum. The schematic can be re-tuned to another bandwidth of QO channels by changing the internal model settings.

Figure 17 exemplifies the simulation results for the both types of single-mode optical fiber models under consideration at room temperature, where QO frequency dependences of CHL gain (a) and of CHL relative phase shift (b) for the fiber length of 30 km are simulated. As seen, the average normalized loss (inverse to gain) is near 0.19 dB/km that equal in this frequency band to the same parameter of standard SMF-28 fiber. In additional, the difference in losses for one 100-GHz optical channel does not exceed 0.07 dB only. Besides, normalized phase-to-temperature shift of RF signal being transmitted over fiber is near 0.1°/GHz/km/°C that corresponds to known data [14].

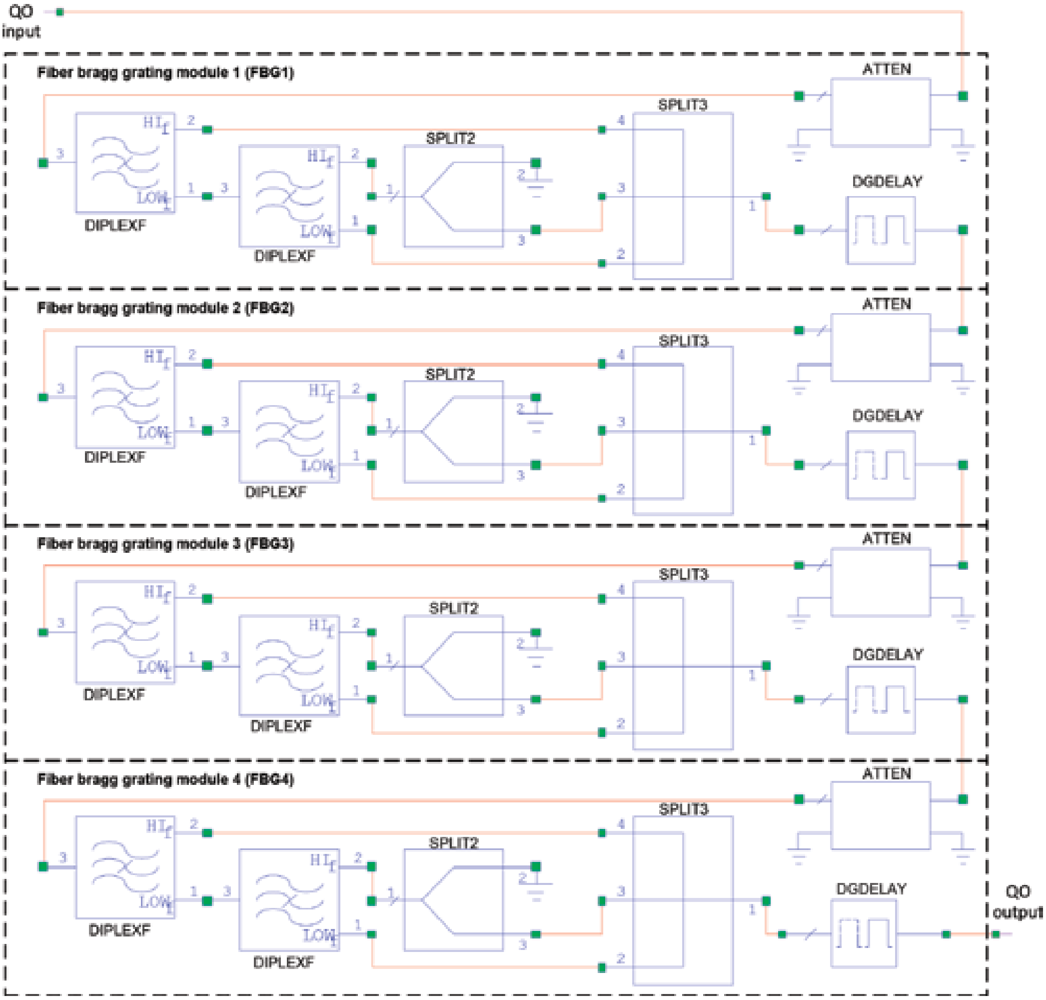

Figure 18. Four-channel AWRDE notch Bragg grating filter model.

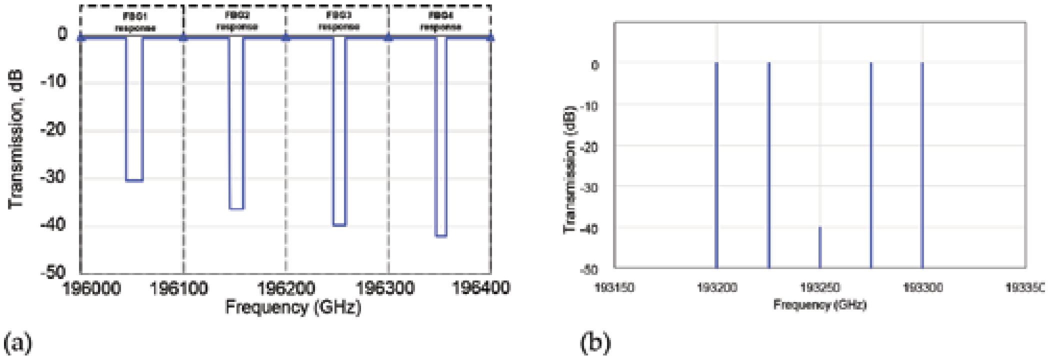

Figure 19. The examples of simulation experiments.

5.2. Narrow-band multichannel optical filter model

Another important element of **Figure 1**'s photonic area used for processing RF signals (filtration, delay) is the notch Bragg grating (NBG), whose optical bandwidth may be as narrow as some hundreds of MHz. **Figure 18** shows 4-channel AWRDE NBG model. Fiber Bragg grating module of each channel (FBG1-FBG4) consists of two library models of ideal passive frequency diplexer DIPLEXF each of them specifies two frequency ranges (low and high) to extract the cutoff band at the output of the second DIPLEXF. In each of the channels, through output 2 of the first DIPLEXF and output 1 of the second DIPLEXF, power is allocated outside the cut-off band. This power is summed by the model SPLIT3 and fed to the next channel. The SPLIT2 unit provides the reflection of the main power in the dedicated band and the transition of some of this power to the next channel (for SPLIT2: $S_{21} = 0$ dB and $S_{31} = -30$ dB), thus incomplete reflection is modeled. The residual power from the output 3 of the element SPLIT2 is fed to the element SPLIT3, where it is summed with the signal power outside the cut-off band. The closed-form models of attenuator (ATTEN) and ideal digital time delay element (DGDELAY) insert the attenuation and time delay of the optical signal in each of the Bragg grating channel, respectively.

Figure 19 exemplifies the simulation results for 4-channel NBG filter transmission response (a) and the QO spectrum at the output of the filter model when the same power QO signals inside the band of FBG3 are inputted. As seen, a rejection level of 40 dB is provided.

6. Simulation of microwave-photonics-based RF circuits

In the previous sections, the requisite active and passive AWRDE models for the MWP circuit design were demonstrated and the results of the key simulation experiments were highlighted. Following them, below we will describe some models and modeling results for MWP circuits as the enablers for time-delay processing in photonic area.

6.1. Fiber-optic delay line of RF-signals

Fiber-optic delay line (FODL) is one of the most feasible units of MWP circuitry [14]. The layout of single-channel FODL is very simple and consists of RF/O converter, single-mode optical fiber of a corresponding length (delay ≈ 4.8 ns/m), and O/RF converter. **Figure 20** shows the AWRDE model of single-channel FODL including in order a single-carrier model of semiconductor laser (see Section 2.1, **Figure 2**), a model of single-mode optical fiber (see Section 5.1, **Figure 16(a)**), and a model of PIN photodetector (see Section 4, **Figure 13**) as subcircuits.

Figure 21 exemplifies the simulation results for RF-dependence phase shift and delay of the RF pulse. In particular, **Figure 21(a)** represents the relative phase shift versus frequency of RF signal modulating optical carrier that propagates over the fiber length of 1 m (the delay is near 4.8 ns). As follows from the figure, the phase shift increases linearly with frequency and its slope is approximately 1700° per GHz, which is consistent with the theory of RF delay lines. Besides, **Figure 21(b)** demonstrates the oscillogram of the input and output RF pulses for the fiber length of 3 m. As seen, due to the wide modulation band embedded in the laser and photodetector models (**Figures 3(a)** and **15(a)**, correspondingly), the delay of the radio pulse is exclusively determined by the retarding effect in the optical fiber.

6.2. Temperature-compensated fiber-optic delay line of RF signals

The key issue in realistic FODLs is a fiber thermal instability in operating conditions, because the temperature variations result in remarkable phase shift and the corresponding group time delay changes of the RF signals that is invalid for a set of important applications. There are two

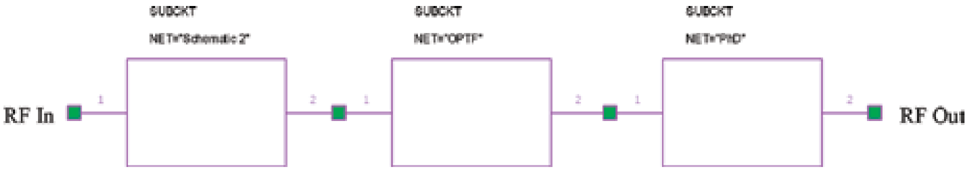

Figure 20. AWRDE model of single-channel fiber-optic delay line of RF signals.

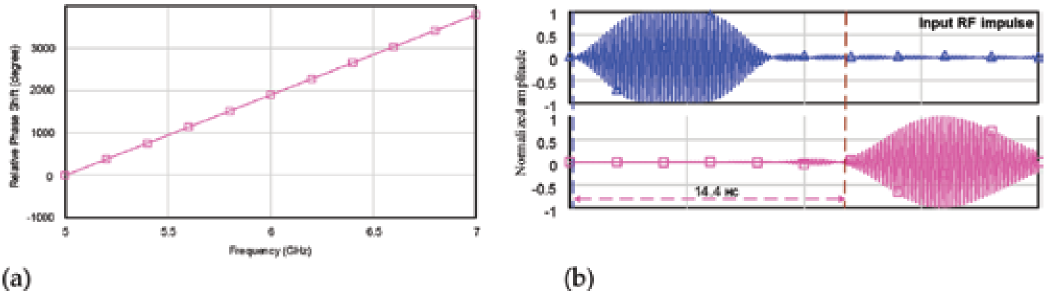

Figure 21. Examples of the simulation results for single-channel FODL of RF signals.

main directions to design temperature-compensating fiber-optic delay lines (TC-FODL) including feedback or phase conjugation concept. The disadvantage of the first one is the limited adjustment range of the RF device, the phase of which is to be regulated depending on the temperature variation. **Figure 22** shows the layout explaining the principle of the second concept that is free of the above shortcoming [18]. In the scheme, the effect of compensation of the temperature-induced change in the delay time is provided by synchronous variation of the fiber length during the triple pass of the modulated by RF frequency optical signal along the same fiber. A detailed explanation of the operation principle for this scheme is given in [18].

Figure 23 demonstrates the proposed ultra-wideband AWRDE model of TC-FODL simulating the operation principle of the schematic in the **Figure 22**. Therein, according to the scheme, the frequency F_m of the input RF signal, first of all, is divided in half and multiplied by one and a half times. The converted frequencies are allocated using library models of bandpass filters BPFB, each of which is tuned to the appropriate frequency. Further, the double trip of the optical carries on the frequencies ν_1 and ν_2 modulated by the RF signal of frequency $1/2F_m$ is represented by means of the semiconductor laser models (**Figure 4**), the optical fiber model of **Figure 16(b)**, and the photodetector models of **Figure 13**. Finally, in the result of mixing double converted RF signal of frequency $1/2F_m$ with RF signal of frequency $3/2F_m$ using library model MIXER, the input RF signal of frequency F_m is recovered exploiting the library model BPFB

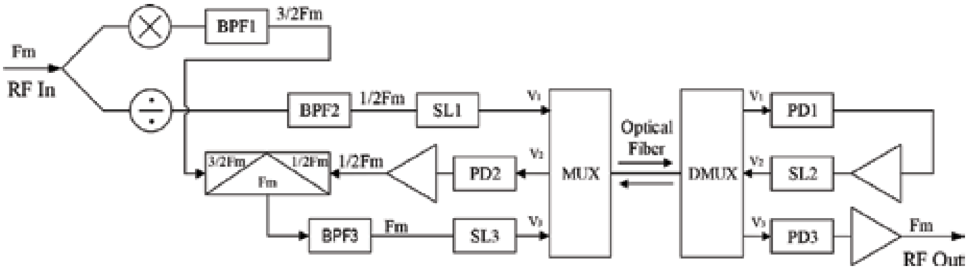

Figure 22. Temperature-compensated fiber-optic delay line of RF signals.

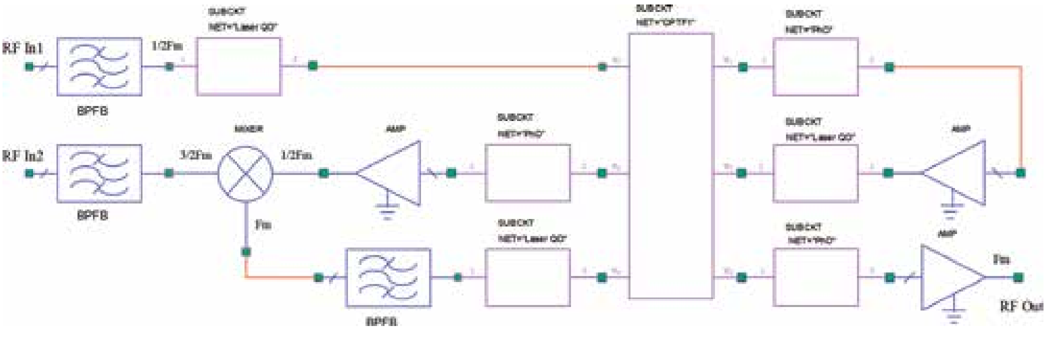

Figure 23. AWRDE model of temperature-compensated fiber-optic delay line of RF signals.

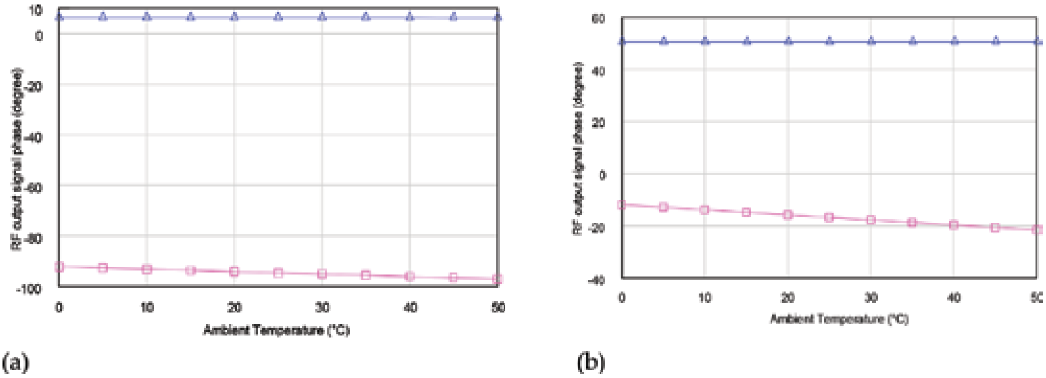

Figure 24. Examples of the simulation results for TC-FODL of RF signals: (a) RF frequency 2.5 GHz; and (b) RF frequency 5 GHz.

and the output after one more trip over TC-FODL on the optical carrier ν_3 that are imitated by the separate models of laser and photodetector and the same model of optical fiber.

Figure 24 exemplifies the simulation results for the proposed TC-FODL model of 40 m in length examining its phase-to-temperature characteristics at the RF frequencies of 2.5 GHz (a) and 5 GHz (b) that are performed by triangles. For comparison, the same plots include the simulation results for the FODL model of **Figure 20** that are performed by squares.

Based on the graphs, the following resume can be drawn. Despite the much higher stability of the silica fiber's phase-to-temperature characteristic compared to the coaxial cable [14], the FODL under the study without compensation (the model of **Figure 20**) introduces the phase distortion increasing at higher frequencies of RF signal that is unacceptable in many practical cases. This distortion regardless of RF signal frequency is eliminated by using a special MWP circuit, the example of which was modeled above.

7. Conclusions

In the chapter, a new approach to design the equipment for a future generation of microwave-band radar, electronic warfare, and wireless telecom systems based on microwave photonics technology using well-known microwave-electronic software tool NI AWRDE is proposed and discussed. As a first part of it, updated and new models of key active and passive elements for microwave-photonic circuits were considered that perform direct and external RF-to-optical conversion and processing of RF signals in the optical range, which leads to an improvement in such important characteristics as size, weight and power, electromagnetic and environmental compatibilities, and immunity to external interferences. As an outcome of the conducted simulation experiments, it was shown that the main parameters and characteristics of the optoelectronic and optical elements considered correspond to the real product analogs. In particular, the comparative modeling has verified that the highest level of linearity, superior to modern transistor amplifiers, is provided in the process of external RF-to-optical conversion by means of an Mach-Zehnder optical modulator and in the process of optical-to-RF conversion using a PIN photodetector. The results of the experimental comparison against the main part of the above-simulated characteristics, which validate the accuracy of the proposed models, are described elsewhere [5–13].

Based on the element models and results of simulations, in the second part of the chapter, we presented two new AWRDE models and the results of model experiments for fiber-optic delay line that realized time-delay processing of RF signals in photonic area. In the course of the model experiment, the way of eliminating phase distortions of delayed RF signal caused by the fluctuation of the ambient temperature under the conditions of application was confirmed.

Acknowledgements

This work was supported by the Russian Foundation for Basic Research, Grant No. 17-57-10002.

Conflict of interest

The authors declare the lack of the "conflict of interest."

Author details

Mikhail E. Belkin[1]*, Vladislav Golovin[2], Yuri Tyschuk[2], Mikhail G. Vasil'ev[3] and
Alexander S. Sigov[1]

*Address all correspondence to: belkin@mirea.ru

1 Moscow State Technological University (MIREA), Scientific and Technological Center "Integrated Microwave Photonics", Moscow, Russian Federation

2 Sevastopol State University (SevSU), Sevastopol, Russian Federation

3 Kurnakov Institute of General and Inorganic Chemistry, Russian Academy of Sciences, Moscow, Russian Federation

References

[1] Izutsu M, Itoh T, Sueta T. 10 GHz bandwidth traveling-wave $LiNbO_3$ optical waveguide modulator. IEEE Journal of Quantum Electronics. June 1978;**14**(6):394-395

[2] Seeds AJ, Williams KJ. Microwave photonics. Journal of Lightwave Technology. 2006; **24**(12):4628-4641

[3] Capmany J, Novak D. Microwave photonics combines two worlds. Nature Photonics. 2007;**1**(1):319-330

[4] Waterhouse R, Novak D. Realizing 5G. IEEE Microwave Magazine. 2015;**16**(8):84-92

[5] Belkin ME, Iakovlev V, Sigov AS, Tyschuk Y, Golovin V. An advanced approach to simulation of super-wide bandwidth information and communication systems combining microwave and photonic industrial technologies. European Modelling & Simulation Symposium (EMSS2016). Cyprus; 26–28 Sept. 2016. pp. 141-147

[6] Belkin ME, Golovin V, Tyschuk Y, Sigov AS. A simulation technique for designing next-generation information and communication systems based on off-the-shelf microwave electronics computer tool. International Journal of Simulation and Process Modeling (IJSPM). 2018. (In print)

[7] Belkin ME, Belkin L, Sigov AS, Iakovlev V, Suruceanu G, Kapon E. Performances of microwave-band analog signal transmission using wafer-fused long wavelength VCSELs. IEEE Photonics Technology Letters. 2011;**23**(20):1463-1465

[8] Belkin ME, Iakovlev V. Microwave-band circuit-level semiconductor laser modeling. In: EMS 2015: 9th European Modeling Symposium on Mathematical Modeling and Computer Simulation. Madrid, Spain; 2015. pp. 1-3

[9] Belkin ME. Multiscale computer aided design of microwave-band P-I-N photodetectors. In: Gateva S, editor. Photodetectors. Croatia: InTech; 2012. pp. 231-250

[10] Belkin ME, Sigov AS. Circuit-level large-signal modeling of microwave bandwidth photodetector. International Conference on Electromagnetics in Advanced Applications ICEAA 2015 Torino; Italy; 7-11 Sept. 2015. pp. 1587-1589

[11] Belkin ME, Golovin V. Microwave electronic CAD modeling of microwave-band optoelectronic oscillator based on long wavelength VCSEL. In: COMCAS 2015: Proceedings of the International Conference on Microwaves, Communications, Antennas and Electronic Systems; Tel Aviv. Israel. pp. 1-3

[12] Belkin ME, Tyschuk Y. Microwave electronic CAD modeling of microwave photonic devices based on LW-VCSEL mixing. In: ICMAP 2015: Proceedings of the II International Conference on Microwave and Photonics; Dhanbad, Bihar. India. pp. 1-3

[13] Belkin ME, Golovin V, Tyschuk Y, Sigov AS. Comparison of RF photonics-based beamformers for super-wide bandwidth phased array antennas. IOP Conference Series: Materials Science and Engineering. 2017;**198**:1-4

[14] Urick VJ, McKinney JD, Williams KJ. Fundamentals of Microwave Photonics. New Jersey: Hoboken; 2015

[15] Fukano H, Akage Y, Kawaguchi Y, Suzaki Y, Kishi K, Yamanaka T, Kondo Y, Yasaka H. Low chirp operation of 40 Gbit/s electroabsorption modulator integrated DFB laser module with low driving voltage. IEEE Journal of Selected Topics in Quantum Electronics. 2007;**13**(5):1129-1134

[16] Yu PKL, Wu MC. Photodiodes for high performance analog links. In: Chang WS, editor. RF Photonic Technology in Optical Fiber Links. University of Cambridge, England: Cambridge university press; 2002. pp. 231-254

[17] Belkin ME, Dzichkovski NA. Research of microwave-bandwidth p-i-n photodetectors. In: EUROCON 2009; St. Petersburg; May 2009. pp. 193-196

[18] Yin F, Zhang A, Dai Y, Ren T, Xu K, Li J, et al. Phase-conjugation-based fast RF phase stabilization for fiber delivery. Optics Express. January 2014;**22**(1):878-884

Chapter 5

Integration of Hybrid Passive Optical Networks (PON) with Radio over Fiber (RoF)

Shahab Ahmad Niazi

Additional information is available at the end of the chapter

http://dx.doi.org/10.5772/intechopen.79299

Abstract

A cost effective, robust, and high capacity access network necessitated to meet the mounting customer demands for bandwidth-desirous services. A remarkable evolution of access networks is observed both in wired and wireless, predominantly driven by ever-changing bandwidth requirements. A wireless connection releases the end user from the restrictions of a physical link to a network that results in mobility, flexibleness, and ease of use. Whereas, optical networks offer immense amount of bandwidth that appease the most bandwidth voracious customers compared to bandwidth limited wireless networks. The integration of wired and wireless domains in the access landscape that presents a technical analysis of optical architectures suitable to support radio over fiber (RoF) is the objective of this chapter. Investigate the main trends that drive the merger of fiber and wireless technologies in access networks. Moreover, study the primary terms and the particular transmission features of integrated fiber-radio links to form a well-defined classification of hybrid systems and techniques. This work also recognizes the major problems for realization of RoF systems and examines the limitation, advantages, and diversity of integrated RoF-PON technology.

Keywords: radio over fiber, passive optical network (PON), hybrid PON, next generation PON (NG-PON-2), millimeter wave, IEEE 802.11ad

1. Introduction

In the upcoming telecom networks, end users need mobility, high speed, and large capacity. Luckily, we know the solution, wireless provides the mobility and optical fiber provides the speed and capacity. Traditionally, the radio signals were typically employed for voice and low rate data communication systems, while optical signals applied for high bandwidth metro and long haul wired communication systems. The existing network technologies (i.e. twisted pair, coaxial cable, optical fiber, and wireless links) allow variable range of mobility and bandwidth to end users [1]. The current technologies have very diverse techniques of signal generation, transmission, and reception. Moreover, their installation, working, and maintenance are also different in design, structure, and implementation.

The cost of access, metro, and core network is greatly impacted by Internet traffic growth [2]. It is expected that Internet traffic will continue its exponential growth trend in the future due to the large scale spreading of smart phones, tablets, and laptops. Moreover, mobile and fixed broadband access connections (LTE, WLAN, and FTTx) will have extensive growth in coming years all over the world. These developments will permit end users to relish social networking, cloud computing, online shopping, and multimedia applications. The terabits per second in back bone networks with gigabits per seconds in access network is shaping new life in telecommunication industry [3]. Furthermore, 3D, HDTV, and UHDTV cable television transmission is accessing home users. It would lead to give a motivation for the development of many services that face band width limitations in present networks. High speed transmission gives impetus to develop competitive signal processing platforms and equally high speed switching devices [4].

However, it is the great challenge for all the network technologies to meet the requirements of the increasing demand of broadband and mobile communications. The present network technologies either wireless or wired just fulfill a partial demand due to inherent limitations. Therefore, realizing the growing requirements and limitations of the network technologies, there appears a need of integration to overcome the limitations of one technology with aid of some other technology [5]. The enormous opportunities arisen to design and develop future high data rate networks by combining the advantages of wireless and fiber technologies. A high throughput networks anticipated after the coexistence of both radio frequency electronics and fiber optics to develop RoF systems. The term RoF is used for modulating a light beam by radio frequency signal and propagating through an optical fiber link to finally transmit radio signal in free space.

The RoF system can adequately resolve the generation, propagation, and synchronization issues of broadband signal. RoF is a perfect technology for the integration of wireless and wired networks that it aggregates the best features of both communication technologies. Hence, RoF provides the best optimum solution to end users by allowing them to maintain their mobility along with the needed bandwidth for both current and future communication/entertainment applications. The RoF networks also deliver greater geographical coverage and tractability as compared to use either wired or wireless technology. Furthermore, extremely high spectral efficiency can be attained by optical generation of radio frequencies that is the most important parameter for long haul networks. RoF also provides frequency synchronization to solve the performance constraints of wireless interconnect systems. Finally, RoF system offers numerous advantages in different levels of communication systems.

After a brief introduction of our topic in section 1, a comprehensive overview about integration of RoF is presented in second section. In third section, the candidate optical technologies to realize radio over fiber are discussed. The complete network architecture concentrated on pragmatic execution strategies of radio over fiber systems, along with millimeter wave applications and standardization (IEEE 802.15.3c, ECMA-387, Wireless gigabit alliance, IEEE 802.11ad) are presented. Finally, this chapter concluded with future dimensions.

2. Integration of RoF with PON

The RoF technology is the propagation of wireless signal through low loss optical fibers to achieve long reach, which is not possible by direct transmission of radio signals. This coexistence of wireless/optics systems paved the way for many promising solution for broadband networks. It also facilitates the network and service providers to offer mobility, bandwidth, and multi ways of connectivity to customer by integrating wireless and wire line solutions [6]. The broadband modulation techniques are being implemented to enable baseband and RF technologies to coexist together in the same access network. The high bandwidth capabilities of the optical fiber can effectively be utilized by taking advantage of advances in both wired and wireless telecommunication systems. A mix of services and technologies such as PON, cellular mobile, and fixed wireless base stations are integrated and served by a single fiber infrastructure as illustrated in **Figure 1**. This integrated optical infrastructure involved independent modulation of baseband and RF signals and then multiplexed together in the access domain. This hybrid radio-optic system is considered as a very attractive solution to offer low-cost multi gigabit wireless services. The integration of both technologies over the same

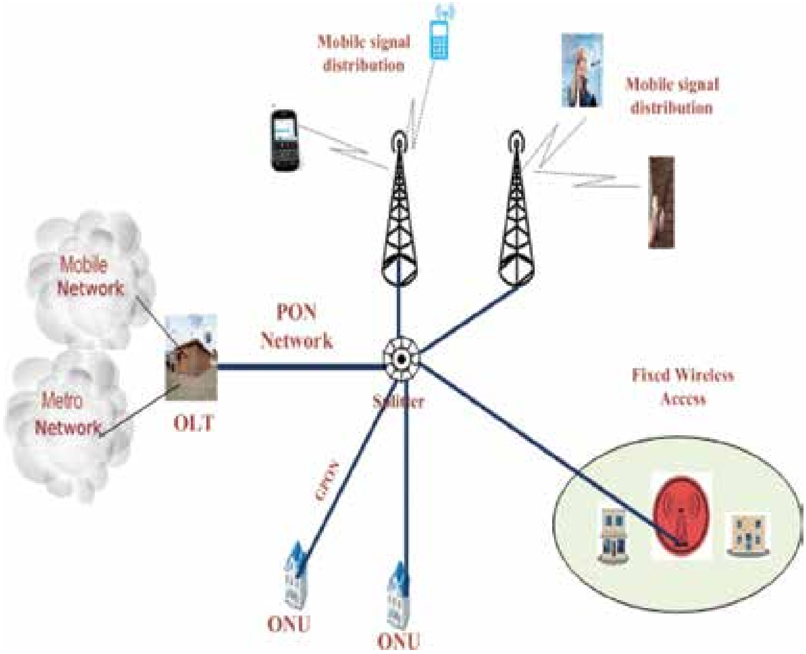

Figure 1. Integrated RoF and PON system.

optical infrastructure is evaluated on the basis of existing standards of fiber access and radio networks. The integrated multiplexing techniques either wavelength division multiplexing-time division multiplexing (WDM-TDM) or WDM-subcarrier multiplexing (SCM) are two preferable choices for serving higher user density RoF antenna sites on optical infrastructure.

After specifying the preferable network architecture for integrated systems, the possibility of analog or digital transmission modes is analyzed to carry radio signals. The mapping of radio signals on hybrid PON network is assessed by evaluating their bandwidth capacity requirements. The first generation of the primary standards defined for time division multiplexing (TDM) PON such as gigabit PON (GPON) and Ethernet PON (EPON) are insufficient to fulfil the bandwidth requirement for digital protocols designed for multi-gigabit systems. In such situations, the sequential upgradation to high data rate PONs from next generation XG-PON/10G EPON to NG-PON2 and beyond are recommended.

For implementation of mm-wave RoF networks in pico or femto-cell environment, multipoint to multipoint (MP2MP) architectures are preferred for home networks. In MP2MP architectural design, NxN nodes are used for distributed antenna units. The laser of each antenna unit through the logical mesh network of the nodes is connected to the every photodiodes of this network to provide connectively to every other wireless device in this network. Therefore, all the wireless devices are visible to each other in the same network. Optical MP2MP is preferred topology for small scale mm-wave enable home network.

The ROF system like any fiber-based system has problem of inter symbol interference (ISI) due to fiber dispersion. The dispersion penalty is mainly introduced by optical filters and cascading multiplexing stages in integrated RoF-PON networks. The converged radio-optical signals will face degradation due to dispersion in hybrid network. So, the RoF networks will be designed with simple network architectures to bring the flexibility, reliability and resilience against all transmission impairments.

3. Candidate fiber platforms to implement RoF

In late 1980s, optical fiber systems were introduced in long haul communications to provide high capacity and long distance communication. This development has started a new era of information and telecommunication systems. The available high capacity in back bone network has guided to increase the capacity and data rates in access networks. The legacy copper and radio networks were unable to support very high data rates in last mile networks. Optical fiber-based access networks were introduced to offer high data rates in the access networks. However, the economical and flexible solutions still needed to make it available for everyone. On the other hand, the tele-density in the world is raised to many folds after the unveiling of cellular networks, but they are limited to voice and low data rate communications.

A new access work is required to fulfill the requirement of data devouring applications. To meet this goal, multi-gigabit radio systems were designed in the form of wireless fidelity (WiFi), worldwide interoperability for microwave access (WiMAX), and long term evolution (LTE) systems. Although, these systems can support very high data rates in access network but only when appended with optical fiber systems from central office to base stations. After the introduction of Qualcomm, QCA6320 (60 GHz MAC/BB) + QCA6310 (60 GHz RF transceiver and commercial products (i.e. TP-link AD7200 (Talon), NETGEAR R9000-100EUS Nighthawk X10 AD7200, ASUS RT-AD7200) which are utilizing 60 GHz mm-wave band and offering data rates around 7 Gb/s. To meet such high data demands, optical access network with very high capacity and affordable prices are intended to be designed. Moreover, TV overlay is required with PON to provide ultra-high definition (UHD) TV service with no latency and with all the existing and future auxiliary services of IPTV with minimum cost involved at ONU [7].

It is projected that the rapid development of optical technologies particularly for passive optical networks will continue to ensure cost-competitiveness with current access technologies. For wire-line access networks, point-to-multipoint passive optical network is the leading technology being deployed in many countries in contrary to other available options of network topologies. It is commonly acknowledged that fiber to the home (FTTH) and time-wavelength multiple access (TWMA) PON is the most optimum solution for present and near future that will be able to support the upcoming interactive multimedia services. Other multiple access techniques as wavelength division multiple access (WDMA), optical code division multiple access (OCDMA), or orthogonal frequency division multiple access (OFDMA) still did not find wide scale acceptance for optical access network by network operators due to huge cost involved per customer to implement these techniques. Currently, many advanced hierarchical designs of passive optical networks (PON) are being deployed to implement FTTH. The first generations of PONs (broadband PON, gigabit PON, and Ethernet PON) that were standardized by IEEE and ITU already installed in many countries [8]. Among the numerous approaches proposed for FTTH, hybrid (TDM-WDM) PON technology straightforwardly offers a new dimension for this upgrade. To reduce the cost of ONU, colorless ONU configurations have been suggested to reuse the optical downstream carrier for upstream modulation. However, to reduce the influence of the downstream modulation on the upstream data, different approaches especially the adoption of different modulation formats for downstream and upstream transmissions are recommended. The devices such as chirp managed laser (CML), injection locked Fabry-Parot laser diodes (FP-LDs), semiconductor optical amplifier (SOA), and reflective semiconductor optical amplifier have laid the foundation for colorless ONU in hybrid PON. The extraordinary features of the hybrid passive optical networks and 60 GHz mm-wave RoF technique are motivating the research toward the convergence of both technologies that is the single most important point of this chapter.

Many technologies are recommended for high-bandwidth passive optical networks to deliver required data rates for current and future services. They are 40 Gbit/s time division multiplexing (TDM) PON, wavelength division multiplexing (WDM) PON, orthogonal frequency division multiplexing (OFDM) PON, coherent ultra-dense WDM-PON (UDWDM PON), and time-wavelength division (TWDM) PON [9]. The full service access network (FSAN) group under International telecommunication union (ITU-T) has adopted the TWDM-PON for its next generation PON-2 standardization. A hybrid TWDM-PON system that stacks four 10G-PONs onto a single fiber to deliver 40 Gbit/s integrated capacity in downstream. The ITU-T and FSAN has adopted smooth path for multi gigabit PON (GPON) evolution, based on incremental and targeted at the ultimate goal of migration to NG-PON2, cost effectively making full reuse of deployed fiber infrastructure [9]. The early installation work has already started on next generation of PON (TWDM-PON) in many countries. The path being adopted by network operators is seamless migration to protect their legacy PON architecture investments [10]. The laying of appropriate fiber infrastructure is very important for network operators to cope the requirement of never-ending upgrades.

The hybrid time-wavelength multiplexing for TWDM is certainly less expensive than pure dense wavelength division multiplexing (DWDM) PON [11]. The wavelength leasing option is available besides offering additional bandwidth than legacy TDM-PON [12]. The different operators can utilize wavelength leasing by sending their traffic on different colors (wavelengths) over the same infrastructure. This feeding of different mesh networks feature will be very attractive for Wi-Fi networks operators. The TWDM PON is designed on distinctive characteristic of sequential upgrade that allows the usage of the legacy GPON point-to-multipoint network and involves changes only in optical devices at the optical line terminal (OLT) and optical network units (ONUs). Huawei has proposed a prototype network for TWDM PON employing intensity modulation and offline digital signal processing [13, 14]. The features of XG-PON1 and NG-PON-2 are compared without possible options for implementations of NG-PON2 [15, 16]. A comparison is made between the possible options for wavelength selection and transmitter/receiver design for implementation of NG-PON2 [17].

FSAN did not recommend particular frequency band for downstream band width selection and choice made open for network operators. A possible selection for downstream 4-wavelengths group selection from S-band, L-band, C-band, and O-band is analyzed in our previous study [17]. The optimal transmitter design is also examined between probable options of chirp managed laser diode and Lithium Niobate (LiNbo3) Mach Zehnder modulator along with the option of tunable transceiver or remotely fed colorless ONU [17].

The IUT-T and IEEE have already defined wavelength groups for downstream (S-band: 1480–1500, C-band: 1550–1560, L-band: 1575–1580) and upstream (O-band: 1260–1360) for implementation of GPON and XG-PON [14]. The S-band is primarily defined for GPON, L-band for XG-PON, and C-band for TV overlay. In our previous analysis, we found that the choice of group of four downstream wavelengths can easily be made without uprooting current wavelengths assigned for legacy PONs. Being restricted to currently specified bands for PON, their performances for downstream communication is compared as represented in **Figure 2**. The optimal options to design optical transmitter for data rates 10 Gbit/s or higher are chirp managed laser and conventional LiNbO3 MZ modulator. The modulators were considered as the first choice for access, metro and long-haul networks till very recent [18]. But, the excessive power consumption and bulky size of Mach Zehnder modulator left the market open to better alternatives. However, Mach Zehnder is still the most reliable mean to achieve very high data rates. The chirp managed lasers (CML) is appeared to address the concerns of cost, power consumption, and size of MZ modulators. CML provides intense optical output power on low driving voltage in standard single mode fibers with 50–100 GHz ITU grids spacing for DWDM wavelengths [19]. The remotely fed colorless ONUs and tunable receivers are the two most recent trends for designing of an optical receiver. A tunable receiver made up of a thin film Fabry-Perot tunable semiconductor filter, an avalanche photo diode (APD) and a trans-impedance amplifier (TIA). The current tunable receiver can easily be tuned to more than 16 nm covering part of the ITU-T bands [20]. Whereas, the tunable external cavity laser (T-ECL) can be tuned to more than 26 nm covering part of the ITU-T band to couple with tunable receiver [21]. The remotely fed colorless ONU is based on the remote seeding that relieves need of laser diode at optical network unit (ONU) end.

For designing an optical access network, the capital and operational costs are vitally important due to the fact of its low cost sharing characteristics. Easily manageable, simple to upgrade, customer friendly, highly reliable, and overall satisfactory performance are crucial parameters for achieving a well-designed optical access network. A detail description of network topology, standards, and hierarchy of optical access network with some latest and ongoing developments need to be examined. At present, most of the field deployed optical access networks based on the passive power splitter at the remote node to broadcast information to all optical network units [22].

It is really challenging to generate mm-wave frequencies by using electrical devices due to the limited frequency response. The more optimum solution is to generate millimeter waves by photonic means. Recently, many groups have proposed different techniques of photonic generation of mm-wave and RoF transmission systems. The photonic generation of mm-wave is mostly accomplished by direct laser modulation, external intensity modulation, and remote heterodyning.

The photonic generation methods of mm-wave are vastly investigated in literature. These methods include the technique using the external intensity modulator (ODSB, OSSB, and OCS), dual-mode laser, optical phase-locking loop (OPLL), optical injection phase-locked loop (OIPLL), four wave mixing (FWM), external phase modulation, stimulated Brillouin scattering (SBS), and harmonic generation by SOA and OFDM [23]. The most important and basic process in RoF systems is modulation technique, where the radio frequency signal applied to modulate the optical carrier. RoF modulation methods can be broadly categorized into direct and external modulation. In direct modulation, the mm-wave is directly applied to a semiconductor laser to generate an intensity modulated optical signal. It is the simplest and least expensive method and remained focus in early research. However, the relaxation

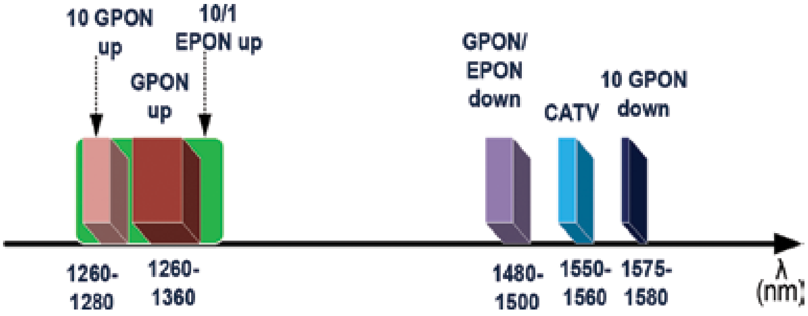

Figure 2. Wavelength allocation by ITU-T and IEEE for GPON/EPON.

oscillation limits achievable modulation bandwidth and results in high intensity noise. While on the contrary, devices such as intensity modulator, phase modulator, and interferometer can be used to modulate the phase of the optical carrier. External modulation is preferred than the direct modulation due to it is better resilience against chromatic dispersion at high speeds. Therefore, external modulation is mostly preferred for higher speeds or when the light cannot be directly modulated. Advance modulation techniques to achieve high data rates and higher mm-wave frequencies are also introduced based on OFDM and semiconductor optical amplifier (SOA). Multiband techniques are also described to achieve multiuser communications.

To fully utilize the potential of mm-wave RoF systems, its performance and reliability should be improved and considerably reduced the cost. This can be accomplished by large-scale photonic integrated circuits (PICs) [24]. PICs can enable integration of several components, such as lasers, couplers, modulators, and detectors on the same chip, reducing optical losses. But to develop PICs require very advanced design and processing techniques. Research is underway all around the world to develop them.

4. Radio over fiber systems

The wireless technology has survived as an essential telecommunication mean with time since its origination in the late 19th century. After the remarkable innovation of mobile or cellular phone, this technology has outnumbered the wired technologies in telecommunication field. Even now, there is more than 100% density of cell phones in the world. Telecommunication industry is at the epoch of a new revolution where high-speed digital signal processing (DSP) is being applied to replace most of the analog circuitry used to modulate and demodulate the radio and optical waves. After this excogitation, many new, lucrative, and adaptive solutions appeared that have not only improved the efficiency of wireless communication channels but also make possible coordinated multipoint (CoMP) transmission [25].

The RoF is used as backbone technology for wireless access networks and makes it possible to combine the RF signal processing utilities in one common area (central office). The optical fiber is used to distribute the RF signals to the remote antenna units for low signal loss (0.2 dB/km at 1550 nm wavelength) [26]. A fiber-fed distributed antenna network can be implemented for microcellular network. The remote antenna units are connected with central office through analog optical fiber links. All the de-multiplexing and signal processing is done at central office in this setup [27]. Therefore, each remote antenna site just contains an optical transmitter, an amplifier and the antenna unit, which significantly reduces the cost of the microcellular antenna sites. The spectral efficiency of radio network can be improved by distributed antenna system with the liberty of adaptive antenna selection and adaptively assigning the channels. The major advantage of RoF configuration is the reduction of the signal losses by employing the low loss optical fibers for signal propagation from central office to remote antenna units. Moreover, this scheme provides the system protection against electrical discharges and lightning strikes.

In the generic radio over fiber architectures, the performance gains of optical fiber and radio technologies are combined to offer an alternate system for broadband wireless access as shown in **Figure 3**. In a typical RoF system, a large number of remote antenna base stations are connected with a central office (CO) through an optical feeder fiber network where all the switching and signal processing devices can be located for centralized control and monitoring. The wireless links for access networks in the last mile segment of the data transport are offering mobility, flexibility, and high capacity links to the end user. Moreover, in cellular based access networks a certain geographical area is covered by a number of base stations (BS) in the form of cluster of cells. In the next generation of cellular networks, the reach of the wireless link will be short to achieve a substantial increase in data rates. It will need higher RF carriers and advance modulation formats to attain high capacity links. To offer adequate coverage and support multi input multi output (MIMO) system, the number of antenna units per geographical area will be increased that will need rigorous control on large number of distributed nodes. The transport of aggregated data from/to a central office (Co) will need a high capacity backhaul optical fiber network for high density of antenna units [28].

In radio over fiber (RoF) systems, the radio signal modulation can be achieved by two alternate methods either to perform the baseband to RF up or down conversion at the remote BS. It will result digital transport of the information through the fiber backhaul or using optical fiber for the analog transport of wireless signals transparently [9]. On the basis of the applications,

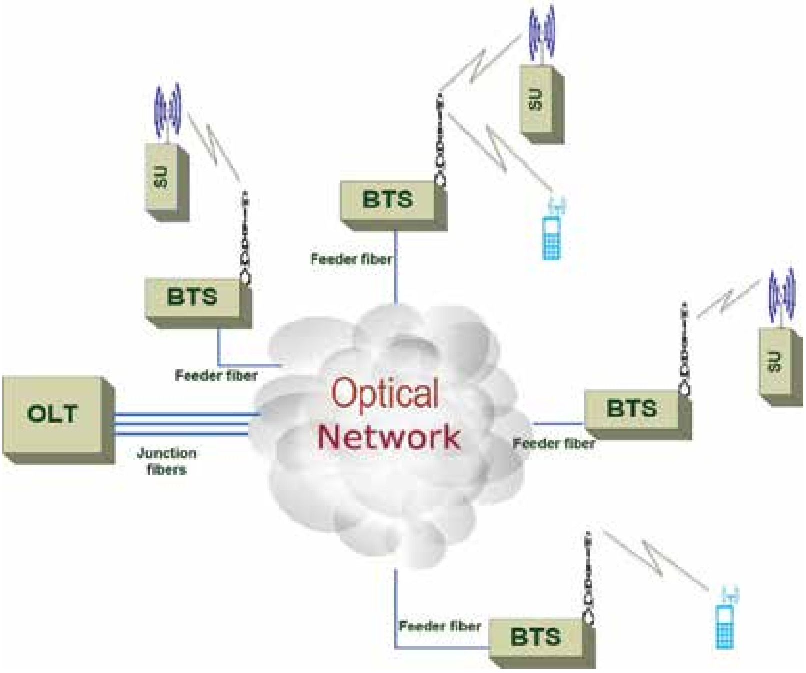

Figure 3. Radio over fiber system architecture. SU: Subsriber unit, BTS: Base transceiver station.

the fiber feeder network can be used as active or passive optical network. In general, passive feeder network is applied for the RoF systems and all the active devices are either located at the CO or at the BSs. However, if the RoF system is applied as a metro network, the feeder network will contain multiple active devices in this infrastructure.

The centralized network arrangement is the best optimum solution for RoF systems that allows securing the sensitive and delicate equipment at one location and shares them among a larger numbers of end users. Furthermore, the centralized control enables dynamic and reconfigurable channel assignment to base stations that improves the performance of network quite considerably [12]. The dynamic channel assignment techniques allow assigning multiple frequency channels to a particular cell of base station that is heavily loaded with users to avoid the blocking probability from insufficient frequency capacity [21]. The performance of the transport layer is very crucial for the performance of radio over fiber access network. RoF can also be employed to simplify the overall access network architecture and reduce operating costs in some situations. Intensity modulation with direct detection (IM-DD) is the simplest technology for the transport layer in RoF links [25]. To accomplish this, the analog radio signal is directly modulated by the optical intensity of a laser and an analog receiver performs direct detection.

By applying hybrid TWDM technology, the capacity of the RoF systems can be enhanced appreciably for optic feeder networks. In this way, a large number of RoF channels can be carried by each wavelength from the base stations to the central office and vice versa through a single fiber that also provides quantum increase in network capacity without the need for laying new fiber [17].

To develop and implement a simple, compact, low-cost, and light-weight remote antenna base station, the integration of optics and optoelectronic components will be essential. The base stations with such architectures can decrease per customer cost and speed up the deployment of the RoF systems. There are many system design are proposed by different research groups and institutions to achieve this goal as fiber-wireless (FiWi), wireless optical broadband access network (WOBAN), metro-access ring integrated network (MARIN), grid-based reconfigurable optical-wireless network (GROW-Net), fiber optic networks for distributed, extendible heterogeneous radio architectures and service provisioning (FUTON), and a converged copper-optical-radio OFDMA based access network with high capacity and flexibility (ACCORDANCE).

4.1. Pragmatic design approaches for applying RoF systems

The radio over fiber (RoF) is not merely a transport technique for wireless signals over optical fibers but it involves photonic generation of radio waves and integration of radio-optics technologies. To promote and enhance the quality of wireless broadband services, seamless networking capabilities for optical and wireless domains need to be further explored. The first barrier to overcome in this direction is the integration of medium access control (MAC) protocols for both segments. The seamless propagation can only be achieved by resolving the layer-1 issues such as propagation delay, noise, and interference on converged medium of fiber and radio. The sub-layers logical link control (LLC), and dynamic bandwidth allocation

(DBA) within data link layer are responsible for adaptively managing the diverse traffic types over common media through coordination with medium access control (MAC) strategy of error control [25].

In converged RoF systems for applying TDMA technique in upstream, a downstream authorization message sent to a specific ONU to assign bandwidth share. The ONUs communicates with the OLT to get permission to send their data by sending a report message of current buffer status. Whereas, in the wireless segment of this converged system, carrier sense multiple accesses with collision avoidance (CSMA/CA) under 802.11 protocol suites is adopted technique. The CSMA/CA works well for converged system due to the restricted coverage area for wireless due to propagation losses in atmosphere. The integration of radio and fiber technologies to achieve converged RoF system is not straightforward. Most of the studies on converged RoF systems perceive the optical domain just as reach extension of radio signals from main switching unit to base stations or remote antenna units (RAUs). In P2MP techniques for applying RoF, the MAC only works well if propagation delay of optical fibers was not considered. In 802.16e, the maximum allowable delay spread is 300 ns for multipath interference that impose an upper limit on remote antenna spacing and overlapping coverage so that tolerance for inter symbol interference (ISI) remained in limits [29]. To overcome MAC restrictions of RoF systems, a protocol translation strategy is proposed by some research groups to meet optical-wireless borderline. This technique is known as radio and fiber (R&F) that achieved some further integration in contrary to RoF. However, it is still noncomprehensive and caused extra overhead and complexity. Recently, a third technique is proposed to apply integrated technologies for sharing the common resources between the two parts of RoF systems.

The evolution of new mm-wave technology that is capable to offer multi-gigabit signal propagations over a radio frequency channel. The latest progress in 60 GHz radio over fiber systems has made it one of the promising solutions for the multi-gigabit mm-wave wireless access networks. The Federal communications commission (FCC) in United States allocated 7 GHz of continuous spectrum 57–64 GHz for license free operation [30]. The huge free bandwidth of 7 GHz has pulled the attentions of researchers around the world. It is considered as a solution to offer multi Gbit/s wireless access for communication systems with high security and anti-interference ability [31], especially due to congestion in the lower frequency bands.

The actualization of multi-Gbit/s wireless access network at 60 GHz band comes across number of technical challenges. It suffers high air-link loss and quite low power efficiency and device performance compared to lower frequency bands (i.e. path-loss at 60 GHz is about 30 dB higher than at 2.4 GHz). The 60 GHz band undergoes 15–30 dB/km atmospheric absorption loss based on atmospheric conditions of the area [28]. The coverage area is less than 10 m for a cell at 60 GHz that needs large number of antenna units along with high-capacity feeder network to provide wireless coverage [9]. The 60 GHz signal propagation in atmosphere is estimated by Friis transmission equation. It is not possible to realize ubiquitous wireless service coverage as WiMAX and LTE with 60 GHz band [10]. Therefore, 60 GHz band can only be implemented in cost effective and practical mode as non-line-of-sight (NLOS) transmission at indoor environment. This requires inexpensive and flexible base station management at brown areas [31].

On the other hand, the mm-wave (especially 60 GHz band) radio technology can easily approach multi-gigabit capacity. It is readily apparent that multi Gbit/s data rates can be achieved by emerging high capacity mm-wave radio links with high bandwidth and small coverage distance [32]. The key consequence of this fact is that the small pico or microcells with multiple access points are required to cover a particular area (home or office) with mm-wave system. Therefore, the radio home networks will be like a multi cellular network. In this context, an integration is required to achieve the potential offered by mm-wave with the optical infrastructure to link the different remote antennas to provide a inexpensive and adjustable solution. The coordinated research efforts are required for the development and improvement of millimeter pico-cellular personal access networks at low cost in the presence of many performance constraints.

Telecom regulatory authorities have announced this band license free world wide to attract researchers, telecom operators and telecom vendors to develop systems for this band. Many groups are formed to standardize the unlicensed mm-wave band to utilize its potential as a RF carrier band for wireless access networks. The IEEE 802.15.3c-2009 was published on September 11, 2009 to attain this goal. However, the first economical and pragmatic systems for this band were marketed conforming to the IEEE 802.11ad.

4.2. Millimeter wave applications

Many indoor applications at 60 GHz band are proposed [33].

1. Uncompressed high definition (HD) video display to a remote screen wirelessly with wired equivalent "I" quality experience.
2. The gigabytes wireless file transfer.
3. Wireless personal area network that permits wireless connection with multiple peripherals like monitor, keyboard, and mouse etc. It will save the frequent need of plug and unplugs.
4. Wireless gigabit Ethernet connection that allows multi-gigabit bi-directional Ethernet traffic. This feature is very attractive for smart phones, tablets and personal digital assistants (PDAs).

Radio over Fiber (RoF) technology has attracted great interest in the last decade to offer optical transmission of radio signals to simplified base station (BS) [15].

4.3. Standardization of millimeter wave band

The great interest in 60 GHz wireless transmission has motivated the formation of many International mm-wave standardization groups and industry alliances in last few years. Unlicensed mm-waveband has been considered a possible RF carrier band for future wireless access networks. To attain this goal, the IEEE 802.15.3c task group was constituted to formulate an alternate physical layer to support mm-wave communications for the present

IEEE 802.15.3 WPAN standard [34]. In August 2006, ECMATC-48 began an effort to standardize data link and physical layer for mm-wave unlicensed band for multimedia and data applications [33]. A wireless high definition (HD) consortium was formed in October 2006, with a focus to develop a number of superior quality uncompressed multimedia applications using 60 GHz technology. In May 2009, the wireless gigabit alliance (WiGig) was created to develop a set of common specification for mm-wave band to develop a global system for interoperability of products for a diverse nature of applications. IEEE has published first mm-wave standard 802.15.3c on September 11, 2009 [18]. The IEEE 802.15.3c and IEEE 802.15.3a were proposed for wideband personal area networks. In IEEE 802.15.3c, four channel OFDM mm-waves are proposed to employ free spectrum of 57–64 GHz to achieve the data rate up to 7.3 Gbit/s [19].

4.3.1. IEEE 802.15.3c

The IEEE 802.15.3c group was formed under the supervision of the Japanese research center national institute of information and communications technology (NICT) to design a WPAN standard capable of being used at 60 GHz [14]. It is the first IEEE standard designed for multi-Gigabit/s wireless transmission to operate in the mm-wave band. This standard was published in 2009 [35]. In this standard, three physical layers are defined to meet different market segments,

Single carrier (SC) mode is based on single carrier modulations and bit rate is ranging from 25.8 Mbit/s to 5.2 Gbit/s with recommended modulation techniques are pi/2 binary phase shift keying (BPSK), Gaussian minimum shift keying (GMSK), quadrature phase shift keying (QPSK), quadrature amplitude modulation (8-QAM), 16-QAM, on off keying (OOK) and digital radio broadcast (DRB). The high speed interface (HSI) mode is based on OFDM modulations where bit rates are defined from 32.1 Mbit/s to 5.7 Gbit/s and approved modulation techniques are QPSK, 16-QAM and 64-QAM. Audio/Visual (AV) mode is based on OFDM modulations and wireless high definition (HD) specifications with physical layer throughput ranging from 952 Mbit/s to 3.807 Gbit/s and modulation formats are BPSK, QPSK, and 16-QAM.

4.3.2. ECMA-387

This Standard specifies a physical layer (PHY), distributed medium access control (MAC) sub layer, and high definition multimedia interface (HDMI) protocol adaptation layer for mm-wave networks. The ECMA-387 was adopted by ISO in June 2009. The most important feature of this standard was the channel widening by associating adjacent channels that makes it possible to support the data rates up to 25 Gbit/s.

4.3.3. Wireless gigabit alliance

The wireless gigabit alliance (WiGig or WGA) was formed in May, 2009.The purpose of this formation to brings together major telecommunication players like Intel, Wilocity, Broadcom, Atheros, and many others to work together to develop common standards for mm-wave products [34]. The first WiGig specification (Vl.O) is published in December, 2009. While, the second version introduced in 2011. The WiGig specifications are drafted to allow devices to communicate at multi-gigabit speeds without wires. The standard has recommended wireless transmission of high data rate for video and audio applications to enhance the performance of WLAN devices.

4.3.4. IEEE 802.11ad

Recently, IEEE has put in a new wireless standard 802.11ad that promises very high speed for short distance communication. The commercial products based on this standard provide 7-Gbit/s data rate over 60 GHz mm-waves. 802.11ad allows devices to exchange data over four 2.16 GHz wide channels to support data rates up to 7 Gbit/s. The IEEE standard for mm-wave was initially created in January, 2009. It was designed and developed to work at 60 GHz as a new generation of Wi-Fi systems for the IEEE 802.11 family [21]. The IEEE 802.11ad enabled chips are being installed in millions of devices. 802.11ad supports all native 802.11a/b/g/n/ac standards and enables devices to seamlessly switch between 2.4, 5, and 60 GHz bands [29]. One of the major advancements comes from the single carrier is low power consumption. It can enable advance power management and long battery life of device. For 60 GHz band, the data rate around 7 Gbit/s that makes it more attractive than the common Wi-Fi standards at 2.4 and 5 GHz. The IEEE 802.1lad standard maintains the Wi-Fi user experience at the same time with backward compatibility to the previous 802.11 systems.

This new 60 GHz Wi-Fi standard provides support to internet protocol (IP), high definition multimedia interface (HDMI), display port(a digital display interface developed by the video electronics standards association), universal serial bus (USB) and peripheral component interconnect express (PCie). Therefore, it is multi-protocol used to communicate with various peripherals including IP, audio-visual (AV), and input–output (I/0) data ports. In 802.11ad, single carrier (SC) modulation is formulated to support multi gigabit/s data rates for line of sight (LOS) short distance communication but maintaining low power consumption and low system complexity. Whereas, OFDM is adapted for high data rates for non-line of sight (NLOS) transmission but only for a maximum distance of 10 m.

5. Conclusion

The ever increasing customer demands for high capacity broadband services has ensued the development of fiber based access networks. A comprehensive overview about radio systems capable to provide multi gigabit data rate with special focus on 60 GHz millimeter wave is provided. The 60 GHz mm-wave allocated spectrum, its applications and standardization, and system approaches are also highlighted. Most of the present studies are concentrating the point-to-point fiber-wireless transmission using hetero optical suppressed carrier mm-wave systems, whereas multi-user applications such as pico or femto-cells still need exhaustive research efforts. The simulation and experimental systems need to be designed to further reduce the cost of devices conforming to optical access process introduced in the IEEE 802.11ad standard.

Author details

Shahab Ahmad Niazi

Address all correspondence to: shahabniazi@iub.edu.pk

Electronic Engineering Department, University College of Engineering and Technology,
The Islamia University of Bahawalpur, Pakistan

References

[1] Patnaik B, Sahu PK. Optimized ultra-high bit rate hybrid optical communication system design and simulation. International Journal for Light and Electron Optics. 2013;**124**:170-176. DOI: 10.1016/j.ijleo.2011.11.080

[2] Ladan S, Yari A. Evaluation of migration scenarios toward NGN considering economic aspects. In: Proceedings of the IEEE Globecom; 30 November-4 December 2008; New Orleans, LO, USA: IEEE; 2008. pp. 1-5

[3] Crow J. Regulation and free markets Redux additional insights on regulating the telecommunications industry in the new economy. Journal on Telecommunication and High Technology Law. 2006;**5**:487-500

[4] Fang Z, Zhao CZ. Recent progress in silicon photonics: A review. ISRN Optics. 2012:1-27. DOI: 10.5402/2012/428690

[5] Patnaik B, Sahu PK. Optimized hybrid optical communication system for first mile and last mile problem solution of today's optical network. Procedia Technology. 2012;**6**: 723-730. DOI: 10.1016/j.protcy.2012.10.087

[6] Ihara T, Fujumura K. Research and development trends of millimeter-wave short-range application systems. The IEICE Transaction on Communication. 1996;**79**:1741-1753

[7] Niazi SA, Zhang X, Xi L. Co-existence generation of XG-PON and single carrier XLG-PON for ultra-high definition TV transmission with entirely passive optical plant. Optoelectronics Letters. 2013;**9**:221-224. DOI: 10.1007/s11801-013-3011-9

[8] Prat J, editor. Next-Generation FTTH Passive Optical Networks Research Towards Unlimited Bandwidth Access. 1st ed. Chichester: Springer; 2008. p. 185. DOI: 10.1007/978-1-4020-8470-6

[9] Niazi SA, Zhang X, Xi L. Simultaneous generations of independent millimeter wave and 10 Gbit/s wired signal by single electrode modulator in TDM-PON network. Journal of Optical Communication. 2013;**34**:21-27. DOI: 10.1515/joc-2013-0008

[10] Chanclou P, Cui A, Geilhardt F, Nakamura H, Nesset D. Network operator requirements for the next generation of optical access networks. IEEE Network. 2012;**26**:8-14. DOI: 10.1109/MNET.2012.6172269

[11] Niazi SA, Zhang X, Xi L. A 32 wavelength hybrid passive optical network architecture by applying QPSK modulation in downstream and intensity re-modulation for upstream colorless transmission. Journal of Convergence Information Technology. 2013;**8**:201-208. DOI: 10.4156/jcit.vol8.issue3.24

[12] Woo AKC, Li CY, Wai P. Lightpath affiliation graph approach for wavelength assignment of lambda leasing service. In: Proceeding of the 14th OptoElectronics and Communications Conference (OECC 2009). DOI: 10.1109/OECC.2009.5219915

[13] Ma YR, Qian YB, Peng GK, Zhou XP, Wang XM, Yu JW, Luo YQ, Yan XJ, Effenberger F. Demonstration of A 40Gb/S time and wavelength division multiplexed passive optical network prototype system. In: Proceedings of the National Fiber Optic Engineers Conference (NFOEC 2012)

[14] Abhishek D, Bart L, Didier C, Mario P, Piet D. Wavelength switched hybrid TDMA/WDM (TWDM) PON: A flexible next-generation optical access solution. In: Proceedings of the International Conference on Transparent Optical Networks (ICTON 2012). DOI: 10.1109/ICTON.2012.6253746

[15] Niazi SA, Zhang X, Xi L. A viable passive optical network design for ultrahigh definition TV distribution. Advances in OptoElectronics. 2013;**3**. https://www.hindawi.com/journals/aoe/2013/219271/. DOI: 10.1155/2013/219271

[16] Effenberger F. XG-PON1 versus NG-PON2: Which one will win. In: Proceedings of European Conference and Exhibition on Optical Communication; 16-20 September 2012; Amsterdam, Netherlands. Optical Society of America; 2012. DOI: 1364/ECEOC.2012

[17] Niazi SA, Zhang X, Xi L. The available options for wavelength group selection and transceiver design for next generation PON stage 2 (NG-PON2). Journal of Optical Communication. 2013;**34**:223-229. DOI: 10.1515/joc-2013-0040

[18] Fan ZF, Erefteh DM. Chirp managed lasers: A new technology for 10Gbps optical transmitters. Optik & Photonik. 2007;**12**:39-34. DOI: 10.1002/opph.201190284

[19] Kani JI, Bourgart F, Cui A, Rafel A, Campbell M, Davey R, Rodrigue S.: Next-generation PON-Part I: Technology roadmap and general requirements. IEEE Communications Magazine. 2009;**47**:43-49. DOI: 10.1109/MCOM.2009.5307465

[20] Duong TN, Milion C, Genay N, Grard E, Rodrigues V, Burie J-R, Nascimento MD, Bougueroua K, Dijk FV, Charbonnier B,Masson JL, Ouzzif M, Chanclou P, Gharba A. Very high bit-rate transmission for NG-PON using AMO OFDM direct modulation of

linear laser. In: Proceedings of the Optical Fiber Communication (NFOEC- 2010). DOI: 10.1364/OFC.2010.OTuO3

[21] Raharimanitra F, Chanclou P, Murano R. 40 Gb/s NG-PON system using low electrical bandwidth tunable receiver and emitter at 10 Gb/s. In: Proceedings of the 37th European Conference on Optical Communication (ECOC-2011). DOI: 10.1364/ECOC.2011.Mo.1.C.2

[22] Wong E. Optical technologies in passive optical access networks. In: Cedric F, editor. Passive Optical Networks. 1st ed. Chichester: Academic Press, Burlington; 2007. pp. 87-149. DOI: 10.1016/B978-012373853-0.50009-1. Ch3

[23] Park CS, Lee CG, Park CS. Photonic frequency upconversion by SBS-based frequency tripling. Journal of Lightwave Technology. 2007;**25**:1711-1718. DOI: 10.1109/JLT.2007.897749

[24] Berceli T, Herczfeld PR. Microwave photonics—A historical perspective. IEEE Transactions on Microwave Theory and Techniques. 2010;**58**:2992-3000. DOI: 10.1109/TMTT.2010.2076932

[25] Kazovsky L, Shing-Wa W, Tolga A, Kadir MA, Moises RN, Shastri A. Hybrid optical–wireless access networks. Proceedings of the IEEE. 2012;**100**:1197-1225. DOI: 10.1109/JPROC.2012.2185769

[26] Singh S. Simulative analysis of the influence of continuous wave laser power on different data formats for a bi-directional radio over fiber communication system. Journal of Optics. 2012;**41**:25-31. DOI: 10.1007/s12596-012-0059-z

[27] Mohamed N. Review on system architectures for the millimeter-wave generation techniques for RoF communication link. In: Proceedings of the IEEE International RF and Microwave Conference; 2-4 December 2008; Kuala Lumpur: IEEE; 2009. pp. 326-330

[28] Daniels RC, Heath RW. 60 GHz wireless communications: Emerging requirements and design recommendations. IEEE Vehicular Technology Magazine. 2007;**2**:41-50. DOI: 10.1109/MVT.2008.915320

[29] Zhang Y, Liu B, JS. Generation of multiple-frequency optical millimeter-wave signal with optical carrier suppression and no optical filter. IEEE Photonics Journal. **2017**(9): 1-7. DOI: 10.1109/JPHOT.2016.2647200

[30] Bujang S, Jaafar S, Amiruddin MF, Ariffin A, Lee YC. A V-band radio receiver integrating LTCC Sop module with a fully embedded LPF for wireless applications. In: Proceedings of the 17th Asia Pacific Conference on Communications; 2-5 October 2011; Sabah (Malaysia): IEEE; 2012. pp. 770-773. DOI: 10.1109/APCC.2011.6152911

[31] Xu K, Sun XQ, Yin J, Huang H, Wu J, Hong X, Lin J. Enabling ROF technologies and integration architectures for in-building optical–wireless access networks. IEEE Photonics Journal. 2010;**2**:102-112. DOI: 10.1109/JPHOT.2010.2043665

[32] Charbonnier B, Bras HL, Urvoas P, N'Guyen QT, Huchard M, Pizzinat A. Upcoming perspectives and future challenges for RoF. In: Proceedings of the Microwave Photonics, International Topical Meeting on; 3-5 October 2007; Victoria, BC, Canada: IEEE; 2007. pp. 21-23

[33] Yong SU. Introduction to 60 GHz. In: Yong SU, Xia PF, Garcia AV, editors. 60 GHz Technology for Gbps WLAN and WPAN from Theory to Practice. 1st ed. Chichester: Wiley; 2010. pp. 1-16. DOI: 10.1002/9780470972946. Ch1

[34] Azza MA, Yahyaoui ME, Moussati AE. Adaptive modulation and coding for the IEEE 802.15.3c high speed interface physical layer mode. In: Oualkadi A, Choubani F, Moussati A, editors. Proceedings of the Mediterranean Conference on Information & Communication Technologies 2015. Lecture Notes in Electrical Engineering; Chichester: Springer; 2015. pp. 65-73. DOI: 10.1007/978-3-319-30301-7

[35] Guillory J. Radio over Fiber (RoF) for the future home area networks [thesis]. Dept. ESYCOM Laboratory and Orange Labs, Paris-Est University; 2012

Chapter 6

RF Desensitization in Wireless Devices

Chulsoon Hwang

Additional information is available at the end of the chapter

http://dx.doi.org/10.5772/intechopen.76162

Abstract

The Internet of Things (IoT), where data are exchanged via wireless connection between devices, is rapidly becoming inextricable from our daily lives. A variety of IoT devices ranging from smart homes to autonomous vehicles and health care have grown explosively. While wireless communication makes the devices conveniently connected, it also makes them inherently vulnerable to electromagnetic interference (EMI). Any radio frequency (RF) antenna used as a radio receiver can easily pick up the unintended electromagnetic noise from integrated circuits (ICs) populated within the same device. The radio range is limited by interference, called RF desensitization, which in turn often limits the usefulness of IoT devices. While the amount of EMI can be estimated using numerical simulations tools like HFSS and CST, engineering issues such as where to place the IC or setting the radiation specification of the IC cannot be so easily addressed. In this chapter, an insightful and efficient RF desensitization model necessary to estimate EMI levels on RF antennas will be addressed. The approach will be focused on two representative areas: noise radiation source modeling and coupling estimation associated with an embedded RF antenna.

Keywords: radio frequency, desensitization, electromagnetic interference, wireless devices, dipole moment, reciprocity

1. Introduction

Electromagnetic interference (EMI) is the disruption of operation of an electronic device when it is in the vicinity of an electromagnetic field in the radio frequency (RF) spectrum caused by another electronic device. Any electronic device generates electromagnetic energy, usually over a wide band of frequencies [1]. These emissions can interfere with the performance of sensitive wireless receivers nearby, called RF desensitization. In general, as contribution of thermal noise is much lower than that of electromagnetic noise in EMI, only electromagnetic noise is considered. When the noise sources and receivers are situated within the same device or system in which the interference tends to be much more severe than typical EMI. For instance, the noise picked up by AM or FM radio is often a major source of user complaints in the automotive industry. Recently, two popular electric cars, the BMW i3 and Tesla Model X, have excluded terrestrial AM radio because electromagnetic noise from the electric motor interferes with the broadcast reception [2]. The study and analysis of EMI in electronic systems is not a new topic, it has been studied for several decades; but RF desensitization has received renewed interest in recent years as more electronic applications move to wireless communication platforms represented by the Internet of Things (IoT). In recent IoT devices, the noise-sensitive RF antennas are combined with noisy digital integrated circuits (ICs) so the radio range is often limited by the RF desensitization. For instance, the RF module in smart phones composed of an RF antenna, and its receiver can detect signals as weak as −120 dBm in a 200 KHz bandwidth, if not disturbed by nearby electronics. However, the clock frequencies of a smart phone can reach GSM 880–1800 MHz, as well as Bluetooth and Wi-Fi bands [3]. This limits the receiver's ability to detect low-level signals, thus, reducing the overall range and data rate. The radio range limitation of mobile devices often causes great inconvenience to countless consumers. **Figure 1** depicts the typical scenario of a communication system with the receiver's sensitivity affected by electromagnetic noise from in-device components.

A typical industry's product design development cycle starts by defining the product specification and then begins the research and development process. A prototype is populated, debugged, and tested. Based on company protocol, one version of it (prototype, beta, or final product) is tested, and then mitigated and retested—most often many times over—in order to achieve the specification. Any RF desensitization problems that come up late in the design process may be impossible to fix and adding redundant shielding structures entails increased product costs. However, most studies have been focused on understanding the particular EMI problems in a developed system and developing effective numerical simulation methods. In

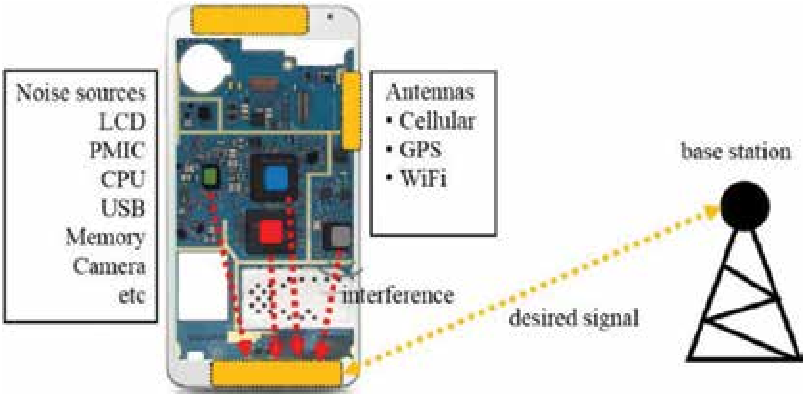

Figure 1. Typical RF desensitization mechanism in wireless devices.

addition, the analysis and understanding have been based on their particular physical structures without a universal model to explain the radiation and coupling physics. As IoT devices become increasingly integrated and cost-sensitive, it is essential to have an efficient and fast way to understand the problem not only to mitigate the noise coupling but also to estimate the RF desensitization early in the design cycle, well before a design is fully finished. For this reason, the model should be highly simplified and fast as an early estimation, while also containing physical insight. At the same time, it should not require detailed information such as circuits and physical structures of the noise source, which are the most likely not available in the development stage. This chapter addresses an efficient RF desensitization model to understand the physics of interference within a device, which can also be used as a tool for efficient product design.

2. RF desensitization model

2.1. Noise source model

In contrast to conventional EMI problems where electrically large EMI antenna structures typically exist, ICs have been identified as a major noise source in wireless devices for receiver sensitivity degradation. Today's use of multilayer PCBs allows the designer to move the potential radiation-critical traces on the quasi-shielded inner layers and uses stripline technology to minimize the emission. As a result, especially at higher frequencies, the ICs situated in outer layers start to dominate the electromagnetic emission. The inclusion of ICs as the EMI antenna changes the nature of the problem. Recently, highly developed products, multiple ICs from different suppliers are integrated, and only the circuit/layout related to input/output (IO) are shared outside the IC supplier. As internal circuits are their intellectual properties, it is not allowed to peek into internal circuits of ICs for any reasons. Despite its physical insight, identifying the EMI antenna structure and tracing down the current path are not often feasible for the ICs as it entails knowing proprietary information of the IC itself. Thus, the noise source models to be developed should never use proprietary information or layout of ICs, but yet need to generate the same fields.

Thevenin or Norton source models are fundamental approaches for noise source modeling; the electromagnetic emissions from traces can be modeled by equivalent lumped source/impedance at the end of the traces. With the nature of highly developed electronic products, including all geometry with each dedicated source is not only too computationally intensive, but also entails knowing intellectual property of the IC suppliers. To conceal the detailed structure of noise source, multiple methods have been proposed including multipole expansion, neural networks, and modal expansion. Recently, for the simplicity and rapidity of the modeling and simulation, an equivalent dipole moment method has been investigated [4–6]. Any wire carrying current on it can be represented as an infinitesimal antenna structure known as a Hertzian dipole, or simply called a dipole moment source. ICs are then substituted by a set of magnetic and/or electric dipole moments disposed in the XY-plane which radiates the same electromagnetic field as the original source as shown in **Figure 2**. The

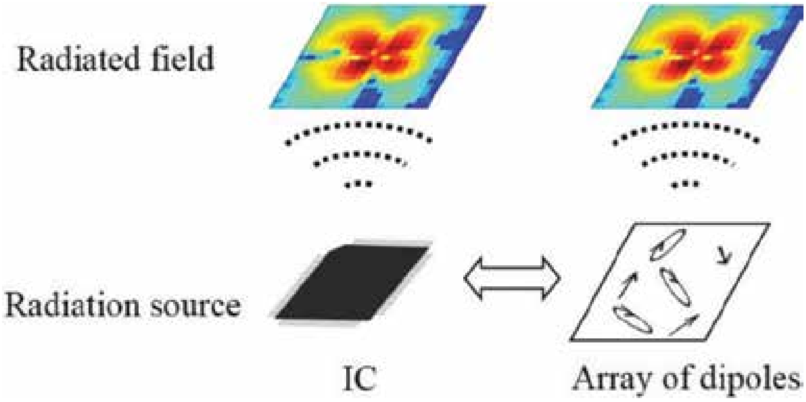

Figure 2. Equivalent radiation model based on a set of Hertzian dipoles.

radiation at a certain observation point of the space is an addition of the emissions of all the sets of dipole moments. The dipole moment source model is versatile as it contains radiation physics, at the same time it does not require knowing any internal circuit geometry. The validity of the dipole moment source model to be used for RF desensitization was experimentally proven by using a practical cell phone [7, 8]. A transfer function between the dipole moment source and RF antenna was experimentally measured and used to represent the EMI coupling to the RF antenna. The transfer function was experimentally measured in [8]. A model to theoretically explain the coupling mechanism and transfer function is addressed in the next subchapter.

The dipole moment source model needs to be reconstructed from measurements as numerical simulations or analytical methods using IC information that is not often available as mentioned before. There are two approaches: using TEM cell with known transfer function and using near-field scanning. Once the fields guided by the TEM cell with dipole moment excitation are known, the dipole moment source can be reconstructed from a dual port TEM cell or GTEM cell measurement. However, as it requires a dedicated board that fits into the opening area of the TEM cells, which is inefficient in terms of costs and time, the near-field scanning method has become the most popular method in industry. In order to reconstruct the dipole moment source from the measured near-field data, the inverse problem needs to be solved. First, electric and magnetic dipoles are assumed as infinitesimal linear wires (straight and circular, respectively) with very small ($l \ll \lambda$), very thin ($a \ll \lambda$), and assuming constant current against the spatial variation. Three types of dipoles (Pz, Mx, and My) are to be considered as the rest of them (Px, Py, and Mz) do not practically radiate by existence of the ground plane and image theory. Then, the fields radiated by the current element can be calculated from the two-step procedure; it is required to determine first A and F, a magnetic vector potential and electric vector potential, respectively, and then find the electric and magnetic fields. The vector potentials from current element and electromagnetic fields from the vector potentials from the Maxwell's equations are given as:

$$\vec{A} = \hat{z}\frac{\mu}{4\pi}\frac{e^{-j\beta R}}{R}P_z \Delta l \; \vec{F} = \hat{x}\frac{\varepsilon}{4\pi}\frac{e^{-j\beta R}}{R}M_x \Delta l + \hat{y}\frac{\varepsilon}{4\pi}\frac{e^{-j\beta R}}{R}M_y \Delta l, \tag{1}$$

$$H_A = \frac{1}{\mu}\nabla \times A \;\; E_A = -j\omega A - j\frac{1}{\omega\mu\varepsilon}\nabla(\nabla \cdot A), \tag{2}$$

$$E_F = -\frac{1}{\varepsilon}\nabla \times F \;\; H_F = -j\omega F - \frac{j}{\omega\mu\varepsilon}\nabla(\nabla \cdot F). \tag{3}$$

As the electric and magnetic fields have a linear relationship with each dipole moment, the dipole moment source can then be reconstructed from the radiated electromagnetic field by solving the linear inverse problem. Near-field scanning is often performed on a plane above the noise and source as shown in **Figure 3**.

The relationship between the dipole moment sources and the radiated fields can be represented as shown below.

$$F_n = T_{nk} X_k \tag{4}$$

$$\begin{gathered} F_n = \begin{pmatrix} [E_x]_{M^2\times 1} \\ [E_y]_{M^2\times 1} \\ [H_x]_{M^2\times 1} \\ [H_y]_{M^2\times 1} \end{pmatrix} = \begin{bmatrix} f_1 \\ f_2 \\ \vdots \\ f_n \end{bmatrix} \; T_{nk} = \begin{pmatrix} T_{ExPz} & T_{ExMx} & T_{ExMy} \\ T_{EyPz} & T_{EyMx} & T_{EyMy} \\ T_{HxPz} & T_{HxMx} & T_{HxMy} \\ T_{HyPz} & T_{HyMx} & T_{HyMy} \end{pmatrix} \\ = \begin{bmatrix} T_{11} & T_{12} & \cdots & T_{1k} \\ T_{21} & & & \vdots \\ \vdots & & \ddots & \\ T_{n1} & \cdots & & T_{nk} \end{bmatrix} \; X_k = \begin{pmatrix} [P_z]_{N^2\times 1} \\ [M_x]_{N^2\times 1} \\ [M_y]_{N^2\times 1} \end{pmatrix} = \begin{bmatrix} x_1 \\ x_2 \\ \vdots \\ x_k \end{bmatrix} \end{gathered} \tag{5}$$

where $[E_x]$, $[E_y]$, $[H_x]$, and $[H_y]$ are the known x and y components of the electric and magnetic fields obtained from near-field measurement; $[P_z]$, $[M_x]$ and $[M_y]$ are the unknown electric and magnetic dipoles in the dipole array; and, $[T]$ is a known field generation matrix whose expression can be found from Eqs. (1)–(3). The least square method can then be used to reconstruct the dipole moment source as shown below.

$$E(X) = \|T_{nk} X_k - F_n\|^2 = \sum_{i=1}^{n}\left(\sum_{j=1}^{k} T_{nj} X_j - F_i\right)^2 \tag{6}$$

$$\hat{X}_k = [T^*_{nk} T_{nk}]^{-1} T^*_{nk} F_n \tag{7}$$

where T^*_{nk}, conjugate transpose of T_{nk}.

However, because of the nature of inverse problem inherent from mathematical procedure, the solution is very sensitive to noise and is not unique because of the ill-posed transformation matrix relating equivalent sources and the measured near-field data while the noise in the near field scanning measurement is inevitable. In addition, the solution is mathematically drawn so it is not able to capture the radiation physics. Although a non-physical solution can match the

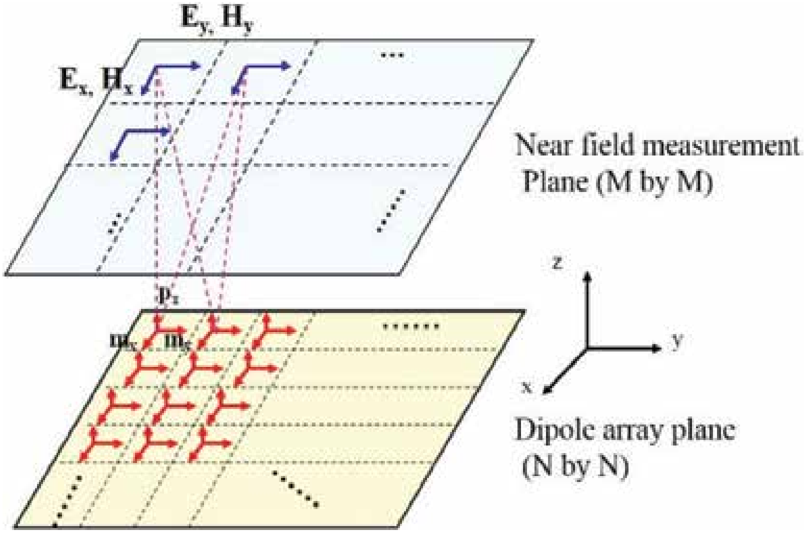

Figure 3. Source reconstruction using near field scanning.

field well at the scanning plane, it often fails to predict the fields well at other locations. In order to overcome the limitation, either a regularization method to minimize the energy of the source or various optimization methods have been investigated. The regularization method has essentially the same inherent problem, and the performance of the optimization algorithms heavily depends on the initial values users provide. Therefore, a more reliable method is needed to reconstruct equivalent dipole moments accurately with physical meaning. In [8], the least square method was used, but the dipole type and location was predetermined based on understanding of the near-field radiation pattern. Then, the least square method was used only to determine the magnitude and phase, rather than all information such as dipole moment types and orientation and, more importantly, the number of dipole moments and their location.

An example of the dipole moment source reconstruction in a practical cellphone based on the understanding of radiation physics, and the near-field radiation pattern is described in details. The structure carrying the high-speed MIPI DSI clock signals is a conductor-backed coplanar waveguide with differential signaling. It has a two layer stack-up; the top layer is ground plane and the bottom layer has four traces: ground, clock+, clock-, ground. **Figure 4** shows the top and bottom side on the edge of the FPCB. The clock lane on the FPCB is routed all the way to the input pins of the DDI chip. There are no significant geometry changes on the bottom side of the FPCB; however, the top of the FPCB has a clear discontinuity. The top of the FPCB has a solid metal and acts as the ground plane, but there is no ground at the edge of the FPCB. The surface current increases at the edge of the top ground plane, which does not come from a conduction path since there is no metal in direct contact with the edge of the top ground plane. Therefore, the only way to generate the increase of the conduction current is from a displacement current path. A simplified illustration of common mode current flow is shown in **Figure 5**. The top view of the current flow shows that there are two current loops facing opposite directions. These two equivalent *Mz* dipole moments with an equal magnitude, but opposite direction will cancel each other out. The diagram on the right side shows

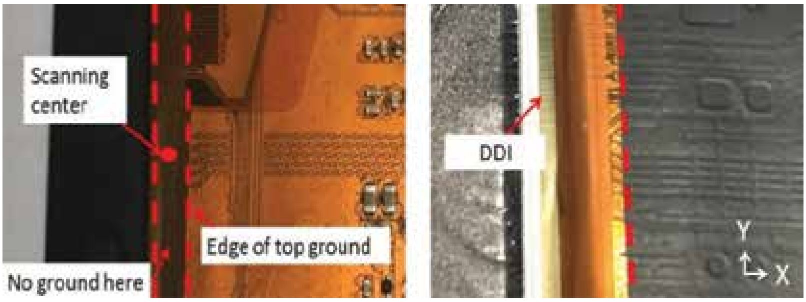

Figure 4. Top and bottom side of flexible PCB in an LCD panel.

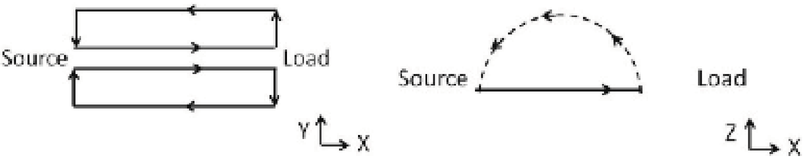

Figure 5. Illustration of common mode current flow in a differential clock pair.

the side view of the common mode current flow. The conduction current and the displacement current form a current loop in the *xz* plane. A current loop facing the *y* axis forms an *My* dipole moment, so the radiation source can be modeled as an *My* dipole moment.

In order to reconstruct the radiation source, the near-field above the LCD and FPCB was measured at 897.0 MHz. To obtain the phase resolved H-field data in the near-field, the tuned receiver mode of the VNA was used. In tuned receiver mode, both of the two ports of the VNA are receivers. Two H-field probes were connected to the two receiver ports of the VNA and the H-field probes were calibrated to get the probe factor which included the magnitude and phase information of the probe and the connecting cables and amplifiers. The cell phone controlled the LCD panel in the ON state during the whole near-field measurement to ensure the clock lane was active. The scanning height was 1 mm above the FPCB. The reference probe was placed near the noise source so that the reference signal had enough signal-to-noise ratio (SNR).

The measured H-field pattern at 897.0 MHz is shown in **Figure 6**. For all of the field patterns, the center of field pattern plot lies in the physical center of the scanning plane. This indicates that the noise source came from the clock lane because the scanning center was located exactly above it. A magnetic dipole moment along the *y* axis is denoted as M_y. The magnitude and phase of the equivalent dipole moment M_y can be easily obtained using the least square method as given in Eqs. (6) and (7). The H-field patterns from reconstructed dipole moment source are shown and the magnitude and phase from the reconstructed M_y dipole moment agree well with the magnitude and phase of the measured H-field patterns from the cell phone.

By containing physics prior to the source reconstruction, the reconstructed dipole moments were able to represent the radiation physics. However, the location and types of dipole

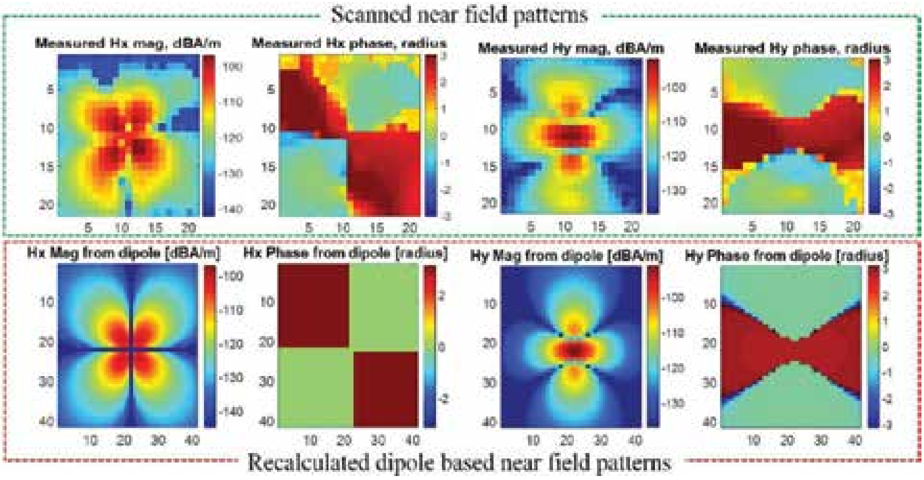

Figure 6. Comparison between scanned near-field patterns and calculated near-field patterns from reconstructed dipole moment source.

moment were determined from the researcher's educated guess based on understanding of dipole moment radiation, which is not suitable to disseminate the developed methodology to industry. The near-field pattern of each dipole moment is shown in **Figure 7**. It requires understanding of dipole moment radiation to recognize the location and type of dipole moment from the radiation patterns; sometimes it is not even possible, especially when multiple dipole moments exist. For this case, the physical dipole can be reconstructed based on the radiation pattern recognition, and the recognition can be automated by artificial intelligence based on machine learning algorithm [9].

2.2. Coupling model

As the radiation from an IC is independent of the environment nearby (this is usually the case except for the special cases such as IC noise modulation studied in [10]), the noise coupling

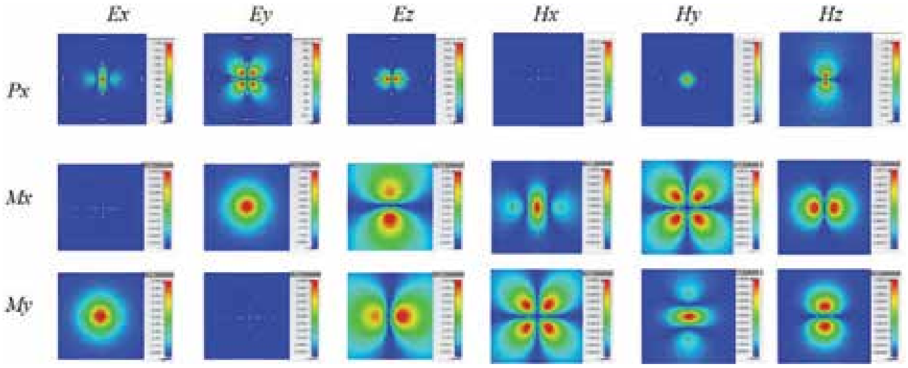

Figure 7. Near field pattern of each dipole moment.

canvbe decomposed into two parts: radiation and coupling. While conventional studies have focused on the analysis of radiation physics for debugging, recently, understanding of the coupling mechanism and its modeling have received more attention for EMI-aware design. For the coupling modeling, the Friis transmission equation could be used, but it only works for the far-field region. Since coupling problems occurring in electronic devices are strongly relevant to near-field, estimating the coupling by the Friis equation may cause the wrong results. Instead, the coupling decomposition method based on reciprocity with Huygens' box is a fundamental approach to decompose the noise coupling. It models the noise source and coupling independently, then combines them using the Lorentz reciprocity theorem, which allows separate investigations on each part. However, using Huygens' box blurs the physical meaning of the noise source so it fails to provide physical insight for the design. In this section, an efficient coupling model using dipole moment source and reciprocity will be introduced; this method can contain radiation physics and, thereby, provide an efficient tool for analysis and design for RF desensitization.

The reciprocity theorem states that when places of voltage and current sources in any reciprocal network are interchanged, the amount or magnitude of current and voltage flowing in the circuit remains the same, as depicted in **Figure 8**. In other words, Z_{21} is identical to Z_{12} in reciprocal networks.

This theorem also applies to electromagnetics. When two sources ($\vec{J}_1$, $\vec{M}_1$) and ($\vec{J}_2$, $\vec{M}_2$) exist in the same region, electromagnetic fields by reaction theory ($\vec{E}_1$, $\vec{H}_1$) and ($\vec{E}_2$, $\vec{H}_2$) must satisfy the Lorentz reciprocity theorem, whose simplified integral form is:

$$\iiint_V \left(\vec{E}_1 \cdot \vec{J}_2 - \vec{H}_1 \cdot \vec{M}_2\right) dv = \iiint_V \left(\vec{E}_2 \cdot \vec{J}_1 - \vec{H}_2 \cdot \vec{M}_1\right) dv. \tag{8}$$

When three current density or electromagnetic fields are known, the rest can be calculated from the abovementioned equation, which leads to the core idea for this approach. For instance, if one source, ($\vec{J}_1$, $\vec{M}_1$) and both electromagnetic fields on two locations, ($\vec{E}_1$, $\vec{H}_1$) and ($\vec{E}_2$, $\vec{H}_2$), are known, the rest, ($\vec{J}_2$, $\vec{M}_2$), can be calculated analytically.

Using Eq. (8), the original noise coupling problem from **Figure 9** can be decomposed into two parts, the forward problem and the reverse problem (from **Figure 10**). The currents $\vec{J}_s^{fwd}$, $\vec{M}_s^{fwd}$ describe the noise source in the forward problem, where the victim antenna is terminated. In the reverse problem, the noise source is removed and the victim antenna radiates. $\vec{J}_a^{rev}$, $\vec{M}_a^{rev}$ are currents on the victim antenna and the corresponding fields on the location of the original noise source are denoted as $\vec{E}_s^{rev}$, $\vec{H}_s^{rev}$. Then, Eq. (8) can be rewritten as:

$$\iiint_V \left(\vec{J}_s^{fwd} \cdot \vec{E}_s^{rev} - \vec{M}_s^{fwd} \cdot \vec{H}_s^{rev}\right) dv = \iiint_V \left(\vec{J}_a^{rev} \cdot \vec{E}_a^{fwd} - \vec{M}_a^{rev} \cdot \vec{H}_a^{fwd}\right) dv. \tag{9}$$

The subscript "s" and "a" represent the source and antenna, respectively (**Figures 9–11**).

As the electric and magnetic dipole moments (denoted as *P* and *M*) are essentially identical to the volume integral of electric and magnetic current density (*J* and *M*), respectively, derivation from the Lorentz reciprocity theorem can be simplified to a simple and straightforward form. The

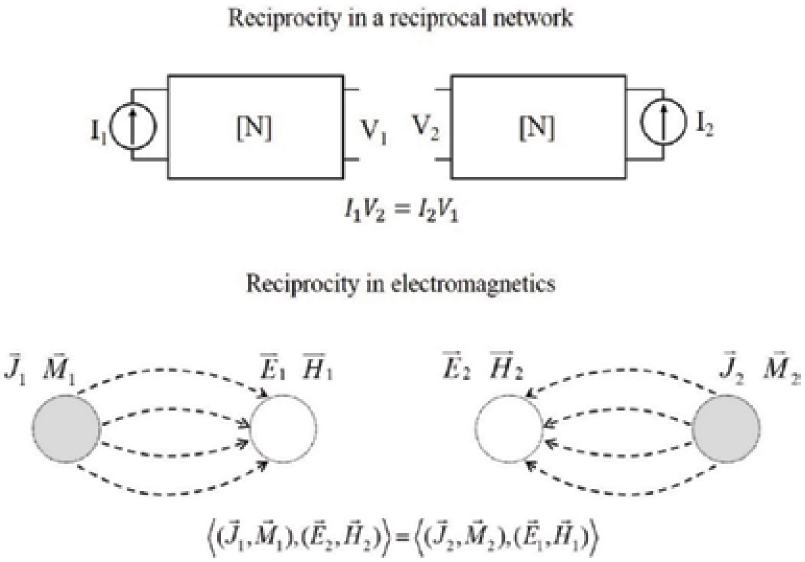

Figure 8. Reciprocity theorem.

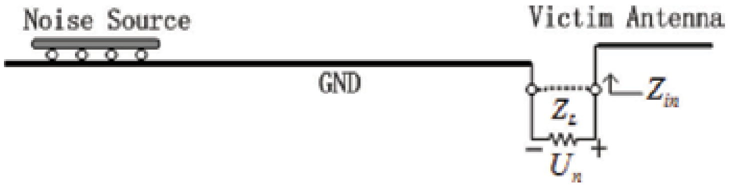

Figure 9. Original RF desensitization problem.

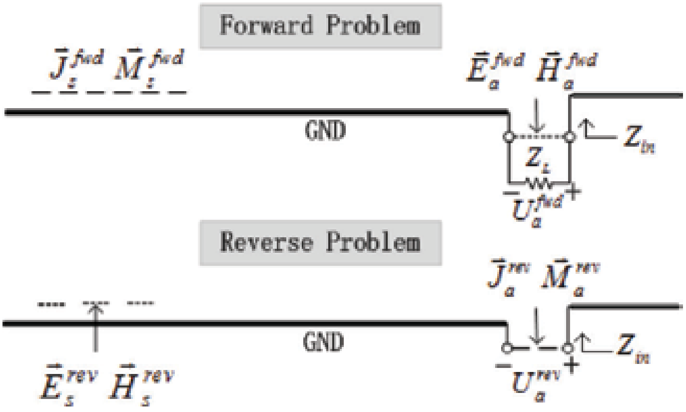

Figure 10. Decomposed problem; forward and reverse problem.

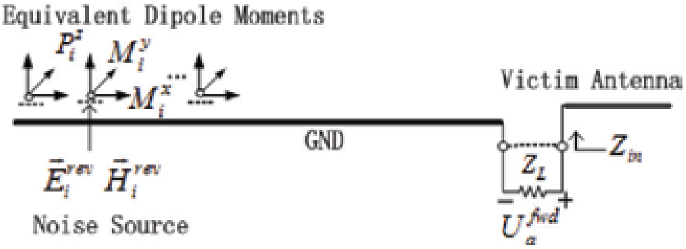

Figure 11. Equivalent RF desensitization model using dipole moments and reciprocity.

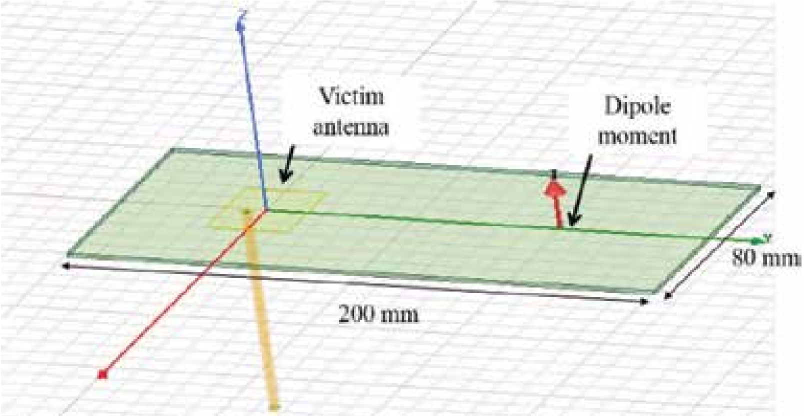

Figure 12. Model for the numerical validation; a single P_z excitation is shown as an example.

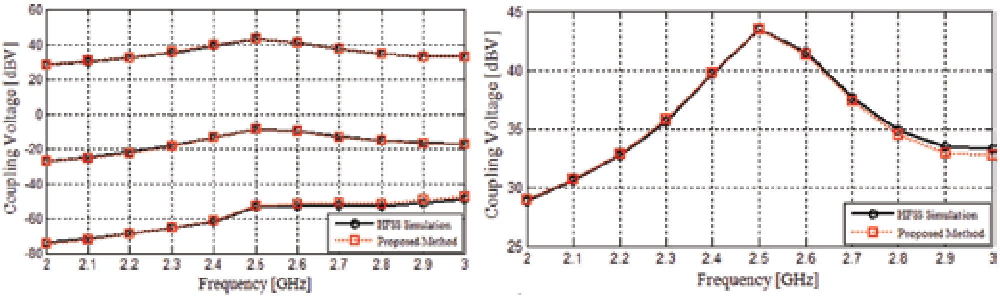

Figure 13. Numerical validation with a single dipole moment (left) and a combination of three kinds of dipoles (right).

left side of the Lorentz reciprocity theorem states the relationship between the fields generated by the victim antenna and the current density represent the IC. As the fields can be assumed as constant across the current density area, the left side of the equation can be simplified as:

$$\begin{aligned}&\iiint_V\left(\vec{E}_s^{rev}\cdot\vec{J}_a^{fwd}-\vec{H}_a^{rev}\cdot\vec{M}_a^{fwd}\right)dv = \iiint_{V_s}\left(\vec{E}_s^{rev}\cdot\vec{J}_a^{fwd}-\vec{H}_a^{rev}\cdot\vec{M}_a^{fwd}\right)dv\\&=\sum_{i=1}^{N}\iiint_{V_i}\left(\vec{E}_a^{rev}\cdot\vec{J}_a^{fwd}-\vec{H}_a^{rev}\cdot\vec{M}_a^{fwd}\right)dv = \sum_{i=1}^{N}\left(\vec{E}_i^{rev}\cdot\vec{P}_i^{fwd}-\vec{H}_i^{rev}\cdot\vec{M}_i^{fwd}\right),\end{aligned} \tag{10}$$

where *N* represents the number of dipoles used to model the noise source. Note that the letter *M* used in the reciprocity theorem represents magnetic current density defined in Maxwell's equation, while the letter *M* used in the final equation represents the magnetic dipole moment. The unit of the magnetic dipole moment is $V{\cdot}m$ because the magnetic dipole is derived by integrating the magnetic current density, which is different from $A{\cdot}m^2$ derived from an electric current loop in [11]. Basically, an arbitrary electrically small source can be replaced by six kinds of dipoles based on the multiple expansion of a radiation source. When the radiation source is located close to a large ground plane, which is the usually the case in modern electronic devices, the radiation from tangential electric dipoles and vertical magnetic dipoles is canceled by their images. Therefore, in Cartesian coordinates, the vertical electric dipoles P_z and tangential magnetic dipoles M_x and M_y are enough to represent the noise source.

The right side of the Lorentz reciprocity theorem (Eq. (9)) is associated with electromagnetic fields and current density on the cross section of the antenna port, which is typically a good transmission line. As voltage and current are well defined in a transmission line (i.e., TEM mode), the field and current density can be changed to voltage and current quantities as [12]:

$$\iiint_V \left(\vec{J}_a^{\,rev} \cdot \vec{E}_a^{\,fwd} - \vec{M}_a^{\,rev} \cdot \vec{H}_a^{\,fwd} \right) dv = -\left(\frac{1}{Z_{in}} + \frac{1}{Z_L} \right) U_a^{fwd} U_a^{rev}, \tag{11}$$

where Z_L is the load impedance of the victim antenna in the forward problem, which is usually 50 ohm. Z_{in} is the input impedance of the victim antenna in the reverse problem. U_a^{fwd} is the voltage coupled on the victim antenna in the forward problem. U_a^{rev} is the voltage excited on the victim antenna in the reverse problem.

Substituting Eqs. (10) and (11) into Eq. (9) gives [13]

$$U_a^{fwd} = \frac{Z_{in} Z_L}{U_a^{rev}(Z_{in} + Z_L)} \sum_{i=1}^{N} \left(-P_i^z \left(\hat{z} \cdot \vec{E}_i^{\,rev} \right) + M_i^x \left(\hat{x} \cdot \vec{H}_i^{\,rev} \right) + M_i^y \left(\hat{y} \cdot \vec{H}_i^{\,rev} \right) \right). \tag{12}$$

From an engineering perspective, a transfer function concept can be defined based on Eq. (12) to quantify the coupling relationship from each dipole moment to the victim antenna as

$$U_a^{fwd} = \sum_{i=1}^{N} \vec{f}_{P_i} \cdot \vec{P}_i + \sum_{i=1}^{N} \vec{f}_{M_i} \cdot \vec{M}_i \tag{13}$$

$$\vec{f}_{P_i} = -\frac{Z_{in} Z_L}{U_a^{rev}(Z_{in} + Z_L)} \vec{E}_i^{\,rev} \quad \vec{f}_{M_i} = \frac{Z_{in} Z_L}{U_a^{rev}(Z_{in} + Z_L)} \vec{H}_i^{\,rev}, \tag{14}$$

where $\vec{f}_{P_i}$ is a transfer function representing the coupled noise from each electric dipole moment $\vec{P}_i$. $\vec{f}_{M_i}$ is a transfer function representing the coupled noise from each magnetic dipole moment $\vec{M}_i$. There are two important observations: the transfer function has a linear relationship with its respective E- and H-field, and the transfer functions can be obtained as long as the respective E- and H-field are acquired in the reverse problem. Thus, the coupling voltage on the victim antenna can be expressed by the linear superposition of the product of equivalent dipole moments and the corresponding electromagnetic fields. The final form is simple, but describes the coupling mechanism quite intuitively. It states that the coupling is simply proportional to the fields (when the victim antenna radiates) on the IC location and different fields contribute depending on the type of IC radiation. This understanding can greatly improve the design procedure. Detailed radiation structures do not necessarily need to be known to understand the RF desensitization problems; even with a brief information of noise source (type and orientation), the characteristics of RF desensitization can be fully understood and the EMI level can be quantitatively estimated, which will provide an efficient design tool and facilitate pre-layout design.

Several simple models were created in the full-wave simulation tool, HFSS, to validate the proposed method. In these models, a single dipole moment was treated as the noise source. The victim antenna is a 28 mm × 37 mm patch antenna that has a center frequency designed to 2.5 GHz. In these models, $P_z = 1A \cdot m$, $M_x = 1V \cdot m$ and $M_x = 1V \cdot m$ are used, respectively. Based on the proposed method, only the field in the reverse problem needs to be scanned and then the coupling voltage can be calculated by using Eqs. (13) and (14). For comparison, the coupling voltage was also obtained directly from simulation.

In the comparison, the typical error of the proposed method was less than 0.1 dB. The maximum error reached 1.4 dB for dipole M_y at 2.8 GHz. The differences were introduced by numerical errors in the reverse problem. Three field values needed for the calculations, E_z, H_x, and H_y, were obtained by running one simulation (the reverse problem). However, the H_y component at the noise source location was significantly smaller than the other fields (E_z and H_x), which meant H_y was more prone to numerical errors than the other cases, and consequently resulted in the largest error. On the other hand, that is the reason why the M_y case had the lowest coupling voltage. For a source containing three kinds of dipole moments at the same time, the model also showed a good correlation with the maximum error of 0.6 dB at 3 GHz.

2.3. Practical applications

The RF desensitization model was applied to estimate the noise coupling from an LCD panel to an RF antenna in a practical cell phone. The cell phone under test consisted of three parts: a LCD, a main body, and a FPCB which connected the two together. There are two antennas on the cell phone: main antenna and sub antenna as illustrated in **Figure 14**. The high-speed MIPI DSI signals routed on the FPCB can be potential noise sources and couple to the cellular antenna. At the edge of the FPCB, a discontinuity of the ground plane was observed as explained in the previous section. The conduction current and the displacement current formed a current loop in the xz-plane. A current loop facing the y-axis formed an M_y dipole moment, thus, the radiation source was modeled as an M_y dipole moment.

A three-step process was performed to validate the RF desensitization model in this cell phone measurement [14]. The coupled noise from the LCD panel to the antennas was estimated using the model and later compared with direct measurement results.

In step one, the LCD was put into working condition. The radiation source was on and near-field scanning was conducted. Through the process described in the previous section, the

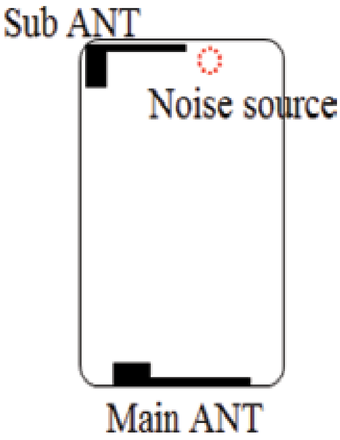

Figure 14. DUT illustration.

dipole moment was reconstructed. The comparison between the measured near-field pattern and the calculated near-field pattern from the reconstructed source is shown in **Figure 6** .

In step two, the antenna radiated in the reverse problem. Because only magnetic dipole *My* existed in this problem, only the *y*-component of the H-field was needed to estimate coupled voltage according to the inner product in Eqs. (13) and (14). In this problem, Eqs. (6) and (7) can be further simplified to:

$$U_a^{fwd} = \vec{f}_M \cdot \vec{M} = \frac{Z_{in} Z_L}{U_a^{rev}(Z_{in} + Z_L)} H_y^{rev} M_y, \tag{15}$$

where H_y^{rev} was measured using a near-field H-probe. The H-field was converted from S-parameter measurement through a probe calibration. In the reverse problem, port one was connected to the victim antenna for excitation, port two was connected to the H-field probe. An S_{21} measurement was needed to measure the transfer function from a unit magnetic dipole M_y to the victim antenna. The set-up for the reverse problem is shown in **Figure 15**. Theoretically, H_y^{rev} should be measured at the exact location of the equivalent dipole moment M_y which is often inside an IC. In reality, the H-field probe often cannot be put inside an IC because of physical constraints. Here, the H-field probe was placed as close to the location of the dipole moment as possible. In order to test robustness of measurement set-up, the H-field probe was moved up several mm to test the variation of the measured H-field; the results were within 1 dB.

After finishing steps 1 and 2, M_y in the forward problem and H_y in the reverse problem were obtained. Using Eq. (15), the coupled voltage on the antenna port was analytically calculated. In step 3, direct measurement of the coupled power was performed to compare with the estimated coupled value. As the noise source is from the clock harmonics of 448.5 MHz, the whole process was repeated for the first seven harmonics of the fundamental frequencies. The proposed method was used to calculate the coupled power at the main antenna port

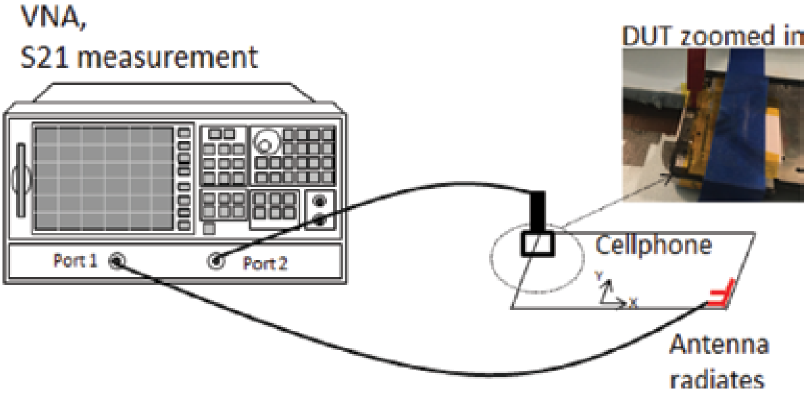

Figure 15. Measurement set-up for the reverse problem.

for the first seven harmonics. Estimated results were compared with measurement results, as shown in **Figure 16**. Besides the main antenna, there was another sub antenna in this cell phone. The same procedures were performed to estimate the coupled power through the forward and reverse problems. The estimated coupled power from the proposed method was compared with measurements. For both of the antennas, estimation errors were mostly within 5 dB, which is acceptable for most engineering practices. The proposed method was successfully validated through the measurements using a practical cell phone.

In engineering practice, engineers often need to know how much improvement a certain change will give. This method can help engineers answer that question and make accurate and fast decisions. As mentioned, RF desensitization problems contain two parts: the noise source and the coupling to an antenna. Recently, a lot of work has been done to build equivalent source modeling to understand the noise source. However, the coupling to the antenna is widely believed to be difficult and unpredictable. A transfer function concept was introduced to quantify the coupling from each unit dipole moment to the antenna. In the beginning, the transfer functions are analytically derived from reciprocity theorem, but it turns out that the transfer functions are relatively easy to obtain in both simulations and measurements.

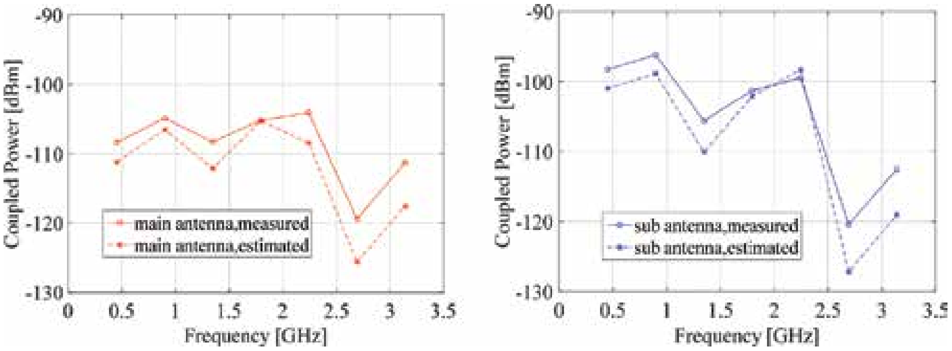

Figure 16. Measured and estimated coupled power to the antennas.

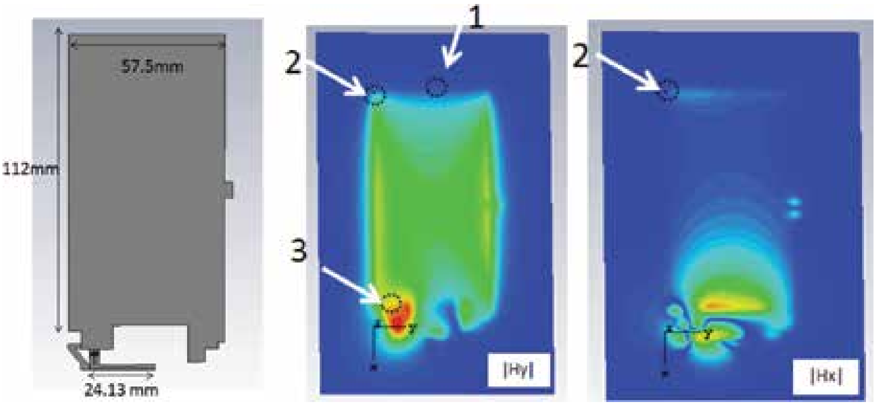

Figure 17. A typical cell phone antenna model (left), magnitude of H_y when the antenna radiates (center), and magnitude of H_x when the antenna radiates (right).

One example is to find the best placement of the IC to minimize RF desensitization. For example, a cell phone and its antenna model are shown in **Figure 17**. The simulated magnitude of H_y and H_x at 1 GHz are shown when the antenna radiates. If the noise source was identified as a M_y dipole moment, according to Eqs. (13) and (14), the transfer function from each unit M_y dipole moment to the victim antenna was proportional to H_y in the reverse problem. So out of the given locations 1, 2 and 3, location 1 had the smallest transfer function and location 3 had the largest transfer function. From the RF desensitization perspective, location 1 will be the best place to locate the noise source M_y dipole moment where the coupling between the M_y dipole moment to the victim antenna is the smallest.

The RF desensitization model can also help understand the effect of the noise source rotation. For example, suppose the noise source is fixed at location 2. By rotating the noise source 90°, the M_y dipole moment becomes an M_x dipole moment. According to Eqs. (13) and (14), the transfer function from each unit M_x dipole moment to the victim antenna is proportional to H_x in the reverse problem. Since H_x is much weaker than H_y, the transfer function is much weaker after rotating the noise source by 90°. So for this particular antenna at 1 GHz, rotating the original noise source by 90° will help reduce RF desensitization a lot.

3. Conclusions

In this chapter, an efficient model to understand and mitigate the RF desensitization problem was discussed. As IoT devices are required to increase their radio range, it is essential to understand the mechanism of RF desensitization. A fundamental understanding of EMI noise coupling and having an efficient tool to address this problems early in the design cycle can achieve a fast and low-cost product design. A dipole moment-based reciprocity method was introduced to estimate the RF desensitization problem. Its formulas were analytically derived from Maxwell equations and the reciprocity theorem. Using the derived equations, we clearly identified which part of the equation belonged to the noise source itself and which part belonged to the coupling path of the antenna. A transfer function concept was also introduced to quantify the coupling coefficient from each unit dipole moment to the victim antenna. The transfer functions can be relatively easy to obtain from either simulation or measurement. Using this RF model, we can provide RFI/EMI engineers with a clear idea about what goes wrong and how to fix it.

Author details

Chulsoon Hwang

Address all correspondence to: hwangc@mst.edu

Missouri University of Science and Technology, Rolla, MO, USA

References

[1] Ott HW. Electromagnetic Compatibility Engineering. Hoboken: Wiley; 2009. 872 p. DOI: 10.1002/9780470508510

[2] Motherboard. Why Electric Cars Are Ditchng AM Radio [Internet]. 2016. Available from: https://motherboard.vice.com/en_us/article/yp3vmj/why-electric-cars-are-ditching-am-radio [Accessed: January 10, 2018]

[3] Scogna A, Shim H, Yu J, Oh C-Y, Cheon S, Oh N, Kim DS. RFI and receiver sensitivity analysis in mobile electronic devices. In: Proceedings of Designcon; Santa Clara, CA. January 28–February 2, 2017

[4] Vives-Gilabert Y, Arcambal C, Louis A, de Daran F, Eudeline P, Mazari B. Modeling magnetic radiations of electronic circuits using near-field scanning method. IEEE Transactions on Electromagnetic Compatibility. 2007;**49**(2):391-400. DOI: 10.1109/TEMC.2006.890168

[5] Tong X. Simplified equivalent modelling of electromagnetic emissions from printed circuit boards [thesis]. University of Nottingham; 2010

[6] Yu Z, Koo J, Mix JA, Slattery K, Fan J. Extracting physical IC models using near-field scanning. In: Proceedings of IEEE International Symposium. On Electromagnetic Compatibility; July 26-30, 2010; Fort Lauderdale, FL. 2010. pp. 317320

[7] Cho GY, Jin J, Park HB, Park HH, Hwang C. Assessment of integrated circuits emissions with an equivalent dipole moment method. IEEE Transactions on Electromagnetic Compatibility. 2017;**59**(2):633-638. DOI: 10.1109/TEMC.2016.2633332

[8] Huang Q, Zhang F, Enomoto T, Maeshima J, Araki K, Hwang C. Physics based dipole moment source reconstruction for RFI on a practical cellphone. IEEE Transactions on Electromagnetic Compatibility. 2017;**59**(6):1693-1700. DOI: 10.1109/TEMC.2017.2705641

[9] Huang Q, Chen Y, Hwang C, Fan J. Machine learning based source reconstruction for RF desensitization analysis. In: Proceedings of Designcon 2018; Santa Clara; January 28–February 2, 2018

[10] Hwang C, Pommerenke D, Fan J, Enomoto T, Maeshima J, Araki K. Modeling and estimation of LCD noise modulation for radio frequency interference. IEEE Transactions on Electromagnetic Compatibility. 2017;**59**(6):1685-1692. DOI: 10.1109/TEMC.2017.2705178

[11] Wilson P. On correlating TEM cell and OATS emission measurements. IEEE Transactions on Electromagnetic Compatibility. 1995;**37**(1):1-16. DOI: 10.1109/15.350235

[12] Richmond JH. A reaction theorem and its applications to antenna impedance calculations. IRE Transactions on Antennas and Propagation. 1961;**9**(6):515-520. DOI: 10.1109/TAP.1961.1145068

[13] Lee S, Zhong Y, Huang Q, Enomoto T, Seto S, Araki K, Fan J, Hwang C. Analytical intra-system EMI model using dipole moments and reciprocity. In: Proceedings of IEEE International Symposium On Electromagnetic Compatibility; May 14-17, 2018; Singapore. 2018

[14] Huang Q, Enomoto T, Maeshima J, Araki K, Fan J, Hwang C. Accurate and fast RFI prediction based on dipole moment sources and reciprocity. In: Proceedings of Designcon; 2018; Santa Clara. January 28–February 2, 2018

Edited by Mamun Bin Ibne Reaz
and Mohammad Arif Sobhan Bhuiyan

Radio frequency (RF) refers to frequencies between the upper limit of audio frequencies (>20 KHz) and the lower limit of infrared frequencies (<300 GHz). The increased popularity and easy operation of RF devices for different end users and corporate applications such as RFID, Bluetooth, Zigbee and Wi-Fi devices and sensors have raised the demand for small power and less off-chip components that tend to achieve integrated circuits with *added security and convenience*. Concurrent technologies allow the scientists to reinvent low-power, high-performance and reliable RF systems, circuits and components for many home and commercial applications. The features of RF systems, circuits and components are still being researched and integrated in existing systems to create marketable and potential new RF products for more exciting applications.

Published in London, UK

IntechOpen

ISBN 978-1-83962-096-6
9 781839 620966